University of Pennsylvania
ScholarlyCommons

Publicly Accessible Penn Dissertations

Summer 8-13-2010

Morphology of Ion-Containing Polymers: Correlations Between Structure, Dynamics, and Ion Conduction

Wenqin Wang
University of Pennsylvania, wenqinw@seas.upenn.edu

Follow this and additional works at: http://repository.upenn.edu/edissertations

 Part of the Polymer and Organic Materials Commons, and the Polymer Chemistry Commons

Recommended Citation
Wang, Wenqin, "Morphology of Ion-Containing Polymers: Correlations Between Structure, Dynamics, and Ion Conduction" (2010). *Publicly Accessible Penn Dissertations*. 231.
http://repository.upenn.edu/edissertations/231

This paper is posted at ScholarlyCommons. http://repository.upenn.edu/edissertations/231
For more information, please contact libraryrepository@pobox.upenn.edu.

Morphology of Ion-Containing Polymers: Correlations Between Structure, Dynamics, and Ion Conduction

Abstract
Ion-containing polymers are of intense interest for applications in energy storage and conversion devices. The conductivities of these polymers are determined by both the ion mobility and the total number of mobile charge carriers, which in turn depend on the chemical structure and morphology. To rationally design ion-containing polymers with high conductivity, a comprehensive understanding of their multi-scale structure is essential.

The morphologies of several ion-containing polymers have been explored as a function of material chemistry and external stimuli by X-ray scattering, scanning transmission electron microscopy, and various types of spectroscopy. The fundamental structure-property relationships in ion-containing polymers are discussed. Two classes of ion-containing polymers with very different aggregation behaviors have been studied. The first class is the polystyrene-based ionomers, where there are unfavorable interactions between the polymer matrix and ionic groups. The ionic functional groups in these hydrocarbon-based ionomers self-assemble into ionic aggregates, due to the strong electrostatic interactions in the low dielectric constant matrix and the lack of any solvation interactions between ions and hydrocarbons. The effects of acid content, neutralization level, and cation type on the size, number density, and composition of ionic aggregates were explored. The morphological findings provide a framework for interpreting the dielectric relaxation behaviors of the same ionomers, so as to establish correlations between structure and dynamics.

The second class is poly(alkyl oxide)-based ionomers. The ionic groups have favorable interactions with the polymer matrix in poly(ethylene oxide) (PEO)-based polyester ionomers or urethane groups in poly(tetramethylene oxide)-based polyurethane ionomers. The states of ions are highly dependent on the PEO length, cation size and temperature in PEO-based ionomers. Decreasing cation size from Cs to Li results in a transition of ionic states from isolated ion pairs to aggregated ion pairs. As the temperature increases, these ionomers exhibit greater microphase separation of the ionic groups due to the decreased ability of PEO to solvate the ions. These findings combine to greatly advance our understanding of the interplay between morphology and ion conduction in single-ion conductors.

Degree Type
Dissertation

Degree Name
Doctor of Philosophy (PhD)

Graduate Group
Materials Science & Engineering

First Advisor
Karen I. Winey

This dissertation is available at ScholarlyCommons: http://repository.upenn.edu/edissertations/231

Keywords
Ion-Containing Polymers, Morphology, X-ray Scattering, Structure-Property Relationship, Polystyrene-based Ionomers, Poly(ethylene oxide)

Subject Categories
Polymer and Organic Materials | Polymer Chemistry

This dissertation is available at ScholarlyCommons: http://repository.upenn.edu/edissertations/231

MORPHOLOGY OF ION-CONTAINING POLYMERS: CORRELATIONS BETWEEN STRUCTURE, DYNAMICS, AND ION CONDUCTION

Wenqin Wang

A DISSERTATION

in

MATERIALS SCIENCE AND ENGINEERING

Presented to the Faculties of the University of Pennsylvania

in Partial Fulfillment of the Requirement for the Degree of Doctor of Philosophy

2010

Supervisor of Dissertation

_____

Karen I. Winey, Professor, Materials Science and Engineering

Graduate Group Chairperson

_____

Russell J. Composto, Professor, Materials Science and Engineering

Dissertation Committee

Ralph H. Colby, Professor, Materials Science and Engineering

Russell J. Composto, Professor, Materials Science and Engineering

Paul A. Heiney, Professor, Physics and Astronomy

MORPHOLOGY OF ION-CONTAINING POLYMERS: CORRELATIONS BETWEEN STRUCTURE, DYNAMICS, AND ION CONDUCTION

COPYRIGHT

2010

Wenqin Wang

Acknowledgements

First, I would like to thank my advisor, Professor Karen I. Winey, for all the guidance and support during my Ph.D. career. Throughout the years, Karen has greatly broadened my scope on research and trained me to be a better scientist in many different aspects. I especially appreciate her encouragement for collaboration and inspiring me to be a successful team player. Moreover, Karen has patiently shaped me into a much better communicator, in both writing and presentation.

I would also like to thank my thesis committee, Professor Ralph H. Colby, Professor Russell J. Composto, and Professor Paul Heiney for their critical review of my research proposal and progress report, detailed guidance, and valuable comments. I especially appreciate Professor Colby's thought provoking discussions and suggestions. Professor Composto has given extremely helpful guidance on both writing and science. Professor Heiney trained me on the X-ray scattering, one of the main tools for my thesis work, and shared me his expertise in this area. I would also like to thank Professor Cherie Kagen for serving as my committee member during my research proposal. I thank Professor Shu Yang for sharing many instruments in her lab, including vacuum line, FTIR spectrometer, and GPC.

I am grateful for the opportunities to collaborate with many wonderful professors, postdocs, and students from different universities. I would like to thank Professor Shulamith Schlick and Andrew J. Perkowski from University of Detroit Mercy for their expertise in electron spin resonance spectroscopy (NSF project), Professor Timothy E. Long and Dr. Sharlene R. Williams from Virginia Tech for synthesizing novel ion-

containing polymers (MURI project), Professor Joe Eladb, Dr. Hong Chen, Dr. YueSheng Ye, and Liang Gwee from Drexel University for help with ion conductivity and aqueous GPC measurements. I especially would like to thank many collaborators and friends from the Pennsylvania State University, including Professor Colby, again, Professor Janna K. Maranas, Professor Karl T. Mueller, Professor James Runt, Dr. Shichen Dou, Wenjuan Liu, Gregory Tudryn, Dan King, Alicia Castagna, Kan-Ju Lin, Kokonad Sinha, David Roach, Amanda McDermott, Shih-Wa Wang, U Hyeok Choi, and etc. for their excellent collaborations on the DOE project and many other scientific discussions.

I would like to give special thanks to the staffs at Penn for always being so friendly and helpful. I would like to thank Irene Clements, Vicky Lee, Pat Overend, Reymond Shao, and Fred Helmig for their assistance with all kinds of requests I brought up. I would like to thank Dr. Douglas Yates for his expertise in electron microscopy techniques and training me on the STEM, Dr. Lolita Rotkina for training me on the SEM, and Steve Szewczyk for the training on DSC.

Furthermore, I was lucky enough to be surrounded and helped by many friends at Penn. First, I would like to thank my labmates Dr. Nicholas Benetatos, Dr. Nancy Zhou, and Dr. Chris Chan for introducing me to ionomers and teaching me many different experimental techniques, Dr. Minfang Mu for sharing both fun and pains in our daily work, Dr. Sadie White for the helpful suggestions and encouragements on research and great baking recipes, Tsung-Ta Chan for the collaboration on the dynamic mechanical analysis, Dr. Michelle Seitz for lots of excellent scientific and writing suggestions, David Salas-de la Cruz, Jae-Hong Choi, Francisco Buitrago, Rose Mutiso, and Michael

O'Reilly for the good scientific discussions and making our current office full of fun, and Matt Bramson for all the hard work on the sulfonate polystyrene project. Second, I thank Dr. Chen Xu, Dr. Maria McConnell, Dr. Ying Zhang, Dr. Jamie Ford, Dr. Yongan Xu, Dr. Liang Qi, Dr. Yu Liu, Dr. Jay Park, Xuelian Zhu, Jun Chen, Sangah Gam, Mike Hore, Chris Rodd, Wei Liu, Zheng Liu, Jie Li, and many others in MSE department for the friendship and generous help. I especially would like to thank Dr. Mihai Peterca for training me on the Linkam oven for X-ray scattering. Finally, I would like to thank many other good friends, including Tingting Sha, Gang Song, Yi Feng, Qian Liu, Mengmeng Liu, Zhuowei Bao, Ye Xing, and etc. for making my Ph.D. life at Penn so colorful.

Last but also the most importantly, I would like to thank my family. My parents have implanted in me the passion for knowledge since childhood. I am grateful for their endless love and continuous support in my career pursuit for so many years. I thank my brother, Changbo Wang, for always being there for me whenever I need help. I especially thank Qihui Ken Zhu, a very special person in my life, for inspiring me with his dedication, pursuance, and passion for both work and life. This thesis is dedicated to them.

ABSTRACT

MORPHOLOGY OF ION-CONTAINING POLYMERS: CORRELATIONS BETWEEN STRUCTURE, DYNAMICS, AND ION CONDUCTION

Wenqin Wang

Supervisor: Karen I. Winey

Ion-containing polymers are of intense interest for applications in energy storage and conversion devices. The conductivities of these polymers are determined by both the ion mobility and the total number of mobile charge carriers, which in turn depend on the chemical structure and morphology. To rationally design ion-containing polymers with high conductivity, a comprehensive understanding of their multi-scale structure is essential.

The morphologies of several ion-containing polymers have been explored as a function of material chemistry and external stimuli by X-ray scattering, scanning transmission electron microscopy, and various types of spectroscopy. The fundamental structure-property relationships in ion-containing polymers are discussed. Two classes of ion-containing polymers with very different aggregation behaviors have been studied. The first class is the polystyrene-based ionomers, where there are unfavorable interactions between the polymer matrix and ionic groups. The ionic functional groups in these hydrocarbon-based ionomers self-assemble into ionic aggregates, due to the strong electrostatic interactions in the low dielectric constant matrix and the lack of any solvation interactions between ions and hydrocarbons. The effects of acid content, neutralization level, and cation type on the size, number density, and composition of ionic

aggregates were explored. The morphological findings provide a framework for interpreting the dielectric relaxation behaviors of the same ionomers, so as to establish correlations between structure and dynamics.

The second class is poly(alkyl oxide)-based ionomers. The ionic groups have favorable interactions with the polymer matrix in poly(ethylene oxide) (PEO)-based polyester ionomers or urethane groups in poly(tetramethylene oxide)-based polyurethane ionomers. The states of ions are highly dependent on the PEO length, cation size and temperature in PEO-based ionomers. Decreasing cation size from Cs to Li results in a transition of ionic states from isolated ion pairs to aggregated ion pairs. As the temperature increases, these ionomers exhibit greater microphase separation of the ionic groups due to the decreased ability of PEO to solvate the ions. These findings combine to greatly advance our understanding of the interplay between morphology and ion conduction in single-ion conductors.

Table of Contents

List of Schemes

List of Tables

List of Figures

Chapter 1

Introduction

1.1 Background of Ionomer Morphology

Ionomers are a unique class of copolymers containing a small fraction of ionic functional groups, which are typically pendant to a hydrophobic polymer backbone.[1] The strong electrostatic interactions between the ionic groups in the low-dielectric matrix drive the self-assembly of ionic groups into aggregates. These nanoscale aggregates act as physical crosslinks to enable remarkable improvement in the chemical and physical properties of ionomers relative to traditional homopolymers. As a result, ionomers have found application in a variety of industrially important applications ranging from chemical resistant coatings and high performance thermoplastics to selectively permeable ion-transport membranes.

In order to realize rational design and engineering of ionomers for specific applications, a comprehensive understanding of the multi-scale morphology is essential. Various spectroscopic techniques, including Fourier transform infrared (FTIR),[2-6] nuclear magnetic resonance (NMR),[7-9] electron spin resonance (ESR),[10-12] and extended X-ray absorption fine structure (EXAFS),[13-17] have been employed to probe the structure of ionomers on sub-nanometer length scales.[18] While these studies have provided detailed information regarding the local chemical environment, they cannot provide an adequate description of the robust macroscopic properties. X-ray scattering is a powerful tool for investigating the nanoscale morphology of ionomers.[19-22] The formation of ionic

aggregates manifests itself in the appearance of a broad, isotropic scattering peak in the angular region between 1-5 nm^{-1}, which is typically accompanied by a small-angle upturn.[1, 23]

Several models have been proposed that provide reasonable fitting and interpretation of the scattering data.[24-26] The most widely accepted scattering model is the modified hard-sphere scattering model proposed by Yarusso and Cooper.[26] This model suggests that the ionomer peak arises from the interparticle scattering between monodisperse, spherical ionic aggregates arranged with liquid-like order in the polymer matrix of lower electron density. Ding *et al.*[27] later proposed a modified version of Yarusso-Cooper model, a.k.a. Kinning-Thomas model,[28, 29] wherein the Percus-Yevick total correlation function[30] that accounts for correlations between all particles in the system was incorporated into the structural factor instead of the Fournet three-body interference function.[31] While both models fit the ionomer peak equally well, Percus-Yevick total correlation function was shown to be more suitable for systems of high packing fraction.[28] However, neither model interprets the low-angle intensity upturn, which is attributed to larger scale inhomogeneities resulting from parasitic scattering due to voids or un-reacted neutralizing agent.[26]

The modified hard-sphere scattering model has been used to interpret the ionomer peak in a wide array of scattering data and has determined the sizes and spacing between ionic aggregates for a variety of systems including poly(styrene-ran-methacrylic acid) (SMAA) ionomers,[32] sulfonated polystyrene (SPS) ionomers,[26, 33] and poly(ethylene-ran-methacrylic acid) (EMAA)) ionomers.[33] The model has shown that the size of the ionic aggregates from ~ 1.0 nm in diameter for EMAA and SMAA ionomers to ~ 2.0 nm in

diameter for the P(S-SS) ionomers. However, none of these studies employ a second model-independent technique, such as direct imaging, to verify the validity of the model.

Our group has devoted significant effort toward imaging the nanoscale morphology of ionomers by employing scanning transmission electron microscopy (STEM). STEM provides the capability of high resolution imaging as well as chemical and structural characterization of nanometer domains though evaluation of electron energy loss spectra (EELS), X-ray spectra, and electron diffraction patterns.[34] More importantly, high angle annular dark field (HAADF) STEM imaging mode has the advantage that the intensity is roughly proportional to the square of the atomic number, Z, of the scattering atom, which greatly enhances contrast between the cation-rich ionic aggregates and polymer matrix, and avoids chemical staining. HAADF STEM has been applied to ionomers with different polymer backbone structures, acid types, cations types, and sample preparation conditions.[35-43] HAADF STEM images reveal that the morphologies of ion-containing polymers on the nanoscale are much more complicated than previously anticipated from a single, broad scattering peak, and are highly dependent on the sample preparation methods, Table 1.1.

Table 1.1 Materials, Preparation Methods, and Morphologies Observed in STEM Studies of Ion-Containing Polymers.

Material [ref]	**Neutralization Method**	**Isolation Method**	**Aggregate Shape**	**Aggregate Size**	**Spatial Distribution**
EMAA-Zn[35, 44]	Melt	Extruded	Spheres	~ 2 nm	Uniform
	Melt	Extruded and re-crystallized	Spheres	~ 2 nm	Uniform
SPS-Zn[36]	75%, 100%, 125% in Solution	Precipitated and molded	Spheres and Vesicles	Varied	Uniform
	25% in Solution	Precipitated and molded	Spheres	4-10 nm	Heterogeneous
SMAA-Cs[38]	Solution	Freeze dried and molded	Vesicles	5-20 nm	Uniform
PDMS-Zn[41]	Solution	Precipitated	Spheres and Rods	~ 4 nm ~ 4 × 11 nm	Uniform
	Solution	Precipitated and annealed	Spheres	~ 4 nm	Uniform
PDMS-Ba[41]	Solution	Precipitated	Spheres and Bundles of Rods	~ 4 nm ~ 4 × 60-100 nm	Uniform Uniform
	Solution	Precipitated and annealed	Spheres and Bundles of Rods	~ 4 nm ~ 20-30 nm	Uniform Uniform
EMAA-Na[37]	Melt	Extruded	N/A	N/A	Featureless
	Melt	Extruded and re-crystallized	Spheres	Varied	Multiple coexisting morpholgies
SMAA-Zn[45]	Solution	Solvent cast	Spheres	~ 3 nm	Uniform
	Solution	Precipitated, annealed, and molded	Spheres	~ 4 nm	Uniform
	Melt	Extruded and annealed	Spheres	~ 3 nm	Uniform
SMAA-Cu[42, 46, 47]	Solution	Solvent cast	Spheres	~ 1 nm	Uniform
	Solution	Precipitated and molded	Spheres	Varied size and shape	Heterogeneous
SPS-Zn or Ba[29]	Solution	Solvent cast	Spheres	~ 1-2 nm	Uniform
SPS-Zn, Ba, Cs, or Cu[29]	Solution	Spin coat	Spheres	~ 1-2 nm	Uniform
PTMO-P^{+} [48]	Direct Synthesis	Solvent cast	Spheres	~ 30-60 nm	Uniform

1.2 Quantitative Reconciliation of HAADF STEM and X-ray Scattering Data

The study of ionomers using STEM as a direct imaging method has revealed diverse morphologies of ionomers, which cannot be explained by X-ray scattering data alone. Using a combination of X-ray scattering and HAADF STEM to study the exact same materials provides the potential to verify the applicability of X-ray scattering model and to establish the domain over which the X-ray scattering model provides an accurate description of the system. Using this powerful combination along with the real-space image modeling, our group has achieved quantitative reconciliation of STEM and X-ray scattering data in SMAA ionomers and SPS ionomers.[29, 46, 47]

The combination of STEM and X-ray scattering was first applied to monodisperse gold nanoparticles (1-2 nm in diameter) supported on polystyrene films of varying thickness (20-90 nm).[49] The radius of gold nanoparticles was measured by fitting a Gaussian function to the intensity profile across the feature in the STEM image. The form-factor scattering model was used to interpret the X-ray scattering data from a dilute solution of the exact same gold nanoparticles. The diameter determined from STEM imaging and X-ray scattering are in excellent agreement, thereby demonstrating that STEM methods can be used to provide quantitative information of nanoscale objects in the presence of amorphous polymer.

Our group then applied these STEM methods to examine the nanoscale morphology of $SMAA_{0.072}$-Cu ionomers (7.2 mol% acid).[46] The ionomers were prepared by solution neutralization with copper acetate and followed by solvent casting and vacuum drying. Figure 1.1a shows the HAADF STEM image of a $SMAA_{0.072}$-Cu thin section microtomed from a bulk material. The image shows a dense, uniform distribution

of spherical bright features, corresponding to the Cu-rich ionic aggregates. The size of these ionic aggregates was determined by the same method described previously for gold nanoparticles. X-ray scattering intensity as a function of scattering vector (q) shows three peaks within q =1.6-16 nm^{-1}, corresponding to the "ionomer peak" (3.7 nm^{-1}), polystyrene "polymerization" (7 nm^{-1}) and "amorphous" peaks (13 nm^{-1}), respectively, Figure 1.1b.[46] With confidence in the presence of spherical ionic aggregates, the scattering data were concurrently fit with Yarusso-Cooper model[26] for the ionomer peak, two Lorentzian functions for the polystyrene peaks, and a constant to account for instrumental background scattering. There are four fitting parameters for the Yarusso-Cooper model: the ionic aggregate radius R_1, the radius of closest approach R_{CA} that limits the spatial correlation between two aggregates, the average sample volume per aggregate V_p, and the peak amplitude A. Note that V_p is the inverse number density of the ionic aggregates ($V_p = 1/N_p$). The size of the ionic aggregates obtained from STEM and X-ray scattering is in quantitative agreement.

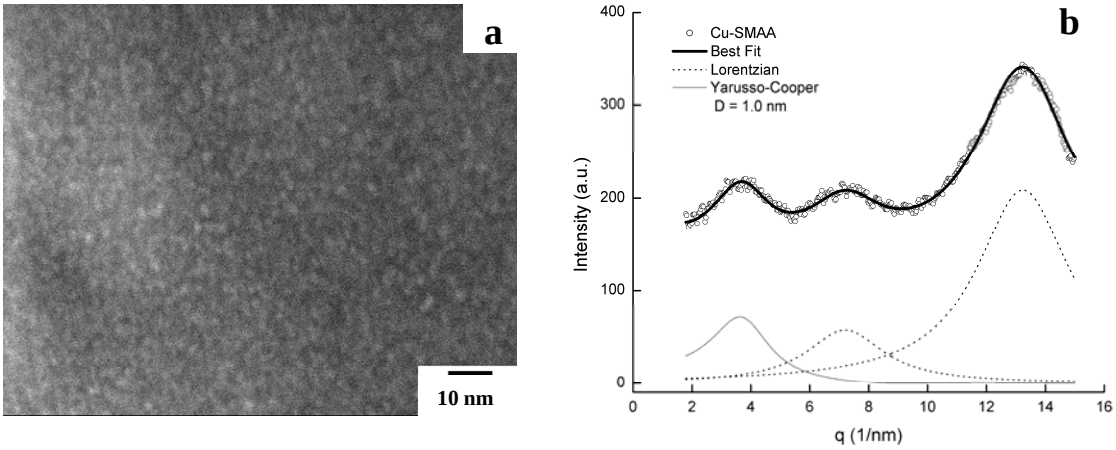

Figure 1.1 (a) HAADF STEM image of SMAA-Cu shows a dense, uniform distribution of Cu-rich features. (b) Scattering intensity as a function of scattering vector, q, for SMAA-Cu along with the best-fit model (solid). The model includes the Yarusso-Cooper model for interparticle scattering from spherical ionic aggregates (grey), two Lorentzian functions (dotted), and an additive constant. (Modified from reference 46).

However, the number density of the ionic aggregates (N_p) obtained from X-ray scattering data is much larger than that directly observed in the HAADF STEM image.[47] The size of the ionic aggregates is on the order of 1 nm, whereas the typical thickness of specimen for STEM imaging is between 50-100 nm, thus the extensive overlap in the 2D projection of 3D specimen could significantly reduce the actual number of aggregates shown in the STEM image. In order to obtain a better interpretation of the morphology observed in the STEM image, 3D real-space structural models were constructed based on the parameters from scattering data and subsequently used to simulate the 2D projections.[47] Figure 1.2a illustrates a 3-D real-space volume of 25 x 25 x 25 nm^3 randomly populated with hard spheres (R_1 = 0.5 nm, R_{CA} = 0.75 nm, and V_p = 5 nm^3/particle). The projected intensity map of the 3D volume shows the particle overlap

with intensities corresponding to numbers of aggregates overlapping (Figure 1.2b). The regions of highest cumulative overlap are shown as brightest red and represent ≥ 8 overlapping spheres. The scale of intensity was adjusted to be as close to the experimental HAADF STEM situation as possible. During STEM imaging, the adjustment of brightness and contrast will typically accentuate the highest intensity regions at the expense of lower intensity area. As a result, for a densely populated system, the regions of highest cumulative overlap are preferentially imaged. The number density of particles observed in the 2D projection (N_{2D}) is only ~5% of that present in the 3D real-space volume of 25 nm thick (N_{3D}). However, it should be noted that despite extensive overlap, the size and shape of the high-intensity regions remain nominally consistent with that of isolated spheres. Thus the extensive overlapping has minor effect on the size of ionic aggregates, further confirming that the size of ionic aggregates observed in HAADF STEM image are indicative of the material.

The real-space depiction of the specific nanoscale morphology of $SMAA_{0.072}$-Cu ionomers and the corresponding projections suggest that overlap in the STEM image of ionomers is significant.[47] The ratio of N_{3D}/N_{2D} was plotted as a function of thickness and fitted with a power law. The relationship between the N_{3D} and N_{2D} for $SMAA_{0.072}$-Cu was subsequently applied to the STEM data including the thickness of specimen measured by EELS and N_{2D} counted from STEM image. It is found the number density of ionic aggregates from STEM is perfectly consistent with that determined from X-ray scattering.

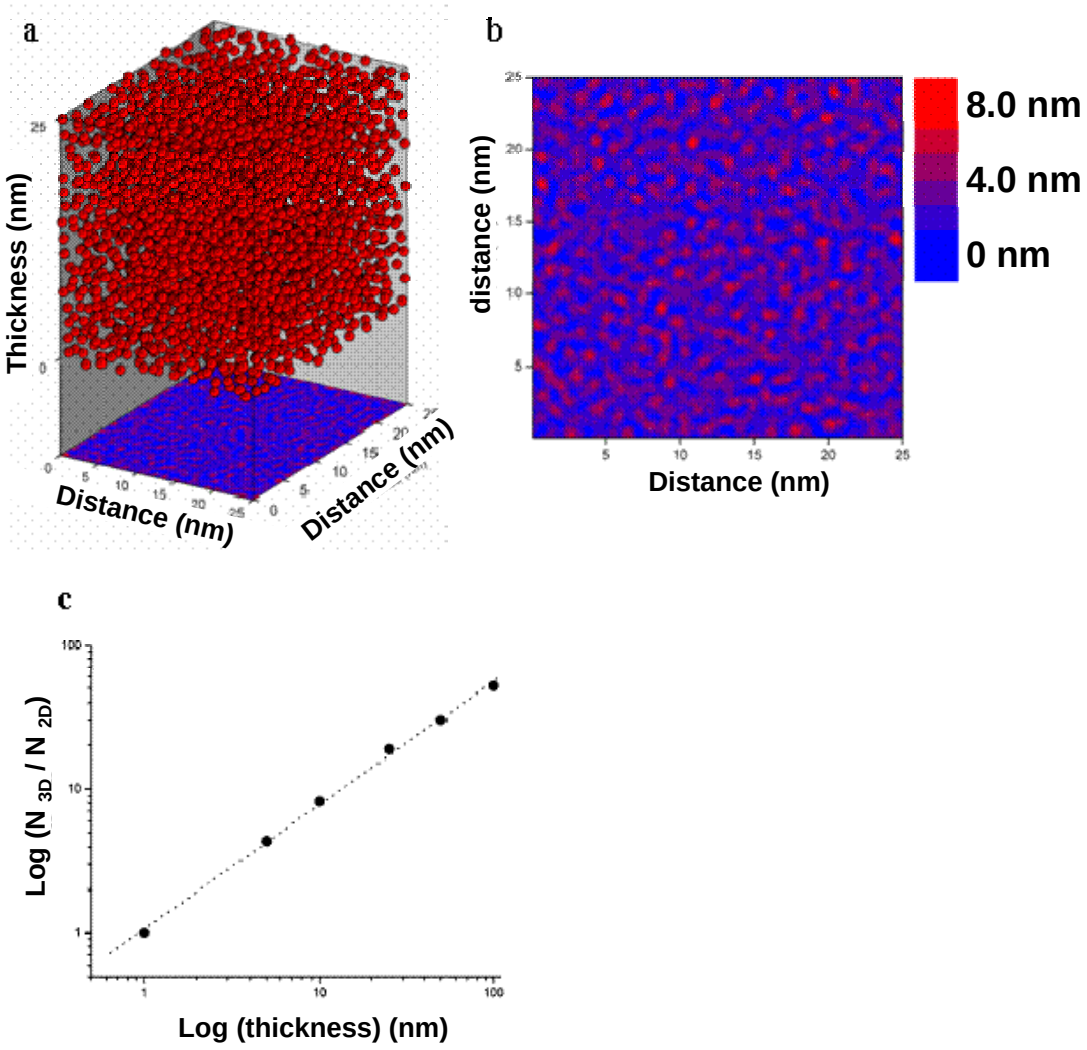

Figure 1.2 (a) 3-D real-space volume (25 x 25 x 25 nm^3) randomly populated with hard spheres (R_1 = 0.5 nm, R_{CA} = 0.75 nm, and V_p = 5 nm^3/particle). (b) 2D projection (c) Values of N_{3D}/N_{2D} (●) as a function of thickness and line of best fit (dotted) plotted on a logarithmic scale. Linear slope (m=0.09) indicates a power law relationship between N_{3D}/N_{2D} and the specimen thickness for the specific parameters of this simulation. (Modified from reference 47)

The quantitative consistency of both size and number density of ionic aggregates obtained from STEM and X-ray scattering of $SMAA_{0.072}$-Cu confirm that the modified hard sphere model provides an excellent description of the nanoscale morphology for this ionomer. This systematic study was further applied to solution neutralized $SPS_{0.019}$ ionomers neutralized to 125% with a variety of cations (Zn, Ba, Cs, Cu, Na, Mg), and successfully reconciled the STEM and X-ray scattering data.[29]

Having confidence in the liquid-like modified hard sphere scattering model for SPS and SMAA ionomers prepared by solvent casting, the fitting parameters from the model can be employed to obtain information about the composition of ionic aggregates. The composition of the ionic aggregates can be inferred from the comparison of the number of cations per aggregates ($N(cation)$) calculated from the X-ray scattering fitting parameters using two different methods. In the first method ($N(cation, R_1)$), the volume of the ionic aggregates based on the R_1 is divided by the volume of an ionic group by assuming a certain ionic coordination structure and 100% ionic groups occupation in the aggregates. The second method ($N(cation, N_p)$) uses the average composition of the acid copolymer to determine the number of cations within a volume of V_p ($1/N_p$). This calculation assumes that all the ionic groups are in the ionic aggregates, thus it provides an upper limit for the number of the ionic groups possible in the aggregates. For $SPS_{0.019}$ neutralized to 125% with metal cations, the two methods give comparable values, which indicates that the ionic aggregates are composed mainly of ionic groups.[29] In contrast, for the $SMAA_{0.072}$-100%Cu ionomers, $N(cation, N_p)$, is an order of magnitude smaller than $N(cation, R_1)$, suggesting that there are not sufficient number of ionic groups in V_p to fill

an ionic aggregate of size R_1.[29, 47] The result implies that the ionic aggregate contains non-ionic species in addition to the ionic groups in $SMAA_{0.072}$-Cu ionomers.

1.3 Ion-Conducting Polymers for Rechargeable Batteries

Due to the growing environmental concerns and the increasing worldwide demand for energy, ion-conducting polymers are of greater interest for various electrochemical energy storage and conversion devices, such as rechargeable batteries and fuel cells. Since the discovery of the complexes of alkali metal salts with polyethylene oxide (PEO) and the corresponding ionic conductivity,[50-52] there has been intense research on the structures and ion-conduction mechanisms of PEO-based polymer electrolytes for rechargeable batteries. Each cation forms multiple coordination bonds with the oxygen atoms in PEO, enabling effective dissolution of a variety of alkali and alkaline-earth salts. Compared to solvent-based liquid systems or ceramic electrolytes, polymer electrolytes have several advantages, including good mechanical properties, improved chemical and thermal stability, and ease of processing.[53] The ionic conductivity is determined by the effective number of conducting ions, the magnitude of elementary charge and the ion mobility.[54] Ion mobility in amorphous polymer electrolytes has been found to be strongly coupled with the segmental motion of polymer chain, and the temperature dependence of ion mobility and conductivity are often discussed on the basis of the "free-volume model".[54, 55] Depending on the electrostatic interactions between the ionic groups and the dielectric constant of the polymer matrix, ions are able to form different association states, including single ions, ion pairs, triple ions, quadrupoles, and larger ionic aggregates. In order to maximize the conducting ion

concentration, the dissociation energy of ion pairs should be low and the dielectric constant of the polymer matrix should be high.[56] For example, replacing the conventional anion with the non-coordinating anion, e.g. perfluorosulphonimide (TFSI), improved the ionic conductivity by an order of magnitude.[57] This is because the extensive charge delocalization in TFSI greatly reduces the binding energy of TFSI with cation.

Much of the research on polymer electrolytes has been focused on polymer/salt mixtures, such as mixtures of PEO with LiTFSI. Although these bi-ion conductors are able to provide reasonable ionic conductivity, the conductivity is generally anion dominated, with Li transference number to be of the order of 0.1-0.3.[58] The transference number refers to the fraction of the current carried by cation or anion.[55] Bi-ion conductors suffer from undesirable concentration polarization, in which anions build up at the electrode/electrolyte interface due to their high mobility in the electrolyte and exclusion from the electrode.[58] The concentration polarization then degrades battery performance. Single-ion conductors with anions fixed to the polymer backbone are of increasing interest for applications in Li-ion batteries, since they can prevent concentration polarization problem and achieve a cation transference number of 1. However, the single-ion conductors studied so far have much lower conductivity than the bi-ion conductors. In order to optimize the ion conduction in this class of materials, a fundamental understanding of the structure and mechanism of ion transport is essential.

Recently, PEO-based sulfonate polyester and polyurethane ionomers have been chosen as model single-ion conductors by several research groups to investigate their ion association behavior and charge transfer mechanism.[59-62] Dielectric spectroscopy studies

based on the modeling of the electrode polarization, in which the ions buildup at electrodes under low frequency electric field, are able to extract both ion mobility and mobile ion concentration from the frequency dependence of complex dielectric loss data.[62] The ions in these ionomers mostly form bound states and, thus, do not contribute to ion conduction.[59-62] The temperature dependence of the conducting ion concentration is Arrhenius,[60-62] suggesting a thermally activated process. The ion mobility increases with increasing temperature and is well described by the VFT equation, consistent with the coupling of ion motion to segmental mobility.[60-62] However, the detailed morphologies of these ionomers are still not available, and might hold the key to developing strategies to improve ion conductivity.

1.4 Outline and Contribution

This dissertation provides a fundamental understanding of the morphologies of ionomers over multi-length scales and the correlations between the structure, dynamics, and ion conduction. First, we extended our group's previous study of strongly segregating ionomers to systematically investigate the morphology of the ionomers as a function of cation type, acid content and neutralization level. The size, shape, local structure, and composition of the ionic aggregates and its correlation with dynamics were examined in detail. Second, we investigated the multi-scale morphology and ion association behavior of PEO-based single-ion conductors as a function of PEO spacer length, cation size, and temperature. Last, the morphology of polyurethane ionomers containing phosphonium bromide was investigated to elucidate the effect of ionic groups

on the hydrogen bonding interactions. The following paragraphs summarize the main content of each chapter.

Chapter 2 presents the morphologies of poly(styrene-*ran*-methacrylic acid) (SMAA) copolymers neutralized with Cu^{2+}, including the local structure and composition of the ionic aggregates as a function of acid content and level of neutralization. X-ray scattering and STEM were employed to obtain the size and number density of ionic aggregates, and electron spin resonance (ESR) spectroscopy provided detailed information regarding coordination structures of Cu^{2+}. This is the first time STEM, X-ray scattering and ESR have been combined to study the exact same materials, thereby overcoming the inconsistency in sample preparation methods from separate studies. Our findings about the composition and local structure of ionic aggregates provide valuable insights for understanding of ion diffusion and polymer dynamics in these ionomers. This chapter was published in *Polymer*: Wang, W.; Chan, T. T.; Perkowski, A. J.; Schlick, S.; Winey, K. I. *Polymer* **2009,** 50, (5), 1281-1287. Copyright © 2009 Elsevier Ltd.

Chapter 3 describes the structure and dynamics of SPS acid copolymers and ionomers as a function of acid content and neutralization level. SPS acid copolymers with three different sulfonation levels were prepared from polystyrene and neutralized to different extents with Na, Cs, and Zn. HAADF STEM imaging verified the formation of spherical ionic aggregates homogeneously distributed in the matrix. The Kinning-Thomas model was used to interpret the ionomer peak from X-ray scattering, which provided detailed information regarding the size, radius of closest approach, and number density of the ionic aggregates. Dielectric relaxation spectroscopy probes the dipolar fluctuations, charge transport, and polarization effects at aggregate-matrix and electrode-

electrolyte boundaries. Correlations between structure and dynamics in SPS acid copolymer and SPS-Zn ionomers are established.

In Chapter 4, a series of Li, Na, and Cs-neutralized polyester ionomers with well-defined PEO spacer lengths between sulfonated phthalates were investigated by X-ray scattering at room temperature. The effects of the spacer lengths and cation type on the multi-scale morphologies of ionomers were examined. We present the hierarchical semi-crystalline structures in these PEO-based ionomers, including crystal structure, states of ionic association, and higher-order crystalline lamellae. Detailed analysis of the normalized X-ray scattering intensity from these ionomers reveals a variety of ionic states that are highly dependent on the cation size. These findings compare favorably with *ab initio* calculations, and advance our understanding of ion-conduction mechanism. This chapter was published in *Macromolecules*: Wang, W.; Liu, W.; Tudryn, G. J.; Colby, R. H.; Winey, K. I. *Macromolecules* **2010**, 43 (9), 4223-4229. Copyright © 2010 American Chemical Society.

In Chapter 5, we extend the study of PEO-based ionomers to explore the effect of temperature on the ion association behaviors using variable-temperature X-ray scattering. Thermally reversible microphase separation of the ionic groups was observed at elevated temperature, resembling the lower critical solution temperature (LCST) behavior in polymer blends. For these ionomers, the extent of microphase separation increases with increasing temperature. We examine the position of the ionomer peak and amorphous peak as a function of temperature and PEO spacer length, and employ two different scattering models to interpret the ionomer peaks. To the best of our knowledge, this is the first report of reversible formation of ionic aggregates in ionomers. A detailed

explanation for the microphase of ionic groups with temperature is proposed. Our findings provide the foundations for understanding the dynamics and ion transport in PEO-based ionomers.

In Chapter 6, we conduct a fundamental investigation of the morphology of novel polyurethanes containing phosphonium bromide to elucidate the effect of ionic groups on the hydrogen bonding interactions. In addition, polyurethanes containing 1,4-butanediol chain extenders were also investigated for comparison with the morphologies of the phosphonium ion-containing analogs. DSC was employed to study the effect of ionic groups and hydrogen bonding interactions on the crystallinity of polyurethanes. Both DSC and FT-IR spectroscopy showed that the presence of ionic groups greatly reduced the hydrogen bonding interactions. HAADF STEM and energy dispersive X-ray spectroscopy (EDS) in the STEM indicated that charged polyurethanes exhibited ionic aggregates that were rich in P and Br. Detailed analysis of the X-ray scattering profiles from stretched and unstretched polyurethane films elucidate the origins of different scattering peaks and help to explain the strain hardening behavior observed in tensile testing. This work represents our group's effect toward understanding the structure of novel ion-containing polymers for applications in electro-active devices. Part of this chapter was published in *Macromolecules*: Williams, S. R.; Wang, W.; Winey, K. I.; Long, T. E. *Macromolecules* **2008**, 41 (23), 9072-9079. Copyright © 2008 American Chemical Society.

Chapter 7 presents the conclusion and a discussion of suggested future work.

1.5 References

1. Eisenberg, A.; Kim, J.-S., *Introduction to Ionomers*. John Wiley & Sons: New York, 1998.

2. Brozoski, B. A.; Painter, P. C.; Coleman, M. M. *Macromolecules* **1984,** 17, (8), 1591-1594.

3. Brozoski, B. A.; Coleman, M. M.; Painter, P. C. *Macromolecules* **1984,** 17, (2), 230-234.

4. Coleman, M. M.; Lee, J. Y.; Painter, P. C. *Macromolecules* **1990,** 23, (8), 2339-2345.

5. Earnest, T. R.; Macknight, W. J. *Macromolecules* **1980,** 13, (4), 844-849.

6. Lu, M.; Runt, J.; Painter, P. *Macromolecules* **2009,** 42, (17), 6581-6587.

7. O'Connell, E. M.; Root, T. W.; Cooper, S. L. *Macromolecules* **1994,** 27, (20), 5803-5810.

8. O'Connell, E. M.; Root, T. W.; Cooper, S. L. *Macromolecules* **1995,** 28, (11), 3995-3999.

9. O'Connell, E. M.; Peiffer, D. G.; Root, T. W.; Cooper, S. L. *Macromolecules* **1996,** 29, (6), 2124-2130.

10. Kutsumizu, S.; Goto, M.; Yano, S. *Macromolecules* **2004,** 37, (13), 4821-4829.

11. Kruczala, K.; Schlick, S. *J. Phys. Chem. B* **1999,** 103, (11), 1934-1943.

12. Bednarek, J.; Schlick, S. *J. Am. Chem. Soc.* **1991,** 113, (9), 3303-3309.

13. Grady, B. P.; Cooper, S. L. *Macromolecules* **1994,** 27, (22), 6627-6634.

14. Ding, Y. S.; Yarusso, D. J.; Pan, H. K. D.; Cooper, S. L. *J. Appl. Phys.* **1984,** 56, (9), 2396-2403.

15. Ding, Y. S.; Register, R. A.; Nagarajan, M. R.; Pan, H. K.; Cooper, S. L. *J. Polym. Sci., Part B: Polym. Phys.* **1988,** 26, (2), 289-300.

16. Grady, B. P.; Cooper, S. L. *Macromolecules* **1994,** 27, (22), 6635-6641.

17. Grady, B. P.; Floyd, J. A.; Genetti, W. B.; Vanhoorne, P.; Register, R. A. *Polymer* **1999,** 40, (2), 283-288.

18. Grady, B. P. *Polym. Eng. Sci.* **2008,** 48, (6), 1029-1051.

19. Williams, C. E.; Russell, T. P.; Jerome, R.; Horrion, J. *Macromolecules* **1986,** 19, (11), 2877-2884.

20. Galambos, A. F.; Stockton, W. B.; Koberstein, J. T.; Sen, A.; Weiss, R. A.; Russell, T. P. *Macromolecules* **1987,** 20, (12), 3091-3094.

21. Lefelar, J. A.; Weiss, R. A. *Macromolecules* **1984,** 17, (6), 1145-1148.

22. Tomita, H.; Register, R. A. *Macromolecules* **1993,** 26, (11), 2791-2795.

23. Chu, B.; Hsiao, B. S. *Chem. Rev.* **2001,** 101, (6), 1727-1761.

24. Marx, C. L.; Caulfield, D. F.; Cooper, S. L. *Macromolecules* **1973,** 6, (3), 344-353.

25. Macknight, W. J.; Taggart, W. P.; Stein, R. S. *J. Polym. Sci. Part C: Polym. Symp.* **1974,** 45, (1), 113-128.

26. Yarusso, D. J.; Cooper, S. L. *Macromolecules* **1983,** 16, (12), 1871-1880.

27. Ding, Y. S.; Hubbard, S. R.; Hodgson, K. O.; Register, R. A.; Cooper, S. L. *Macromolecules* **1988,** 21, (6), 1698-1703.

28. Kinning, D. J.; Thomas, E. L. *Macromolecules* **1984,** 17, (9), 1712-1718.

29. Zhou, N. C.; Chan, C. D.; Winey, K. I. *Macromolecules* **2008,** 41, (16), 6134-6140.

30. Percus, J. K.; Yevick, G. J. *Phys. Rev.* **1958,** 110, (1), 1-13.

31. Fournet, G. *Acta Crystallogr.* **1951,** 4, 293-301.

32. Tsujita, Y.; Yasuda, M.; Takei, M.; Kinoshita, T.; Takizawa, A.; Yoshimizu, H. *Macromolecules* **2001,** 34, (7), 2220-2224.

33. Yarusso, D. J.; Cooper, S. L. *Polymer* **1985,** 26, (3), 371-378.

34. Liu, J. Y. *J. Electron Microsc.* **2005,** 54, (3), 251-278.

35. Winey, K. I.; Laurer, J. H.; Kirkmeyer, B. P. *Macromolecules* **2000,** 33, (2), 507-513.

36. Kirkmeyer, B. P.; Weiss, R. A.; Winey, K. I. *J. Polym. Sci., Part B: Polym. Phys.* **2001,** 39, (5), 477-483.

37. Taubert, A.; Winey, K. I. *Macromolecules* **2002,** 35, (19), 7419-7426.

38. Kirkmeyer, B. P.; Taubert, A.; Kim, J. S.; Winey, K. I. *Macromolecules* **2002,** 35, (7), 2648-2653.

39. Kirkmeyer, B. P.; Puetter, R. C.; Yahil, A.; Winey, K. I. *J. Polym. Sci., Part B: Polym. Phys.* **2003,** 41, (4), 319-326.

40. Benetatos, N. M.; Winey, K. I. *J. Polym. Sci., Part B: Polym. Phys.* **2005,** 43, (24), 3549-3554.

41. Batra, A.; Cohen, C.; Kim, H.; Winey, K. I. *Macromolecules* **2006,** 39, (4), 1630-1638.

42. Benetatos, N. M.; Winey, K. I. *Macromolecules* **2007,** 40, (9), 3223-3228.

43. Taubert, A.; Wind, J. D.; Paul, D. R.; Koros, W. J.; Winey, K. I. *Polymer* **2003,** 44, (6), 1881-1892.

44. Laurer, J. H.; Winey, K. I. *Macromolecules* **1998,** 31, (25), 9106-9108.

45. Kirkmeyer, B. P. Morphologies in Styrenic Ionomers: Effects of Neutralization, Processing and Cations. University of Pennsylvania, Philadelphia, 2003.

46. Benetatos, N. M.; Heiney, P. A.; Winey, K. I. *Macromolecules* **2006,** 39, (16), 5174-5176.

47. Benetatos, N. M.; Chan, C. D.; Winey, K. I. *Macromolecules* **2007,** 40, (4), 1081-1088.

48. Williams, S. R.; Wang, W.; Winey, K. I.; Long, T. E. *Macromolecules* **2008,** 41, (23), 9072-9079.

49. Benetatos, N. M.; Smith, B. W.; Heiney, P. A.; Winey, K. I. *Macromolecules* **2005,** 38, (22), 9251-9257.

50. Fenton, D. E.; Parker, J. M.; Wright, P. V. *Polymer* **1973,** 14, (11), 589-589.

51. Wright, P. V. *British Polymer Journal* **1975,** 7, (5), 319-327.

52. Armand, M. B.; Chabagno, J. M.; Duclot, N. J., In *Fast Ion Transport in Solids*, Vashishta, P.; Mundy, J. N.; Shenoy, G. K., Eds. North Holland, New York 1979; p 131.

53. Scrosati, B.; Vincent, C. A. *MRS Bull.* **2000,** 25, (3), 28-30.

54. Meyer, W. H. *Adv. Mater.* **1998,** 10, (6), 439-448.

55. Ratner, M. A.; Shriver, D. F. *Chem. Rev.* **1988,** 88, (1), 109-124.

56. Ratner, M. A., In *Polymer Electrolyte Reviews*, MacCallum, J. R.; Vincent, C. A., Eds. Elsevier: New York, 1987; Vol. 1.

57. Tarascon, J. M.; Armand, M. *Nature* **2001,** 414, (6861), 359-367.

58. Wright, P. V. *MRS Bull.* **2002,** 27, (8), 597-602.

59. Dou, S. C.; Zhang, S. H.; Klein, R. J.; Runt, J.; Colby, R. H. *Chem. Mater.* **2006,** 18, (18), 4288-4295.

60. Fragiadakis, D.; Dou, S.; Colby, R. H.; Runt, J. *J. Chem. Phys.* **2009,** 130, (6), 064907.

61. Fragiadakis, D.; Dou, S. C.; Colby, R. H.; Runt, J. *Macromolecules* **2008,** 41, (15), 5723-5728.

62. Klein, R. J.; Zhang, S. H.; Dou, S.; Jones, B. H.; Colby, R. H.; Runt, J. *J. Chem. Phys.* **2006,** 124, (14), 144903.

Chapter 2

Local Structure and Composition of the Ionic Aggregates in Cu(II)-neutralized Poly (styrene-*co*-methacrylic acid) Ionomers

2.1 Introduction

Ionomers are copolymers containing a small fraction of ionic functional groups, which are often pendant to the polymer backbone.[1] Most of these ionic functional groups and their counterions self-assemble into ionic aggregates, due to the strong electrostatic interactions in the low dielectric constant media. These ionic aggregates act as physical cross-links that confer remarkable physical and chemical properties to the ionomers. Much research has been devoted to studying the sizes and spatial distribution of ionic aggregates using X-ray scattering,[2-5] neutron scattering,[6-8] and scanning transmission electron microscopy (STEM).[9, 10] The appearance of a broad, isotropic scattering peak at scattering vector q = 1-5 nm^{-1} indicates the existence of ionic aggregates, and STEM enables direct imaging of the ion-rich aggregates. Winey's group has recently applied both STEM and X-ray scattering to investigate the size and number density of spherical ionic aggregates in a poly(styrene-*ran*-methacrylic acid) (SMAA) copolymer neutralized with Cu(II).[11, 12] By accounting for the extensive overlap in the STEM image, the images and the scattering data as interpreted by a liquid-like modified hard-sphere model are in excellent agreement with respect to both aggregate size (R_1) and aggregate number density (N_p). The successful reconciliation between STEM images and X-ray scattering for Cu(II)-neutralized SMAA ionomers demonstrates that the liquid-like modified hard-

sphere model is able to reliably provide quantitative information about the size and number density of ionic aggregates in Cu(II)-neutralized SMAA ionomers. Having confidence in the scattering model allows us to explore the composition of the ionic aggregates.

The composition of the ionic aggregates is a critical part in any model of ion mobility or transport.[13] However, few studies have probed the composition of the ionic aggregates and it remains a subject of controversy whether ionic aggregates contain purely ionic groups or a mixture of ionic groups and non-ionic segments of the polymer chains.[14] The most widely used model, namely the "multiplet" model, presumes that the ionic aggregates contain only ionic groups.[15, 16] Since the composition of ionic aggregates is strongly correlated with the local structure at the cations, most of the studies have been focused on the local environment and specific ligation of the ions in ionomers using Fourier transform infrared (FTIR)[17-19] and electron spin resonance (ESR)[20-22] spectroscopies. In an FTIR study of the local structures of poly(ethylene-*ran*-methacrylic acid) (EMAA) copolymer neutralized by Zn(II) with different neutralization levels, the acid groups were found to coexist in four distinct states: free acid, acid dimer, tetracoordinated zinc carboxylates, and hexacoordinated zinc carboxylates.[18] Early ESR studies of ionomers containing carboxylic and sulfonic acids neutralized with transition metals (Mn(II) and Cu(II)) have detected both isolated cations and cation-cation dimers.[23-25] The study of Cu(II) in ionomeric systems by Schlick's group has shown that ESR spectra can provide a detailed picture of the type and number of ligands and of the strength of the interactions between the counterion and the ligand.[26-30] Kruczala and Schlick studied by ESR the interactions between ion-containing polymers and Cu(II) in

aqueous media as a function of pH and temperature, and deduced the presence of two types of cation-acid complexes, corresponding to cation ligation to one and two carboxylic groups.[31] However, these spectroscopy studies fail to provide insight about the composition of the ionic aggregates.

The objective of this work is a self-consistent description of the SMAA ionomer morphologies that correlates the local structure and composition in the ionic aggregates with the size and number density of the ionic aggregates. The ionic interactions between the methacrylic acid groups and the counterions were examined by ESR spectroscopy, while X-ray scattering and STEM probed the nanoscale ionic aggregates. This is the first time STEM, X-ray scattering and ESR have been combined in a single study, thereby overcoming the inconsistency in materials or preparation methods from separate studies. Furthermore, this paper extends our previous investigation of Cu-neutralized SMAA ionomers to include the influence of the acid content and the level of neutralization.

2.2 Experimental Section

2.2.1 Materials and Sample Preparation: Poly(styrene-ran-methacrylic acid) (SMAA) copolymers with different mole fractions of acid were prepared by bulk free radical polymerization according to the procedures described elsewhere.[32] The copolymerization reaction time was controlled to achieve a conversion ≤ 10% in order to prevent heterogeneity in chemical structures in the later stage of the reaction. The acid contents of copolymers were measured by nuclear magnetic resonance (NMR). The weight average molecular weight of SMAA, as determined by gel permeation chromatography using a polystyrene standard, was ~ $7x10^5$ g/mol for copolymers with

lower acid content (4.1 mol% and 5.8 mol%), and ~ $4x10^5$ g/mol for copolymers with higher acid content (7.2 mol%, 8.3 mol% and 13.3 mol%) with a polydispersity index of ~ 2.0. SMAA copolymers were neutralized by first dissolving the copolymers in toluene. A stoichiometric amount of dehydrated copper(II) acetate was dissolved in methanol and added slowly into the gently agitated SMAA toluene solution to achieve 35%, 50%, or 100% of neutralization. The volume ratio of toluene to methanol was 9:1. The solution mixture was stirred overnight with gentle reflux at ~ 100 ^oC. The Cu(II)-neutralized SMAA (SMAA-Cu) ionomers were recovered by solvent casting at room temperature for 1-2 days. Solvent casting was used, because previous results have shown that rapid precipitation produces non-equilibrium structures with inhomogeneous assemblies of ionic aggregates.[33] The materials were then dried under vacuum at 90 ^oC for 2 days and annealed under vacuum at 120 ^oC for 1 day to remove the acetic acid and residual solvent. All materials were stored at room temperature in vacuum desiccators. The acid content is given as the mole fraction x and the neutralization level as a percentage: $SMAA_x$-yCu. For example, $SMAA_{0.041}$-50Cu is a SMAA copolymer with 4.1 mol% acid and neutralized to 50% with Cu(II). It should be noted that our sample preparation method is reproducible, so the results are indicative of the material. The SMAA ionomers we prepared were studied by X-ray scattering, STEM, and ESR, to provide data that can be reliably integrated.

2.2.2 X-ray Scattering: The solvent-cast, dried, and annealed ionomer films (0.1 to 0.5 mm thick) were used directly for X-ray scattering characterization. Our multi-angle X-ray scattering (MAXS) apparatus generates Cu X-ray from a Nonius FR 591 rotating-anode generator operated at 40 kV and 85 mA. The beam is focused by doubly-

focusing mirror-monochromator optics in an integral vacuum system. The scattering data were collected over an interval of 1 hour using a Bruker Hi-Star multiwire detector with a sample to detector distance of 11 cm. The 2-D analysis and model fitting were performed using *Datasqueeze* software.[34]

The scattering data of SMAA-Cu ionomers were modeled with three functions:

$$I(q) = I_{KT}(q) + L_1(q) + L_2(q) \quad (1)$$

where $I_{KT}(q)$ is the Kinning-Thomas liquid-like hard-sphere model[35, 36] used to interpret the ionomer peak, and $L_1(q)$ and $L_2(q)$ are Lorentzian functions used to fit the two polystyrene-related peaks, as previously reported.[11] The Kinning-Thomas model is the modified version of the Yarusso-Cooper model,[5, 35, 36] where the Percus-Yevick[37] total correlation function that accounts for correlations between all particles in the system was used instead of the Fournet[38] three-body interference function.

2.2.3 Scanning Transmission Electron Microscopy (STEM): STEM specimens were sectioned from solvent-cast, dried, and annealed ionomer films at room temperature using a Reichert-Jung ultramicrotome with a diamond knife to a nominal thickness of 30-50 nm. STEM experiments were performed using a JEOL 2010F field emission transmission electron microscope. High-angle annular dark field (HAADF) images were recorded using a 0.7 nm STEM probe and a 70 μm condenser aperture at an accelerating voltage of 200 keV.

2.2.4 Electron Spin Resonance (ESR): The ESR measurements were performed by our collaborators, Andrew J. Perkowski and Professor Shulamith Schlick from the University of Detroit Mercy. ESR spectra were recorded with a Bruker X-band EMX

spectrometer operating at 9.7 GHz with 100 kHz magnetic field modulation, and equipped with the ER 4111 VT variable temperature unit and the Acquisit 32 Bit WINEPR data system version 3.01 for acquisition and manipulation. The microwave frequency was measured with a Hewlett-Packard 5350B microwave frequency counter. Typical instrumental parameters were as follows: sweep width 1000 G, microwave power 2 mW, time constant 5.12 to 20.48 ms, 10-16 scans depending on signal intensity, 2048 points per scan, and typical modulation amplitude 5 G.

2.3 Results and Discussion

2.3.1 Room-Temperature Ionomer Morphologies: HAADF STEM images of SMAA-Cu samples show spherical, uniformly distributed bright features, corresponding to Cu-rich ionic aggregates within a matrix of lower average atomic number. Figure 2.1 depicts a representative STEM image for $SMAA_{0.133}$-50Cu. The intensity profiles taken across individual bright features were fit with Gaussian functions, and the diameters of the ionic aggregates were given by the full width at half maximum (FWHM) of the Gaussian functions.[11] The average diameters and their standard deviations for four SMAA-Cu ionomers are shown in Table 2.1. Taking into account the extensive projection overlap in the STEM images and the limit of instrumental resolution, STEM images indicate that the sizes of ionic aggregates are independent of the acid content and neutralization level.

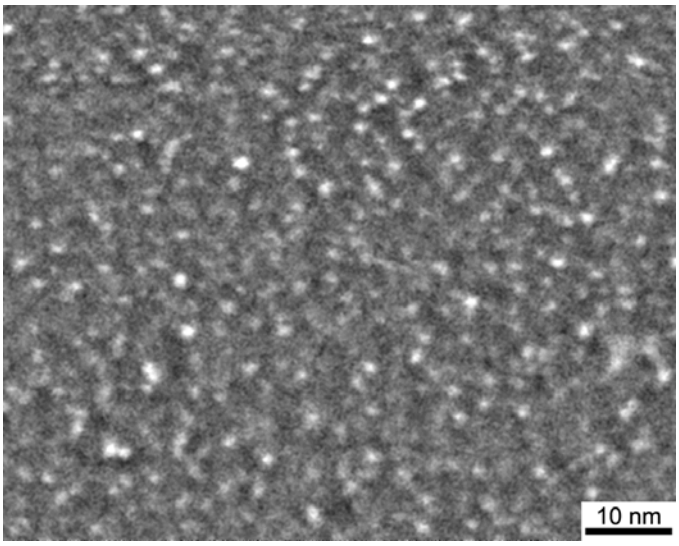

Figure 2.1 HAADF STEM image of $SMAA_{0.133}$-50Cu shows a uniform distribution of spherical ionic aggregates.

Table 2.1 Diameters of ionic aggregates obtained from STEM imaging and X-ray scattering.

Ionomer	D_{STEM} **(nm)**	$2R_{1,\ X\text{-}ray}$ **(nm)** *
$SMAA_{0.072}$-100Cu	**1.2 ± 0.3**	**1.16 ± 0.01**
$SMAA_{0.083}$-100Cu	**1.3 ± 0.4**	**1.15 ± 0.003**
$SMAA_{0.133}$-100Cu	**1.5 ± 0.3**	**N/A**
$SMAA_{0.133}$-50Cu	**1.2 ± 0.3**	**1.06 ± 0.008**

* The standard deviations for $2R_{1,\ X\text{-}ray}$ are obtained when fitting the models to the X-ray scattering data. These values are only indicative of the numerical quality of the fits and not the uncertainties associated with the scattering model.

The X-ray scattering profiles of SMAA-Cu ionomers show three isotropic peaks: polystyrene amorphous halo (~13 nm^{-1}), polymerization peak (~7 nm^{-1}), and ionomer peak (3-4 nm^{-1}), Figure 2.2. A molecular dynamic simulation study of atactic polystyrenes by Ayyagari et al.[39] has found that the amorphous peak arises mainly from

phenyl-phenyl correlation, and the polymerization peak is due primarily to intermolecular backbone-backbone correlations. While the two higher angle peaks are typical features in the scattering patterns of atactic polystyrenes and un-neutralized SMAA copolymers, the ionomer peak indicates the formation of nanoscale ionic aggregates. As the acid content increases, the relative intensity of the ionomer peak with respect to the polystyrene amorphous peak increases significantly at both 100% and 50% neutralization, Figure 2.2a and 2b, respectively. The intensity of the ionomer peak also increases with neutralization level in $SMAA_{0.133}$-Cu, Figure 2.3. The angular position of the ionomer peak is nearly independent of acid content and level of neutralization.

The ionomer peak of the SMAA-Cu ionomers was fitted with a liquid-like modified hard-sphere model based on four parameters: the radius of ionic aggregates R_1, the radius of closest approach R_{CA}, the number density of the aggregates N_p, and the amplitude A (note that $N_p=1/V_p$, where V_p is the sample volume per ionic aggregate).[11] X-ray data from $SMAA_{0.041}$ ionomers were not fitted due to the uncertainties inherent in a weak and broad ionomer peak in this material. In $SMAA_{0.133}$-100Cu, the strong ionomer peak obscures the polymerization peak (~7 nm) of polystyrene, thereby prohibiting a reliable fit. For all other ionomers, fits using Eq. (1) are shown in Figure 2.2 and 2.3 and found to be in good agreement.

Selected samples have been probed by both STEM and X-ray scattering. Table 2.1 compares the size of the ionic aggregates ($2R_1$) measured by these two methods and finds good agreement for this range of acid content. Furthermore, the STEM results verify that a liquid-like model of spherical ionic aggregates is appropriate for these SMAA-Cu ionomers prepared by solution casting and annealing, as previously

reported.[11, 12] In contrast, recent work by the Winey group showed alternate morphologies for a $SMAA_{0.072}$-100Cu ionomer prepared by the precipitation method.[33]

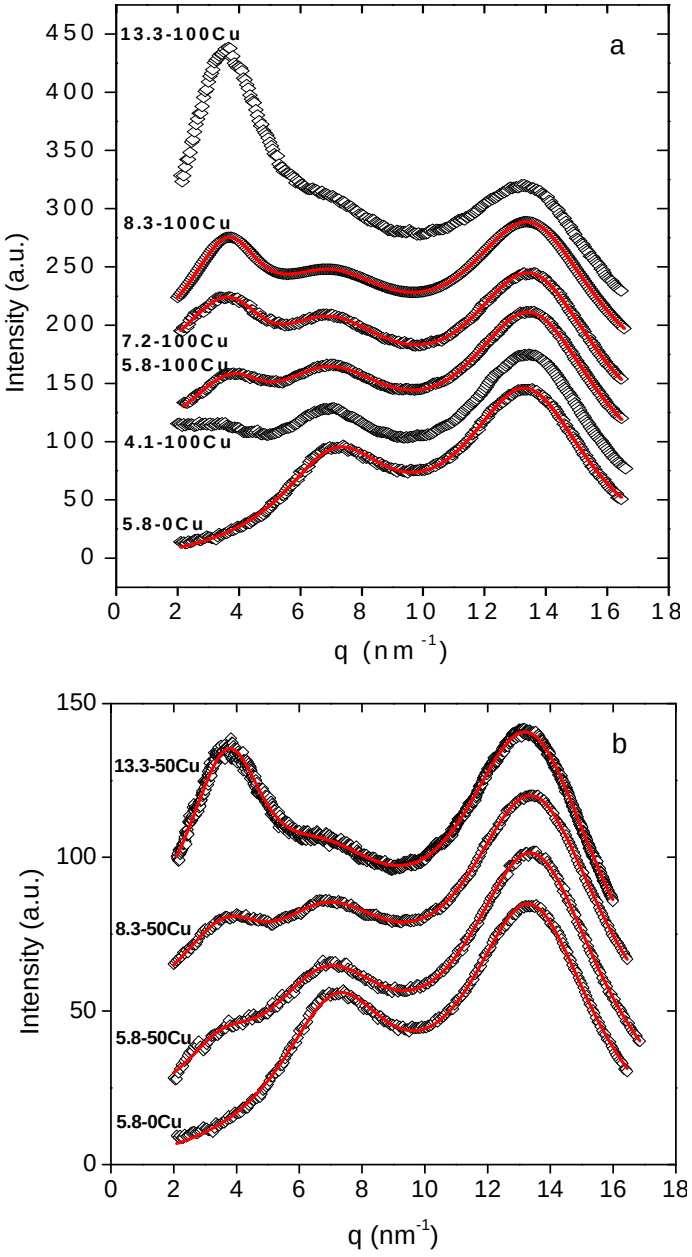

Figure 2.2 X-ray scattering intensity (a.u.) as a function of q with background scattering subtracted for different acid contents (4.1-13.3 mol%) neutralized with Cu(II) acetate along with the best-fit multi-function model given in Eqn (1) (solid line): a) 100% neutralization; b) 50% neutralization.

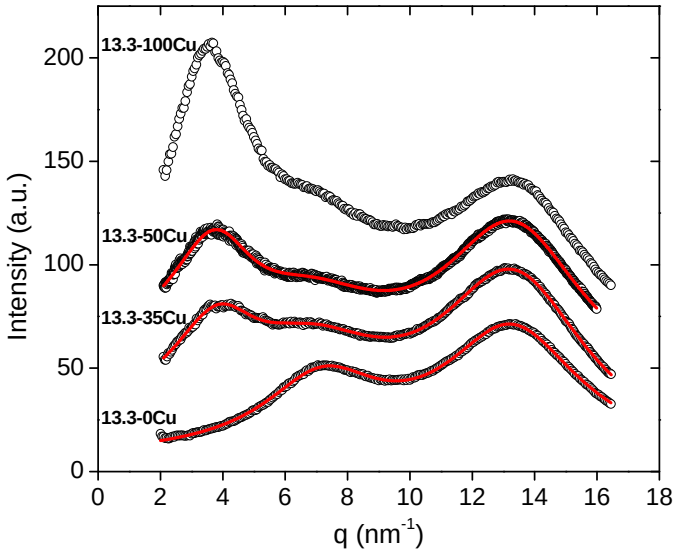

Figure 2.3 X-ray scattering intensity (a.u.) as a function of q with background scattering subtracted for $SMAA_{0.133}$ neutralized with Cu(II) acetate to different levels (0-100%) along with the best-fit multi-function model given in Eqn (1) (solid line).

The R_1 and R_{CA} values for all the SMAA-Cu ionomers are shown in Figure 2.4a. Neither the acid content (5.8-13 mol %) nor the level of neutralization (35-100%) significantly changes the ionic aggregate size (R_1) or the radius of closest approach (R_{CA}). These results in solvent-cast ionomers are consistent with several different ionomer systems studied by other groups.[5, 40] Yarusso and Cooper have applied a similar liquid-like model to interpret the X-ray scattering profiles of sulfonated polystyrenes neutralized with zinc (SPS-Zn), and they also found that the sizes of ionic aggregate were independent of ion content (1.68-6.91 mol% acid, 20-90 % neutralization).[5] Tsujita *et al.*[40] found by X-ray scattering that when neutralized with divalent and trivalent cations, the radii of ionic aggregates in EMAA ionomers were hardly changed (3.5 and 5.4 mol% acid, 40-85 % neutralization).

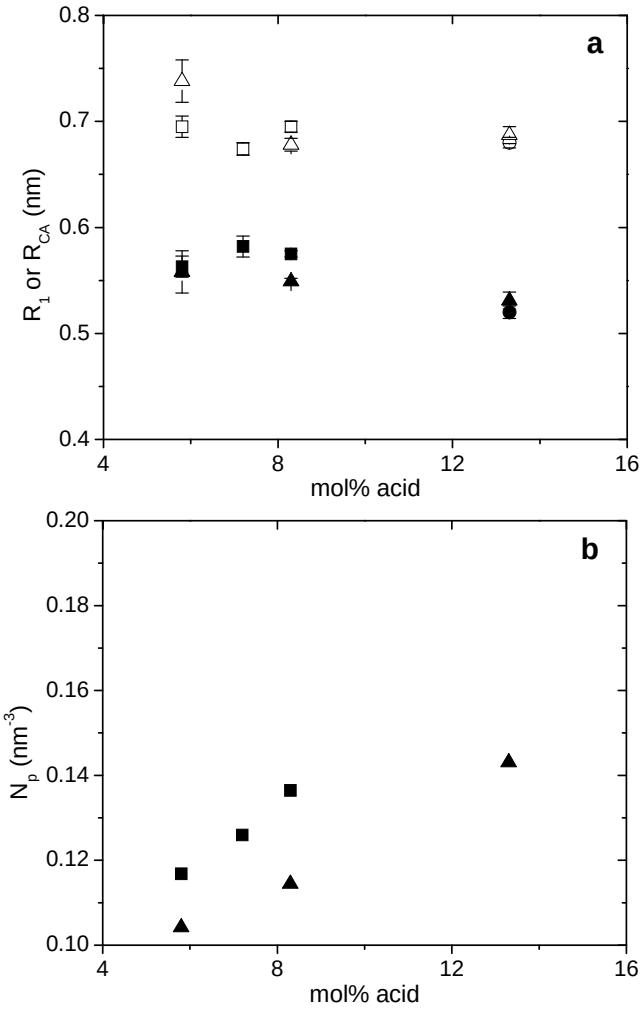

Figure 2.4 a) R_1 (filled) and R_{CA} (open) determined by X-ray scattering as a function of acid content for different levels of neutralization with Cu(II) acetate: □,■ 100%; Δ,▲ 50%; ○,● 35%. The error bar represents the error of the fitting parameter generated by a least-square fit. b) The number density of the ionic aggregate (N_p) as a function of acid content from X-ray scattering results: ■ 100% neutralization; ▲ 50% neutralization.

The X-ray scattering model also provides the number density of the aggregates (N_p), which increases only slightly with increasing acid content and neutralization level, Figure 2.4b. In fact, the number of aggregates per volume increases to a much smaller

extent than expected by assuming, as does the multiplet model, a constant ionic aggregate composition consisting of purely $Cu^{2}(COO^{-})_2$. For example, if the acid content doubles at 100% neutralization, the multiplet model predicts that the number density of ionic aggregation should double. Similarly, if the level of neutralization increases from 50% to 100% at a fixed acid content, N_p should also double. However, the difference in the measured N_p is much less than predicted by the multiplet model when the neutralization level increases from 50% (filled triangles) to 100% (filled squares): 12% increase at 5.8mol% and 19% increase at 8.3mol%. Figure 2.4 suggests that the ionic aggregates incorporate non-ionic species. In contrary to the multiplet model, if all the un-neutralized COOH groups are incorporated into the ionic aggregates of SMAA-Cu ionomers, N_p is expected to increase by a factor of only 1.3 as the neutralization level increases from 50% to 100%. This ratio is closer to our experimental data, supporting our conclusion that ionic aggregates contain COOH groups in partially neutralized ionomers. When the neutralization level increases, the new ionic groups are predominately incorporated into the existing ionic aggregates and thereby form few new aggregates.

In these SMAA-Cu ionomers, R_1 is nominally constant and N_p increases by < 20% as the level of neutralization increases from 50% to 100%. These observations cast doubt on the assumptions of the widely-used multiplet model of ionic aggregates in our partially neutralized SMAA-Cu ionomers, namely that the ionic aggregates contain only ionic species. Using rheological data and FTIR spectroscopy, Vanhoorne and Register have also found that acid groups are associated with the ionic aggregates in poly(ethylene-methacrylic acid) ionomers (EMAA) partially neutralized with Na.[13] However, when EMAA ionomers are neutralized with Zn, a transition metal, their

data suggested that the COOH groups are in the matrix rather than the ionic aggregates.[13] Specifically, COOH groups form reversible dimers with each other through hydrogen bonding in the unneutralized and certain partially neutralized EMAA and SMAA ionomers.[13, 41, 42] Our results for SMAA ionomers partially neutralized with Cu might suggest that the COOH could both form dimers and reside in the ionic aggregates. Thus, the following question arises from our SMAA-Cu ionomer systems: are the excess acid groups for partially neutralized SMAA-Cu ionomers distributed in the polymer matrix or in the ionic aggregates, and how does the acid content affect the distribution? If the acid groups are preferentially associated with the aggregates, how does it affect the coordination structures of cations in the ionic aggregates? To address these questions, ESR spectroscopy experiments were performed on these same ionomers to probe the local structure around the counterions.

2.3.2 Local Ionomer Morphology: Figure 2.5 presents the temperature variation of the ESR spectra for $SMAA_{0.083}$-50Cu. In general terms, these ESR spectra for Cu(II) in SMAA are similar to those previously detected for Cu(II) in poly(ethylene-*co*-methacrylic acid) (EMAA) ionomers.[31] In both systems the spectra indicate complete immobilization of the cation even at ambient temperature (293 K in SMAA and 300 K in EMAA), due to ligation to oxygen atoms from the carboxylic groups. Moreover, the resolution is improved at lower temperatures, because of longer Cu(II) spin-lattice relaxation time. The perpendicular component, represented by the quartet in the range 3200-3300 G is difficult to interpret due to the presence of forbidden transitions. For this reason, conclusions are based on the parallel region, which is characterized by large $g_{\parallel}$- and hyperfine splitting ($A_{\parallel}$) values of the Cu nucleus (I=3/2). The parallel spectrum is

typical of the "strain" effect, arising from a distribution of the g and hyperfine splittings that lead to different widths of each signal, depending on the nuclear spin magnetic quantum number m_I. The spectra at 110 K allow the identification of two sites, site 1 and site 2 in Figure 2.5, based on different values of the $g_\parallel$ and $A_\parallel$: site 1, $A_\parallel$ = 129 G (142x10^{-4} cm^{-1}), $g_\parallel$ = 2.355; site 2, $A_\parallel$ = 153 G (165x10^{-4} cm^{-1}), $g_\parallel$ = 2.308 (Table 2.2). Although the presence of two cation sites is clear from the spectra given in Figure 2.5, more accurate and complete parameters for both sites would require ^{63}Cu enrichment and spectra simulations.

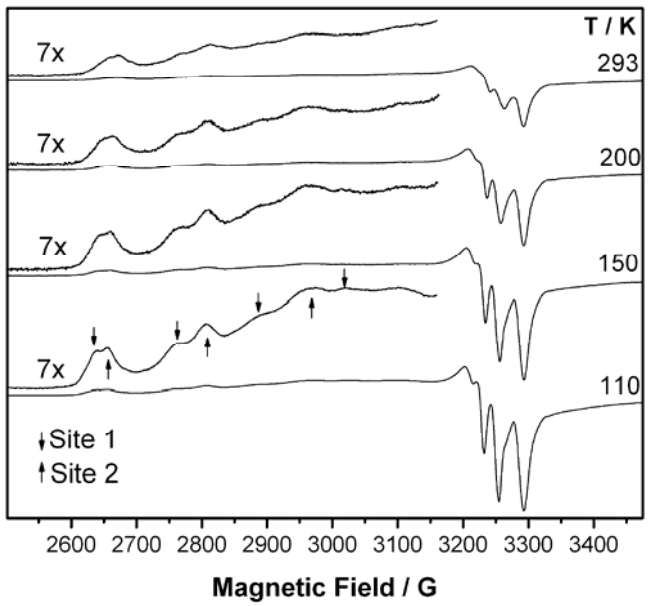

Figure 2.5 X-band ESR spectra of SMAA$_{0.083}$-50Cu as a function of temperature. Vertically expanded portions are shown for all spectra. Downward and upward arrows indicate, respectively, the parallel hyperfine quartet for site 1 and site 2.

The spin-forbidden transition from binuclear Cu-Cu complexes is expected at a magnetic field of ≈ 1600 G, and the distance between the two cations in the dimer can be deduced from the intensity ratio of signals from the mononuclear and dimeric complexes,

as documented in the case on Nafion perfluorinated ionomers neutralized by Cu(II).[43] Signals from the dimeric species were not detected in the SMAA-Cu ionomers, suggesting that the mononuclear Cu(II) complexes are well separated by the polymer chains.

Figure 2.6a presents the ESR spectra at 110 K of SMAA-50Cu samples containing 5.8, 8.3 and 13.3 mol% acid. Qualitatively, the spectra indicate that site 2 is the major site in all three partially neutralized ionomers. There is evidence for a third site for $SMAA_{0.058}$-50Cu, with $A_{\parallel}$ = 167 G (177×10^{-4} cm^{-1}), and $g_{\parallel}$ = 2.275. Another ESR spectrum of $SMAA_{0.058}$-50Cu is shown in Figure 2.6b, for an ionomer sample that was hot pressed at 145 ^{o}C for 10 min after annealing. The spectra from the two preparations are very similar, but the resolution in the pressed sample is improved, allowing the clearer identification of site 3. At 50% neutralization, increasing the acid content apparently reduces the number of sites to two. The change in the relative population of the three different cation sites clearly shows the variation of local environment around Cu^{2+} with acid content. The magnetic parameters for sites 1-3 above are listed in Table 2.2.

Table 2.2 Magnetic parameters for the Cu(II) complexes detected by ESR in the STEM ionomers.[a]

	$g_{\parallel}$	$A_{\parallel}$ / G	$A_{\parallel}$ / 10^4 cm^{-1}
Site 1	**2.355**	**129**	**142**
Site 2	**2.308**	**153**	**165**
Site 3	**2.275**	**167**	**177**

[a] $A_{\parallel}$ (cm^{-1}) = $g_{\parallel}$ x $A_{\parallel}$(G) x 4.667×10^{-5}

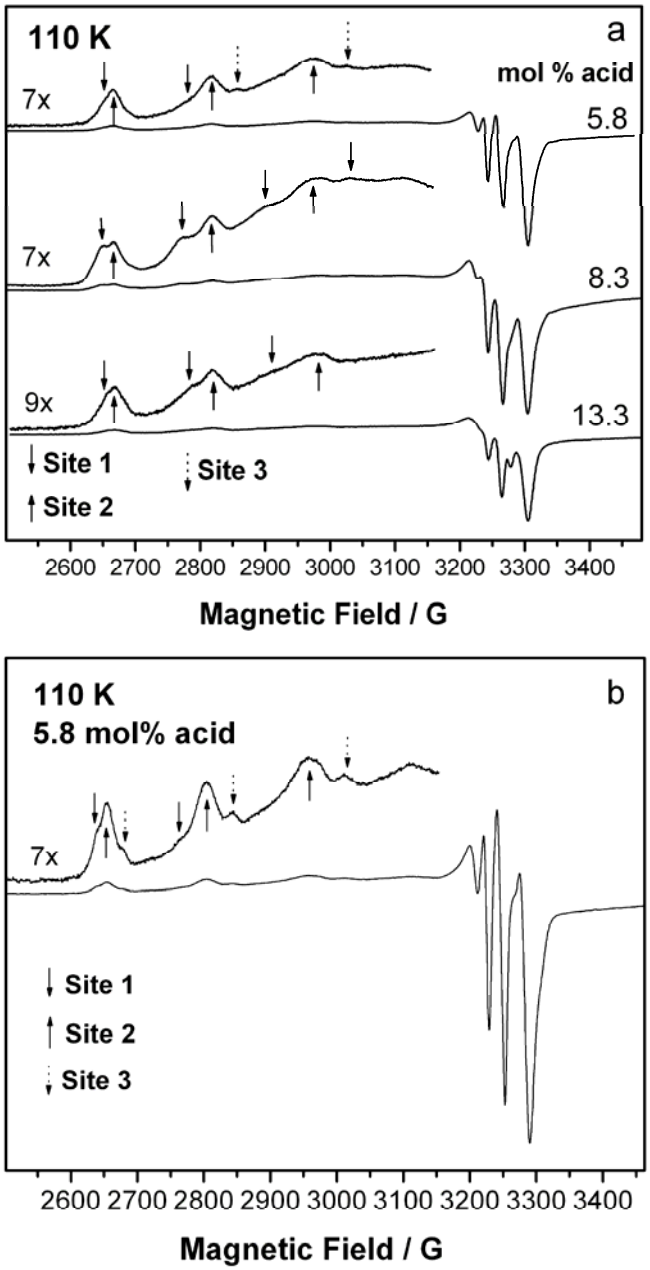

Figure 2.6 a) X-band ESR spectra at 110 K of SMAA-50Cu containing 5.8, 8.3, and 13.3 mol% acid. b) X-band ESR spectra at 110 K of $SMAA_{0.058}$-50Cu after hot pressing. Vertically expanded portions are shown for all spectra. Note the arrows (downward, upward, and dotted) that indicate the positions of the parallel hyperfine signals for sites 1-3, and the improved resolution in the spectrum of the hot-pressed sample.

The $g_{\parallel}$ and $A_{\parallel}$ values in Cu(II) complexes are sensitive to the binding scheme, as described in detail in the Peisach-Blumberg (PB) plots.[44] All ligands in the Cu(II) complexes in the SMAA ionomers are oxygens. If the oxygen ligands originate from charged groups such as COO^- groups, these plots predict a decrease in the $g_{\parallel}$ value and an increase in the $A_{\parallel}$ value compared to the magnetic parameters of the $Cu(H_2O)_6^{2+}$ complex, where all ligands are neutral and $g_{\parallel} > 2.4$ and $A_{\parallel} = 120$ G ($\sim 134 \times 10^{-4}$ cm^{-1}).[31] These expectations are clearly seen in the parameters for sites 1-3 in Table 2.2; qualitatively, these parameters reflect an increase in the number of oxygen ligands from charged groups, in this case COO^- groups, from site 1 to site 2 and to site 3. In addition, the PB plots suggest for sites 1, 2, and 3 complexes with total charges in the vicinity of +1, 0, and -1 respectively. In the case of site 1 this deduction implies two oxygen ligands from the negatively charged $-COO^-$ and two additional oxygen ligands from undissociated acid groups -COOH. For site 2 and a total charge of 0, the ESR parameters indicate Cu(II) complexation with four oxygen ligands from two $-COO^-$ groups. Similarly, the number of oxygen ligands for site 3 suggests a Cu(II) complex with three COO^- groups. These deductions are semiquantitative and final values of the g values and Cu hyperfine splittings should be determined by ^{63}Cu enrichment and simulation of the spectra.

All ESR spectra of the fully neutralized SMAA ionomer, SMAA-100Cu, consist of rather broad lines and show a site with $A_{\parallel} = 155$ G, very close to the major site (site 2) in SMAA-50Cu; see Appendix A. The spectra of fully-neutralized SMAA-Cu ionomers also suggest the formation of more ordered structures at 13.3 mol% compared to SMAA-100Cu with lower acid contents. Due to the limited resolution, it is impossible to determine the type of sites in the fully-neutralized ionomers. Nevertheless, the

qualitative results are in agreement with the scattering and imaging results, which indicate that upon increasing the neutralization level fewer new ionic aggregates are formed, but the ionic aggregates incorporate more acid-cation pairs.

The ESR conclusions are in contrast to X-ray absorption studies in EMAA ionomers: Grady *et al.*[45] found identical local environments around zinc atoms in all zinc- neutralized EMAAs for different preparation methods, acid contents and neutralization levels. However, the work of Farrell and Grady on sodium-neutralized EMAA ionomers detected disordered local environments around the cation that are highly dependent on neutralization levels,[46] as also seen in our ESR results. The contrast in our ESR results for SMAA-Cu ionomers and the X-ray absorption results for EMAA-Zn ionomers could simply reflect the differences in copolymer type, cation, neutralization method, or thermal processing. Alternatively, the distinct results could be associated with differences in sensitivity for the two methods. Given that ESR is only applicable when ionomers are neutralized with paramagnetic cations, such as copper, an interesting next step would be to use X-ray absorption to study Cu-neutralized ionomers in conjunction with the powerful combination of STEM, X-ray scattering and ESR.

Based on the fact that the number density of the ionic aggregates (N_p) increases by < 20% slightly when the percent of neutralization doubles (Figure 2.4b), we conclude that a considerable fraction of un-neutralized acid groups are incorporated into the ionic aggregates when ionomers are partially neutralized. This is consistent with the presence of multiple local environments in partially neutralized SMAA-Cu via ESR (Figure 2.6) as well as with the absence of Cu-Cu dimers mentioned above. ESR results also show that the relative intensity of different sites varies with acid content, thus reflecting the

sensitivity of the method to the structure and composition of the ionic aggregates in ionomers.

2.4 Conclusion

The morphologies, compositions, and coordination structures of ionic aggregates in a wide range of Cu(II)-neutralized SMAA ionomers have been studied by a combination of X-ray scattering, HAADF STEM imaging, and ESR spectroscopy. The sizes of the spherical ionic aggregates are independent of acid content and neutralization level, as shown by both X-ray scattering and STEM. The composition of ionic aggregates is found to change with acid content and neutralization level based on the following two observations. 1) As the acid content or neutralization level doubles, the number density of ionic aggregates increases by a much smaller extent, which contradicts the widely-held assumption of constant aggregate composition. 2) ESR spectra show the presence of multiple disordered cation-acid coordination structures and the order of the local cation environment increases with acid content. Consequently, the ionic aggregates apparently contain non-ionic species, including un-neutralized acid groups, and the ionic aggregates incorporate fewer non-ionic species as the acid content increases. The strength of ionic association and ion mobility are strongly related to the local structure and composition of these ionic aggregates. Our findings provide valuable information for other ionomers with carboxylic acids and for the understanding of ion diffusion and polymer dynamics in these ionomers. This systematic study using three complementary methods can be extended to other acid types and paramagnetic cations for a broader investigation of the structure-property relationships in ion-containing polymers.

2.5 References

1. Eisenberg, A.; Kim, J.-S., *Introduction to Ionomers*. John Wiley & Sons: New York, 1998.

2. Marx, C. L.; Caulfield, D. F.; Cooper, S. L. *Macromolecules* **1973,** 6, (3), 344-353.

3. Macknigh.Wj; Taggart, W. P.; Stein, R. S. *J. Polym. Sci., Part C: Polym. Symp.* **1974,** 45, (1), 113-128.

4. Roche, E. J.; Stein, R. S.; Russell, T. P.; Macknight, W. J. *J. Polym. Sci., Part B: Polym. Phys.* **1980,** 18, (7), 1497-1512.

5. Yarusso, D. J.; Cooper, S. L. *Macromolecules* **1983,** 16, (12), 1871-1880.

6. Earnest, T. R.; Higgins, J. S.; Handlin, D. L.; Macknight, W. J. *Macromolecules* **1981,** 14, (1), 192-196.

7. Earnest, T. R.; Higgins, J. S.; Macknight, W. J. *Macromolecules* **1982,** 15, (5), 1390-1395.

8. Aldebert, P.; Dreyfus, B.; Pineri, M. *Macromolecules* **1986,** 19, (10), 2651-2653.

9. Laurer, J. H.; Winey, K. I. *Macromolecules* **1998,** 31, (25), 9106-9108.

10. Winey, K. I.; Laurer, J. H.; Kirkmeyer, B. P. *Macromolecules* **2000,** 33, (2), 507-513.

11. Benetatos, N. M.; Heiney, P. A.; Winey, K. I. *Macromolecules* **2006,** 39, (16), 5174-5176.

12. Benetatos, N. M.; Chan, C. D.; Winey, K. I. *Macromolecules* **2007,** 40, (4), 1081-1088.

13. Vanhoorne, P.; Register, R. A. *Macromolecules* **1996,** 29, (2), 598-604.

14. Grady, B. P. *Polym. Eng. Sci.* **2008,** 48, (6), 1029-1051.

15. Eisenberg, A. *Macromolecules* **1970,** 3, (2), 147-154.

16. Eisenberg, A.; Hird, B.; Moore, R. B. *Macromolecules* **1990,** 23, (18), 4098-4107.

17. Brozoski, B. A.; Coleman, M. M.; Painter, P. C. *Macromolecules* **1984,** 17, (2), 230-234.

18. Coleman, M. M.; Lee, J. Y.; Painter, P. C. *Macromolecules* **1990,** 23, (8), 2339-2345.

19. Walters, R. M.; Sohn, K. E.; Winey, K. I.; Composto, R. J. *J. Polym. Sci., Part B: Polym. Phys.* **2002,** 40, (24), 2833-2841.

20. Kutsumizu, S.; Schlick, S. *J. Mol. Struct.* **2005,** 739, (1-3), 191-198.

21. Kutsumizu, S.; Goto, M.; Yano, S.; Schlick, S. *Macromolecules* **2002,** 35, (16), 6298-6305.

22. Tsagaropoulos, G.; Kim, J. S.; Eisenberg, A. *Macromolecules* **1996,** 29, (6), 2222-2228.

23. Yamauchi, J.; Yano, S. *Makromol. Chem., Macromol. Chem. Phys.* **1988,** 189, (4), 939-950.

24. Yamauchi, J.; Yano, S. *Macromolecules* **1982,** 15, (1), 210-210.

25. Weiss, R. A.; Lefelar, J.; Toriumi, H. *J. Polym. Sci. Part C: Polym. Lett.* **1983,** 21, (8), 661-667.

26. Szajdzinska-Pietek, E.; Schlick, S., Chapter 7. In *Ionomers: characterization, theory, and applications*, Schlick, S., Ed. CRC Press: Boca Raton, FL, 1996.

27. Bednarek, J.; Schlick, S. *J. Am. Chem. Soc.* **1990,** 112, (13), 5019-5024.

28. Bednarek, J.; Schlick, S. *Langmuir* **1992,** 8, (1), 249-253.

29. Bednarek, J.; Schlick, S. *J. Am. Chem. Soc.* **1991,** 113, (9), 3303-3309.

30. Schlick, S.; Alonsoamigo, M. G.; Bednarek, J. *Colloids Surf., A* **1993,** 72, 1-9.

31. Kruczala, K.; Schlick, S. *J. Phys. Chem. B* **1999,** 103, (11), 1934-1943.

32. Eisenberg, A.; Navratil, M. *Macromolecules* **1973,** 6, (4), 604-612.

33. Benetatos, N. M.; Winey, K. I. *Macromolecules* **2007,** 40, (9), 3223-3228.

34. Heiney, P. A. *Commission on Powder Diffraction Newsletter* **2005,** 32, 9-11.

35. Kinning, D. J.; Thomas, E. L. *Macromolecules* **1984,** 17, (9), 1712-1718.

36. Zhou, N. C.; Chan, C. D.; Winey, K. I. *Macromolecules* **2008,** 41, (16), 6134-6140.

37. Percus, J. K.; Yevick, G. J. *Phys. Rev.* **1958,** 110, (1), 1-13.

38. Fournet, G. *Acta Crystallogr.* **1951,** 4, 293-301.

39. Ayyagari, C.; Bedrov, D.; Smith, G. D. *Macromolecules* **2000,** 33, (16), 6194-6199.

40. Tsujita, Y.; Yasuda, M.; Takei, M.; Kinoshita, T.; Takizawa, A.; Yoshimizu, H. *Macromolecules* **2001,** 34, (7), 2220-2224.

41. Earnest, T. R.; Macknight, W. J. *J. Polym. Sci., Part B: Polym. Phys.* **1978,** 16, (1), 143-157.

42. Arai, K.; Eisenberg, A. *J. Macromol. Sci., Phys.* **1980,** B17, (4), 803-832.

43. Schlick, S.; Alonsoamigo, M. G.; Eaton, S. S. *J. Phys. Chem.* **1989,** 93, (23), 7906-7912.

44. Blumberg, W. E.; Peisach, J. *Arch. Biochem. Biophys.* **1974,** 162, (2), 502-512.

45. Grady, B. P.; Floyd, J. A.; Genetti, W. B.; Vanhoorne, P.; Register, R. A. *Polymer* **1999,** 40, (2), 283-288.

46. Farrell, K. V.; Grady, B. P. *Macromolecules* **2001,** 34, (20), 7108-7112.

Chapter 3

Morphology of Sulfonated Polystyrene Ionomers: Correlation of Structure with Dynamics

3.1 Introduction

Incorporation of a small fraction of ionic functional groups into hydrophobic polymer chains through chemical bonding can greatly enhance the physical properties of the base polymers. These ion-containing polymers, commonly known as ionomers, have been the subject of intensive research for a broad range of applications, ranging from high performance coatings to ion-transport membranes. In order to design materials with desired mechanical or electrical properties, a thorough understanding of the relationships between the structure and dynamics of the materials is essential.

Sulfonated polystyrene (SPS) ionomer has been chosen as a model ionomer and studied by various investigators to understand its morphology and dynamics using X-ray or neutron scattering,[1-6] transmission electron microscopy (TEM),[5, 7] nuclear magnetic resonance (NMR) spectroscopy,[8-10] dynamic mechanical analysis (DMA),[11-13] and etc. However, few of the studies have shown direct correlation of the structure with dynamics. It is widely accepted that ionic groups in SPS ionomers form nanoscale ionic aggregates. The presence of ionic groups increases the viscosity of the ionomers substantially. The viscoelastic behavior of SPS ionomers exhibits three relaxation processes, including segmental motion of polymer matrix, the ion-hopping relaxation, and terminal relaxation,[12, 14] due to the presence of ionic crosslinks. However, the size, shape and

distribution of ionic aggregates are highly dependent on the processing condition and thermal history, which then affect the dynamics of the ionomers. Thus, it is desirable to employ multiple tools to study the morphology and dynamics of exactly the same ionomers.

Broadband dielectric relaxation spectroscopy (DRS), also called impedance spectroscopy, is a powerful tool to probe relaxation processes over wide ranges of frequency (10^{-6} – 10^{12} Hz) and temperature. However, there have been very few reports about the dynamic relaxation behavior of SPS ionomers by DRS.[15] Previous DRS studies on Na-, Cs-, and Zn- neutralized SPS ionomers by Atorngitjawat *et al.* revealed four dielectric relaxation processes: the local β process from the motion of sulfonated phenyl groups, the segmental α process, and the relaxations associated with Maxwell-Wagner-Sillars (MWS) interfacial polarization and electrode polarization (EP).[15] The MWS interfacial polarization typically occurs in multiphase systems in which the phases have different dielectric constants and conductivities. The EP is caused by the accumulation of mobile charges at electrode-electrolyte interfaces. However, detailed information about the morphology of SPS ionomers was not provided by their X-ray scattering study.[15]

Previously, our group has successfully reconciled the morphology of lightly sulfonated polystyrene (1.9 mol% sulfonic acid) neutralized with a variety of cations (Zn, Na, Cs, Cu, Mg, and Ba) using X-ray scattering and scanning transmission electron microscopy (STEM).[5] It was found that the Kinning-Thomas modified hard-sphere model is able to provide quantitative information about size and number density of the ionic aggregates.[5] In this study, a systematic investigation of the morphology *and* dynamics of SPS ionomers as a function of acid content and neutralization level is

performed using a combination of X-ray scattering, High-angle annular dark field STEM, and broadband DRS. SPS copolymers with three different acid contents were prepared and neutralized to different extents with Zn, Na, and Cs, Scheme 3.1. Complementary Fourier transform infrared spectroscopy (FTIR) and differential scanning calorimetry have also been employed to facilitate the interpretation of our findings.

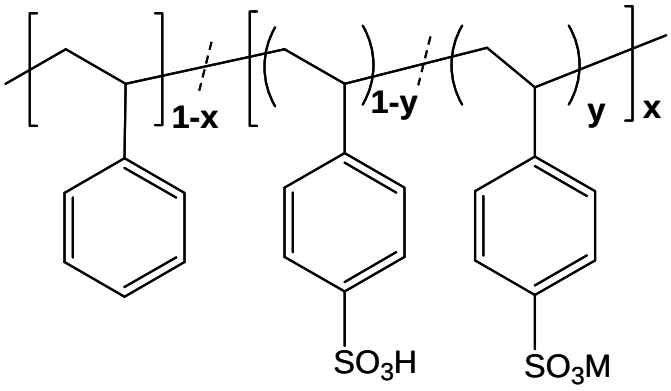

Scheme 3.1 Sulfonated polystyrene ionomers with different sulfonation levels (x = 0.035, 0.067, 0.095) and neutralized to different levels (y = 0, 25%, 50%, 75%, and 100%) with a metal cation (M = Na, Cs, or Zn).

3.2 Experimental Section

3.2.1 Materials and Sample Preparation: Atactic PS was purchased from Pressure Chemical (Mw = 123k g/mol, PDI =1.06). Sulfuric acid, acetic anhydride and dichloromethane were provided by Fisher Scientific. Sulfonated polystyrene (SPS) acid copolymers were prepared by sulfonation of polystyrene according to the procedures described in the literature.[16] Acetyl sulfate was synthesized by combining concentrated sulfuric acid with a solution of acetic anhydride in dichloromethane with acetic anhydride

in excess. Freshly prepared acetyl sulfate was added into the gently agitated solution 10% (w/v) of polystyrene in dichloromethane slowly at 40 °C. The sulfonation reaction proceeded for 4 h and was then terminated by the addition of methanol. The polymers were isolated by precipitation into methanol and then were washed several times with deionized water until the pH was the same as deionized water. The sulfonation levels were determined by Atlantic Microlab (Norcross, GA) using elemental sulfur analysis by combustion (3.5mol%, 6.7mol%, and 9.5 mol%). These sulfonation levels were consistent with the results of titration experiments, in which methanol solutions of SPS were titrated with 0.01N NaOH using the indicator thymol blue. The acid copolymers were dried under vacuum at 80 ^{o}C for at least three days and then at 110-120 ^{o}C for 1-2 day. The water contents of the acid copolymers were determined by coulometric Karl Fischer (KF) titration using Hydranal CG and Hydranal AG-H as KF reagents. The samples were dissolved in chloroform before titration. The water contents of all three acid copolymers were found to be less than 0.3 wt%. After measuring their glass transition temperatures by DSC, the acid copolymers were annealed at ~ T_g+20 ^{o}C for another day, and then hot pressed at 150 ^{o}C. These hot pressed samples were used for X-ray scattering, STEM imaging, and dielectric spectroscopy.

SPS acid copolymers were neutralized by first dissolving the copolymers in a mixture of toluene/methanol (90/10 v/v). A stoichiometric amount of metal acetate was dissolved in 50/50 v/v toluene/methanol and added slowly into the gently agitated P(S-SS_x) solution to achieve different percents of neutralization. The reaction was held at 50 ^{o}C for 2 hour. The neutralized ionomers were recovered by solvent casting at room temperature for 1-2 days and then dried under vacuum at 120 ^{o}C for at least 24 hours.

Ionomers with T_g around or above 120 ^oC (SPS6.7-*y*M and SPS9.5-*y*M) were further annealed at ~ T_g+20 ^oC for another day. The dried ionomer films were then hot pressed at 160 ^oC, and used for X-ray scattering, STEM imaging, and dielectric spectroscopy. All materials were stored in vacuum desiccators until characterization. Selected samples were sent to the Galbraith Laboratories for elementary analysis of metal cation (Zn, Na, or Cs) to determine the percent of neutralization. Within 5% of experimental error, the results were consistent with the expected neutralization levels. The ionomers are designated as SPS*x*-*y*M, where *x* is the mole fraction of sulfonation, *y* is the percent neutralization, and M is the metal cation (Na, Cs, or Zn). For example, SPS3.5-50%Zn is a SPS copolymer with 3.5 mol% acid and neutralized to 50% with Zn.

3.2.2 Thermal Analysis: Glass transition temperatures were determined by TA Instruments Q2000 differential scanning calorimeter from 40 °C to 180 °C during the second heating scan at a rate of 10 °C/min under a nitrogen flow of 50 mL/min. The T_g was taken as the inflection point in the DSC thermogram. Table 3.1 lists the T_g values for all the SPS acid copolymers and ionomers studied in this work.

3.2.3 Fourier Transform Infrared Spectroscopy (FTIR): The samples were hot pressed into thin films at 160 ^oC. FTIR spectra were collected at a resolution of 2 cm^{-1} using a Nicolet 450 FT-IR equipped with an MCT/B detector. A total of 256 scans were signal averaged for each spectrum at room temperature.

Table 3.1 Sulfonation levels determined by elementary analysis and Glass transition temperatures (T_g) determined by DSC for all the materials studied.

Sample	mol% Sulfonation	Cation	% Neutralization[a]	% Neutralization[b]	Tg (^oC)
Polystyrene	0	N/A	N/A	N/A	107.0
SPS3.5	3.5	H	0%		111.3
SPS3.5-50%Zn	3.5	Zn	50%		110.6
SPS3.5-100%Zn	3.5	Zn	100%		110.1
SPS3.5-50%Na	3.5	Na	50%		112.4
SPS3.5-100%Na	3.5	Na	100%		108.8
SPS3.5-50%Cs	3.5	Cs	50%		111.4
SPS3.5-100%Cs	3.5	Cs	100%		113.4
SPS6.7	6.7	H	0%		116.6
SPS6.7-50%Zn	6.7	Zn	50%		119.0
SPS6.7-100%Zn	6.7	Zn	100%		119.6
SPS6.7-50%Na	6.7	Na	50%		111.4
SPS6.7-100%Na	6.7	Na	100%		116.9
SPS6.7-50%Cs	6.7	Cs	50%		115.3
SPS6.7-100%Cs	6.7	Cs	100%		119.4
SPS9.5	9.5	H	0%		121.4
SPS9.5-25%Zn	9.5	Zn	25%	24%	116.7
SPS9.5-50%Zn	9.5	Zn	50%	49%	122.4
SPS9.5-75%Zn	9.5	Zn	75%	70%	131.1
SPS9.5-100%Zn	9.5	Zn	100%	99%	126.8
SPS9.5-50%Na	9.5	Na	50%		121.6
SPS9.5-100%Na	9.5	Na	100%		127.4
SPS9.5-50%Cs	9.5	Cs	50%		122.3
SPS9.5-100%Cs	9.5	Cs	100%	102%	130.3

[a] Theoretical neutralization level. [b] neutralization level determined by elementary analysis of metal cation.

3.2.4 X-ray Scattering: X-ray scattering experiments were performed with a multi-angle X-ray scattering (MAXS) apparatus using Cu X-ray generated from a Nonius FR 591 rotating-anode generator operated at 40 kV and 85 mA. The bright, highly collimated beam was obtained via Osmic Max-Flux optics and triple pin-hole collimation under vacuum. The scattering data were collected using a Bruker Hi-Star multiwire detector with sample-to-detector distances of 11, 54, and 150 cm. The isotropic 2-D data were integrated into 1D plot using *Datasqueeze* software.[17]

The scattering data of SPS ionomers at $q > 0.4$ nm^{-1} were modeled with:

$$I(q) = I_{KT}(q) + L_1(q) + L_2(q) + C \tag{3.1}$$

where $I_{KT}(q)$ is the Kinning-Thomas modified hard-sphere model[5, 18] used to interpret the ionomer peak, $L_1(q)$ and $L_2(q)$ are Lorentzian functions used to fit the two polystyrene-related peaks at 7 and 13 nm^{-1}, and C is a constant used to account for the instrumental background scattering, as previously reported.[19] The Kinning-Thomas model is the modified version of the Yarusso-Cooper model,[2, 5, 18] where the Percus-Yevick[20] total correlation function that accounts for correlations between all particles in the system was used instead of the Fournet[21] three-body interference function.

3.2.5 Scanning Transmission Electron Microscopy (STEM): STEM specimens were sectioned from solvent-cast, dried, and annealed ionomer films at room temperature using a Reichert-Jung ultramicrotome with a diamond knife to a nominal thickness of 30-50 nm. STEM experiments were performed using a JEOL 2010F field emission transmission electron microscope. High-angle annular dark field (HAADF) images were

recorded using a 0.7 nm STEM probe and a 70 μm condenser aperture at an accelerating voltage of 200 keV.

3.2.6 Broadband Dielectric Relaxation Spectroscopy (DRS): The DRS measurements were performed by our collaborators, Alicia Castagna and Professor James Runt from the Pennsylvania State University. Dielectric relaxation spectra were collected a Novocontrol GmbH Concept 40 broadband dielectric spectrometer. Frequency sweeps were performed isothermally from 10 MHz to 0.01 Hz in the temperature range of 30-220 °C under N_2 flow. The temperature step is typically set at 5 ^oC or less, and the sample is held at each temperature for 5 min before data collection. Temperature stability was controlled to within 0.2 °C. The thickness of the sample films were 0.1-0.3 mm. The films were sandwiched between brass electrodes of 2-cm diameter.

3.3 Results and Discussion

3.3.1 Structure and Dynamics of SPS Acid Copolymers: Figure 3.1 displays FTIR spectra in the frequency range of 900-1300 cm^{-1} for polystyrene (PS) and SPS acid copolymers. The bands at 1101 and 1127cm^{-1} arise from the in-plane skeletal vibration of benzene rings substituted by SO_3H and SO_3^-, respectively.[15, 22] Both bands appear upon sulfonation of PS, and the intensity of the bands increases with increasing sulfonation level. Note that these two bands are also sensitive to the environment, such as hydrogen-bonding interactions.[23] Interactions that polarize the acid proton will decrease the intensity of SO_3H absorbance and increase the intensity of SO_3^- absorbance.[23] The increase in the intensity of SO_3^- band with increasing sulfonation suggested that more sulfonic acids are polarized through hydrogen-bonding interactions

or acid aggregation. The band at 1174 cm^{-1} is attributed to the symmetric stretching of the S=O=S in SO_3H groups.[24]

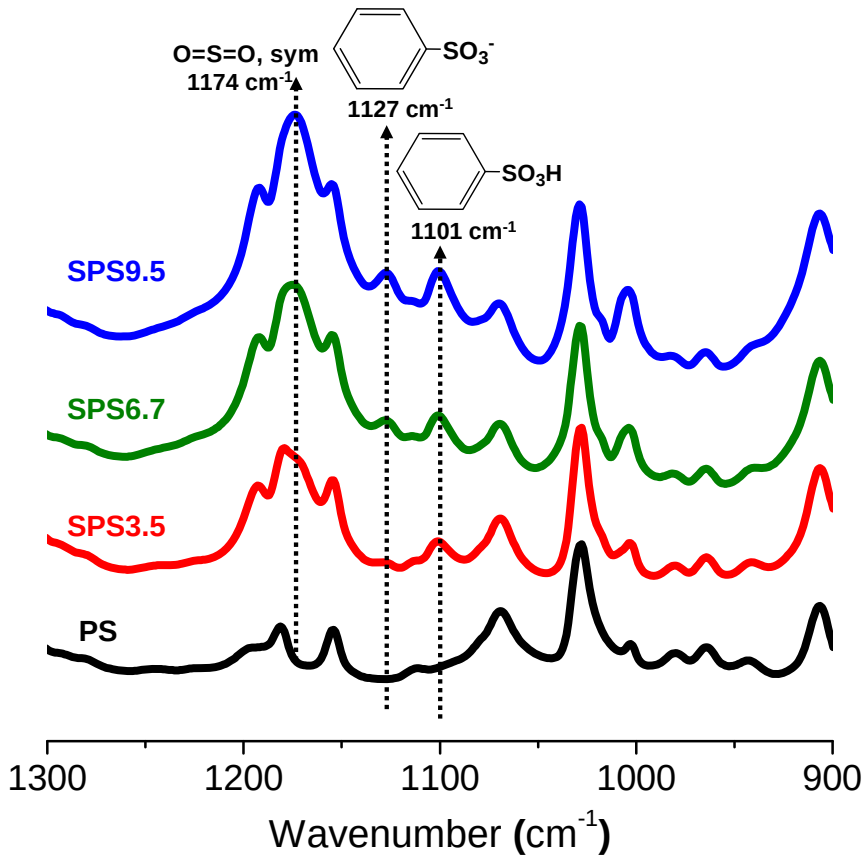

Figure 3.1 FTIR spectra of polystyrene (PS) and SPS*x* acid copolymers at sulfonation levels: *x%* = 3.5%, 6.7%, 9.5%. The spectra were vertically shifted for clarity.

X-ray scattering data from SPS acid copolymers with different sulfonation levels are shown in Figure 3.2. SPS9.5 and SPS6.7 show three isotropic peaks: polystyrene amorphous halo (~13 nm^{-1}), polystyrene polymerization peak (~7 nm^{-1}), and a third peak (1-2 nm^{-1}). The two higher angle peaks are typical features in the scattering patterns of amorphous polystyrene.[25] The third peak is at similar position as the ionomer peak typically seen in SPS ionomers. Previous research on the blend miscibility of PS with

P(S-SS$_x$) has estimated the styrene/styrenesulfonated segmental interaction parameter to be quite large: $\chi_{S/SS}>25$.[16] As a result, the energy penalty for dissolving the sulfonic acids in the polystyrene matrix is very high; thus, sulfonic acids are likely to self-assemble into nanoscale acid aggregates and give rise to the scattering peak at 1-2 nm^{-1}. The intensity of the acid aggregation peak decreases with decreasing sulfonation level. As the sulfonation level decreases to 3.5 mol%, the acid aggregate peak disappears, but the scattering intensity at lower *q* is still much stronger than the pure polystyrene. It is possible that SPS3.5 might contain a small fraction of acid aggregates. Due to the low quantity and limited electron density contrast between the acid aggregates and polymer matrix, these acid aggregates do not give rise to a scattering peak. It is expected that the number of acid aggregates increases with sulfonation, as well as the percentage of acid groups that participate in the aggregates. Yarusso and Copper observed the acid aggregation peak in SPS acid with sulfonation level of 3.37, 5.55, and 6.91 mol%, and the peak intensity increases with sulfonation level.[26] When sulfonation level is 1.68 mol%, the peak appeared as a shoulder.[26] However, Weiss *et al.* did not observe any the acid aggregation peak in SPS acid with sulfonation level of either 5.5 or 11 mol%.[3] The discrepancy between these results is probably caused by different sample preparation conditions. The SPS acid studied by Yarusso and Cooper might contain some residual solvent (DMSO, b.p. = 180 ^{o}C), as Weiss *et al.* suggested, which enhanced the contrast between the acid aggregates and polystyrene matrix.[26] While the absence of acid aggregation peak in Weiss's SPS acids could be attributed to the lack of annealing.[3] The SPS acid copolymers studied in this chapter have been dried above the boiling point of solvents for several days, annealed above T_g for at least 24 hours, and hot pressed. Thus,

the structures and properties obtained from our study should represent the nature of the materials.

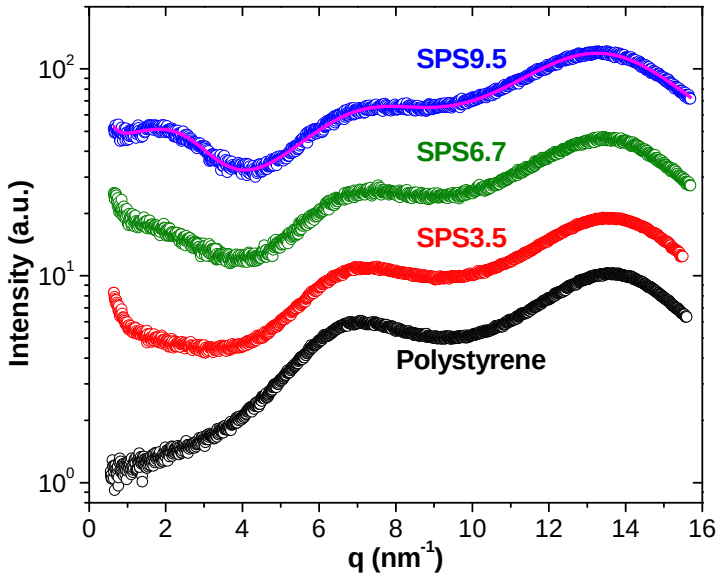

Figure 3.2 X-ray scattering intensity vs. scattering vector q for polystyrene and SPSx acid copolymers at sulfonation levels: $x\%$ = 3.5%, 6.7%, 9.5%. The purple line is the best fit of the scattering data from SPS9.5 using Eq. 3.1. The scattering data were vertically shifted for clarity.

The real (dielectric constant, ε') and imaginary (dielectric loss, ε") parts of the complex dielectric constant ($\varepsilon^* = \varepsilon' + i\varepsilon''$) contain the same information and are related to each other by the Kramers-Kronig relationships:[27]

$$\varepsilon'(\omega_o) = \varepsilon_\infty + \frac{2}{\pi}\int_0^\infty \varepsilon''(\omega)\frac{\omega}{\omega^2 - \omega_o^2}d\omega \tag{3.2}$$

$$\varepsilon''(\omega_o) = \frac{\sigma_{DC}}{\varepsilon_V \omega_o} + \frac{2}{\pi}\int_0^\infty \varepsilon'(\omega)\frac{\omega}{\omega^2 - \omega_o^2}d\omega \tag{3.3}$$

where $\varepsilon_\infty = \lim_{\omega \to \infty} \varepsilon'(\omega)$ is the dielectric constant at limiting high frequency, ε_V refers to the vacuum permittivity, ω is the angular frequency, ω_o is the angular frequency of the applied electric field, and σ_{DC} is the DC conductivity (S/cm). The analysis and discussion of the relaxation properties are mainly based on the dielectric loss spectra, because the loss spectra often contain more details and therefore allow a better evaluation of overlapping peaks.[27]

Figure 3.3a shows the typical dielectric loss as a function of frequency for SPS with different sulfonation levels at T_g + 50 ^oC. The large values of dielectric loss at low frequencies are due to the ionic conduction (first term in Eq. 3.3), which mask any low-frequency loss peaks of dipolar origin. The "conduction-free" loss can be calculated from the dielectric constant using numerical approximations. The derivative formalism, where the derivative of the dielectric constant is taken with respect to the natural logarithm of the angular frequency, was chosen to obtain the "conduction free" loss:[27, 28]

$$\varepsilon''_D = -\frac{\pi}{2}\frac{\partial \varepsilon'(\omega)}{\partial \ln \omega} \tag{3.4}$$

This method has been shown to be a good approximation of the conduction-free dielectric loss, especially for broad relaxation processes.[28] The conduction-free loss spectra of SPS are shown in Figure 3.3b, and exhibit two main relaxation processes at T_g+50 ^oC: α at higher frequency and process I at lower frequency. The high-frequency process, α, corresponds to the segmental relaxation of the polymer. The lower-frequency process, I, could be associated with the dynamics of disassociation and reassociation of hydrogen bonded sulfonic acid groups. More analysis is currently underway to verify the origin of the process I.

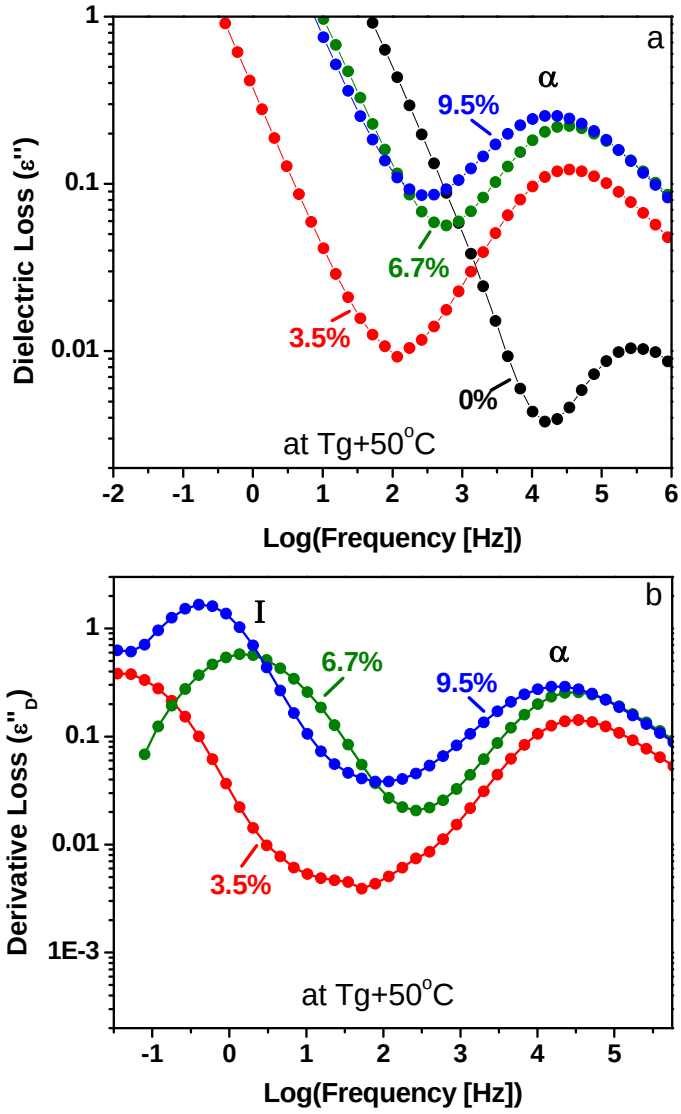

Figure 3.3 (a) dielectric loss and (b) derivation spectra at T_g + 50 °C for polystyrene and SPS acid copolymers with different sulfonation levels.

The relaxations in the dielectric loss or derivative spectra can be fitted to the appropriate form of Harvriliak-Negami function:[29]

$$\varepsilon^*_{HN}(\omega) = \frac{\Delta\varepsilon}{(1+(i\tau_{HN}\omega)^a)^b} \tag{3.5}$$

where $\Delta\varepsilon$ is the relaxation strength, a and b ($0 < a,\ ab \le 1$) are shape parameters describing symmetric and asymmetric broadening of the complex dielectric function, and τ_{HN} is the characteristic relaxation time related to the frequency at the maximum in the loss ($f_{\max}$) by:[29]

$$f_{\max} = \frac{1}{2\pi\tau_{\max}} = \frac{1}{2\pi\tau_{HN}}\left[\frac{\sin(\pi a/(2+2b)}{\sin(\pi ab/(2+2b))}\right]^{1/a} \tag{3.6}$$

The relaxation frequency $f_{\max}$ and strength $\Delta\varepsilon$ of the α process are plotted in Figure 3.4. The α process is well described by the Vogel-Fulcher-Tammann (VFT) equation:

$$f_{\max} = f_o \exp(-\frac{B}{T - T_o}) \tag{3.7}$$

where f_o and B are constants, and T_o is the Vogel temperature. The fits are indicated by lines in Figure 3.4a, and the fitting parameters are listed in Table 3.2. The dynamical T_g (T_g^{DRS}) were obtained by extrapolating the VFT fit of the segmental relaxation to 100s, i.e. $\tau_{\max} = 100\text{s}$. The T_g^{DRS} values are consistent with DSC results (T_g^{DSC}), Table 3.2. Sulfonation greatly slows the dynamics of segmental relaxation. The frequency position shifts to lower value (longer time) as the sulfonation level increases, consistent with the fact that T_g of SPS increases with increasing sulfonation level, Table 3.2. The relaxation strength $\Delta\varepsilon$ increases with increasing sulfonation level, Figure 3.4b. As $\Delta\varepsilon$ contains a contribution from the polar sulfonic acid group, increasing sulfonation effectively increases the number of dipoles in the system. Note that the increase in $\Delta\varepsilon$ is not linear with percent sulfonation, which could be attributed to the different percentages of sulfonic acids that form acid aggregates. It is expected that the α process mainly arise

from the segmental relaxation of polystyrene and sulfonated polystyrene with isolated sulfonic acid; thus, the aggregation of sulfonic acids would reduce the relaxation strength of the α process.

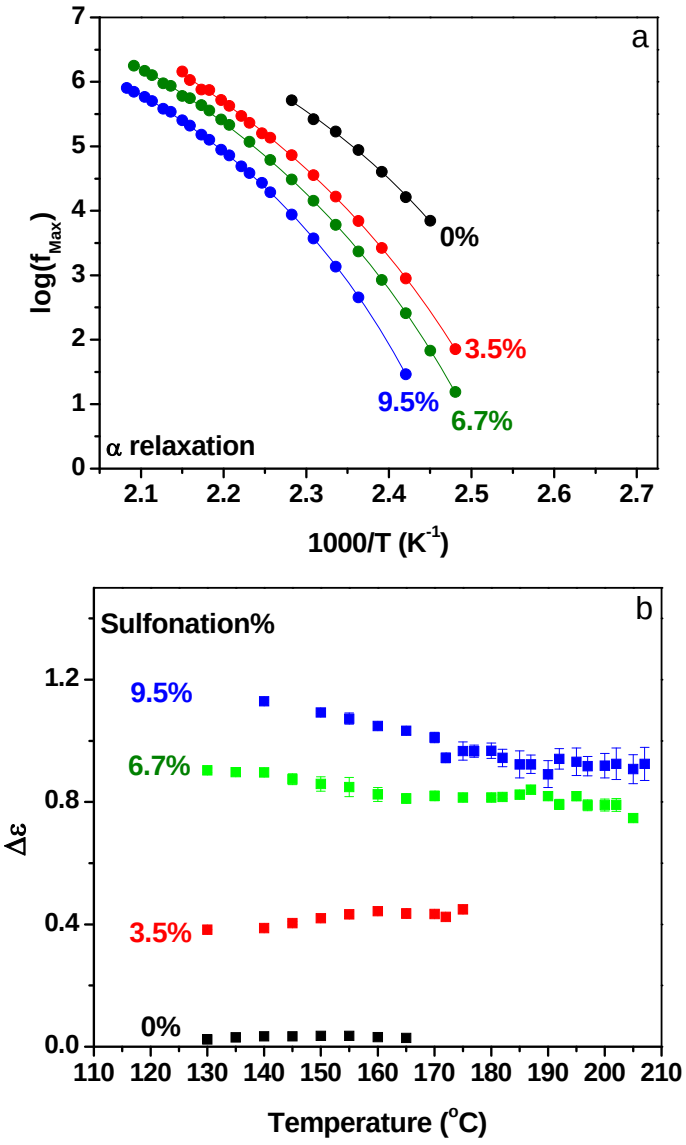

Figure 3.4 (a) relaxation frequency of the α process as a function of inverse temperature and (b) dielectric strength ($\Delta\varepsilon$) as a function of temperature for poly polystyrene and SPS acid copolymers with different sulfonation levels. Lines in (a) indicate fits of the VFT equation (Eq. 3.7) to the data.

Table 3.2 VFT Fitting Parameters and Glass Transition Temperatures for PS and SPS acid copolymers.

	VFT Fitting Parameters				
Sample	B (^{o}C)	T_o (^{o}C)	Log(f_o)	T_g^{DRS} (^{o}C)	T_g^{DSC} (^{o}C)
PS	1119	60	10.3	102	107
SPS3.5	1367	55	11.3	112	111
SPS6.7	1267	62	10.9	117	117
SPS9.5	907	80	10.0	126	121

3.3.2 Structure and Dynamics of Zn-neutralized SPS Ionomers: Figure 3.5 displays FTIR spectra in the frequency range of 900-1300 cm^{-1} for SPS9.5-*y*Zn at different neutralization levels (*y* = 0, 25%, 50%, 75%, and 100%). The bands at ~ 1228 and 1039 cm^{-1} correspond to the asymmetric and symmetric stretching vibrations of S-O bond in $-SO_3M$, respectively.[15] The bands at 1127 and 1009 cm^{-1} result from the in-plane skeletal vibration of benzene rings substituted by SO_3^- and SO_3M, respectively.[15] The intensity of those four bands increases with increasing neutralization level, indicating successful neutralization of SPS. The band at 1101 cm^{-1} is attributed to the in-plane skeletal vibration of benzene rings substituted by SO_3H.[22] The intensity of this band decreases with increasing neutralization level.

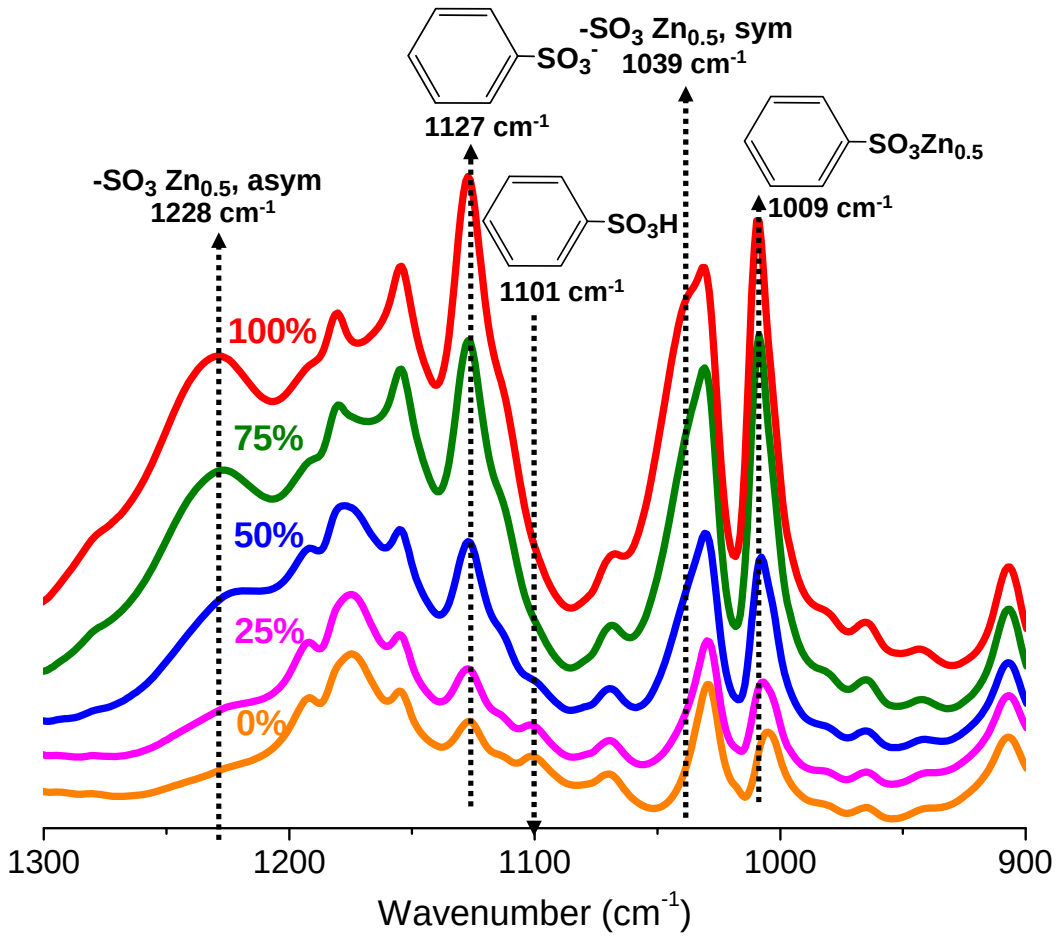

Figure 3.5 FTIR spectra of SPS9.5-yZn at different neutralization levels: 0%, 25%, 50%, 75%, and 100%. The spectra were vertically shifted for clarity.

HAADF STEM images of SPS ionomers show spherical, uniformly distributed bright features, corresponding to cation-rich ionic aggregates within a matrix of lower average atomic number. Representative STEM images for SPS6.7-100%Zn and SPS9.5-100%Zn are shown in Figure 3.6. The diameters of the ionic aggregates were determined by the full width at half maximum (FWHM) of the Gaussian functions fit to the intensity profiles taken across individual bright features.[19] The average diameters and their standard deviations for four SPS ionomers are shown in Table 3.3. Taking into account

the extensive projection overlap in the STEM images and the limit of instrumental resolution, STEM images indicate that the diameters of ionic aggregates are ~ 2 nm and independent of the sulfonation level.

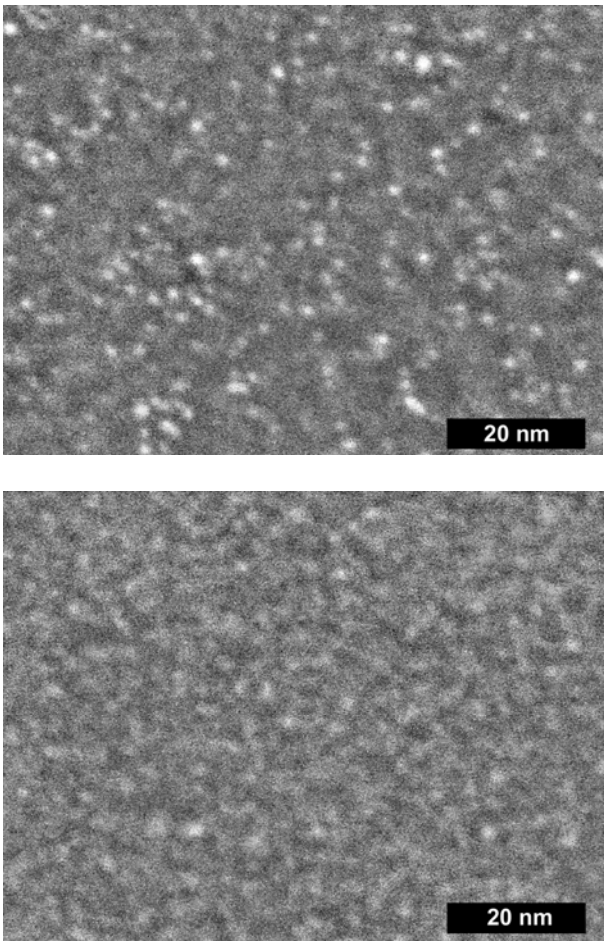

Figure 3.6 HAADF STEM images of SPS6.66-100%Zn (top) and SPS9.45-100%Zn (bottom) show a uniform distribution of spherical ionic aggregates.

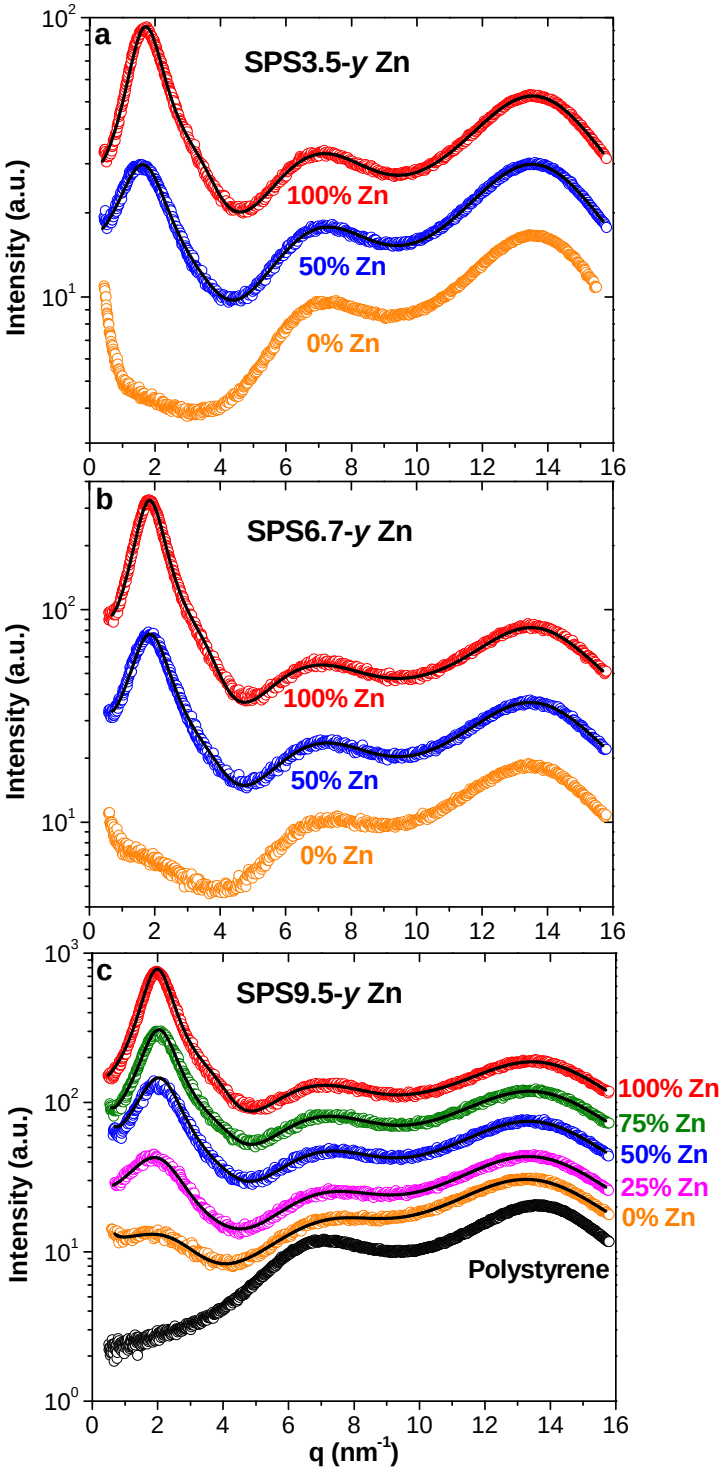

Figure 3.7 X-ray scattering intensity vs. scattering vector q for a) SPS3.5-*y*Zn; b) SPS6.7-*y*Zn; c) polystyrene and SPS9.5-*y*Zn. The lines are the best fit of the scattering data using Eq. 3.1. The scattering data were vertically shifted for clarity.

Figure 3.7 displays the X-ray scattering data from the polystyrene and SPS*x*-*y*Zn. The ionomer peak intensity increases with increasing neutralization level, which is expected since more high-atomic number cations (Zn) are added into the ionomer as the neutralization level increases. (Because the data are vertically shifted for clarity, compare the ionomer peak height to the amorphous peak height to observe changes in intensity). The ionomer peak position is almost independent of the neutralization level.

Table 3.3 Diameters of ionic aggregates obtained from STEM imaging and X-ray scattering.

Ionomer	D_{STEM} (nm)	$2R_{1,\ X\text{-}ray}$ (nm)[a]
SPS3.5-100%Cs	2.1 ± 0.5	1.90 ± .002
SPS6.7-100%Zn	1.8 ± 0.4	1.72 ± .003
SPS9.5-100%Zn	1.8 ± 0.5	1.67 ± .002
SPS9.5-100%Cs	2.0 ± 0.5	1.83 ± .004

[a] The standard deviations for $\mathbf{2R_{1,\ X\text{-}ray}}$ are obtained when fitting Eq. 1 to the X-ray scattering data. These values are only indicative of the numerical quality of the fits and not the uncertainties associated with the scattering model.

Given that STEM imaging results have verified SPS ionomers formed spherical ionic aggregates, and to facilitate the interpretation of X-ray scattering data, the ionomer peaks of SPS ionomers were fitted with the Kinning-Thomas modified hard-sphere model. The model assumes that the ionomer peak arises from the interparticle scattering from monodisperse, spherical ionic aggregates homogeneously distributed in the polymer matrix of lower electron density. The model uses four parameters: the radius of ionic aggregates R_1, the radius of closest approach R_{CA}, the number density of the aggregates N_p, and the amplitude A.[5] The model fits the scattering data well, as shown by the black

line in Figure 3.7a. Table 3.3 compares the diameter of the ionic aggregates measured by STEM (D_{STEM}) and X-ray scattering ($2R_{1,\ X\text{-}ray}$), and finds good agreement. Previous study on SPS1.9-100%M ionomers by Zhou *et al.* also showed consistent size and number density of ionic aggregates between STEM and X-ray scattering.[5]

The $2R_1$ and $2R_{CA}$ values for SPS*x*-*y*Zn are plotted as a function of neutralization level, Figure 3.8a. All Zn-ionomers exhibit similar size ($2R_1$) that is independent of acid content and neutralization level. Previous study on SMAA-Cu ionomers[30] and SPS-Zn ionomers[2] also showed that the size of the ionic aggregates is independent of acid content and neutralization level. These results suggest that the size of ionic aggregates in those strongly segregating ionomers is mainly controlled by the chemical structure of the acid copolymer, i.e. polymer backbone, and acid type. The distance of closest approach between the aggregates ($2R_{CA}$) increases with increasing neutralization level, which will be discussed later along with the composition inside ionic aggregates. On the other hand, the $2R_{CA}$ value decreases very slightly with increasing acid content from 3.5% to 9.5%. Figure 3.8b displays the number density of ionic aggregates (N_p), which increases with increasing sulfonation level, as expected. However, N_p shows a much weaker dependence on the neutralization level. In fact, for SPS9.5-*y*Zn, the N_p decreases upon converting 25% of H^+ to Zn^{2+}, increases as the neutralization level increases to 50%, and then remains almost unchanged when the neutralization level further increases to 75% or 100%. The weak dependence of N_p on neutralization level suggests that the composition inside ionic aggregates changes with neutralization level.

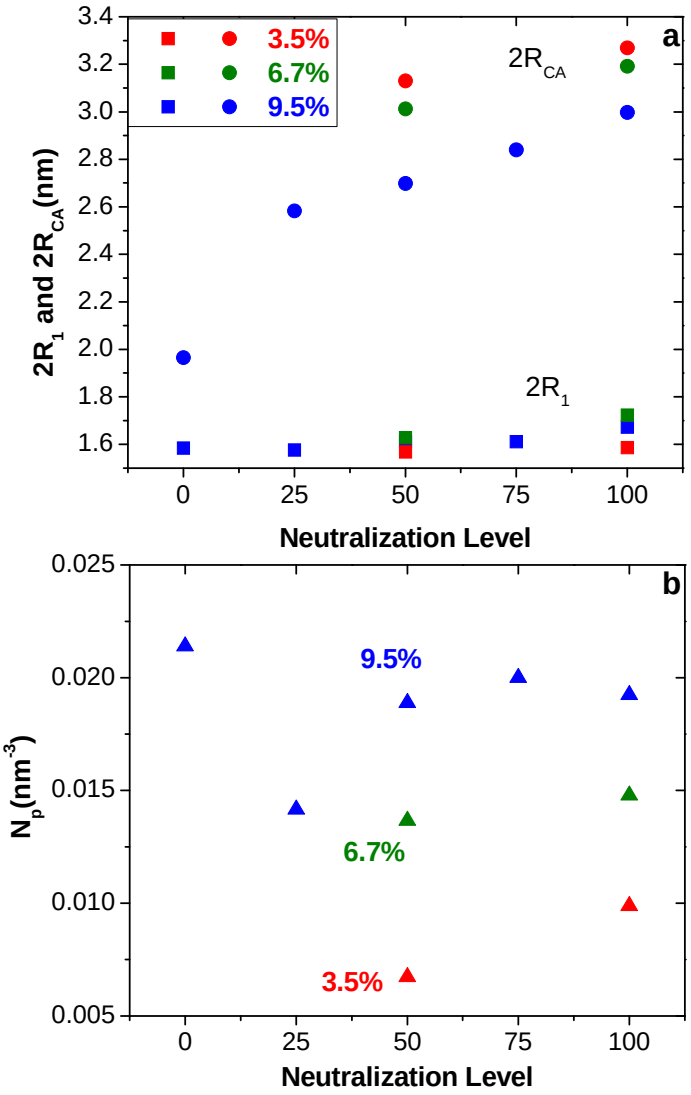

Figure 3.8 a) R_1 (■) and R_{CA} (●) determined by X-ray scattering as a function of neutralization level for SPS*x*-*y*Zn. b) The number density of the ionic aggregate (N_p) as neutralization level for SPS*x*-*y*Zn.

To understand whether the electron density inside the ionic aggregates changes, the number of cations inside the aggregates was calculated separately using R_1 or N_p. The number of cation calculated from R_1, $N(cation, R_1)$, is based on the assumption that ionic aggregates consist entirely of ionic groups:[11]

$$N(cation,\ R_1) = \frac{4}{3}\pi R_1^3 \cdot \left(\frac{n_{sulfate}}{n_{ion\ pair}} \cdot \frac{N_A \rho_{sulfate}}{M_{sulfate}} \right) \tag{3.8}$$

where $n_{sulfate}$ is the number of atoms in metal sulfate, $n_{ion\ pair}$ is the number of atoms in metal sulfonate, and $\rho_{sulfate}$ and $M_{sulfate}$ are the density and formula molar mass of zinc sulfate, respectively. The number of cations per aggregate based on N_p, *N(cation, N_p)*, is calculated based on the composition of acid copolymers. It assumes that all the ions are incorporated into the ionic aggregates, thus representing the upper limit of cation available in a average volume of V_p=1/N_p:[11]

$$N(cation,\ N_p) = \frac{1}{p}\frac{N_A \rho_{SPS}}{M_{SPS}} \cdot \frac{1}{N_p} \cdot \phi_{acid} \cdot \frac{y}{100} \tag{3.9}$$

where p is the valency number, ρ_{SPS} and M_{SPS} are the density and the monomeric molar mass of SPS, respectively, ϕ_{acid} is the volume fraction of sulfonic acid in the SPS, and y is the percent of neutralization.

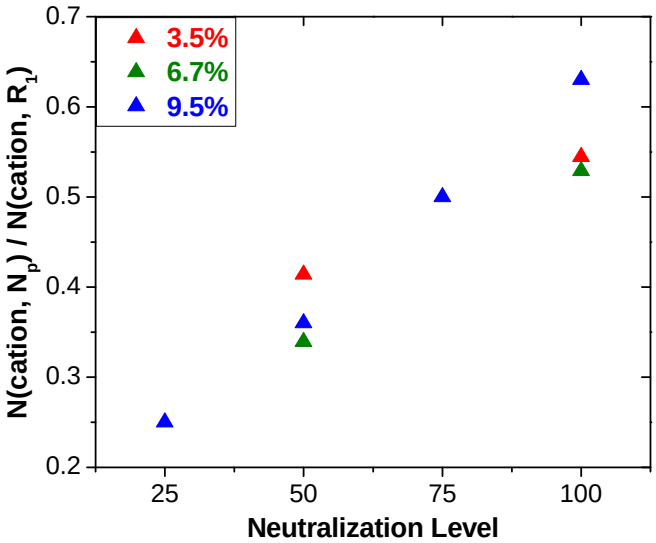

Figure 3.9 Occupancy rate determined by *N(cation, N_p)/N(cation, R_1)* as a function of neutralization level for SPS*x*-*y*Zn.

The occupancy ratio (r) determined by $r = N(cation,\ N_p) / N(cation,\ R_1)$ provides useful information regarding the composition of the ionic aggregates.[31] Figure 3.9 shows the occupancy ratio (r) as a function of neutralization level for SPS9.5-*y*Zn. If $r>1$, the volume of the ionic aggregates as determined by R_1 cannot accommodate all ionic groups that are available in V_p, and thus not all ionic groups are incorporated into the aggregates. There are some isolated metal sulfonates in the polymer matrix. When $r<1$, there are not enough ionic groups in V_p to fill the ionic aggregate of radius R_1. This indicates that the composition of ionic aggregates is less dense than metal sulfonate. The occupancy ratio in these SPS*x*-*y*Zn ionomers is less than 1 at all sulfonation and neutralization levels. The uncertainty associated with R_1 and N_p is estimated to be less than 10% and 20%, respectively. But these uncertainties are systematic and inherent with the structural model, so that the trend of change in r values is reliable. The r value increases with neutralization level, suggesting that more $Zn(SO_3)_2$ groups are incorporated into the ionic aggregates of similar sizes as neutralization level increases, i.e. the composition of ionic aggregates becomes more ionic. Zhou et al.[5] calculated $N(cation, R_1)$ and $N(cation, N_p)$ for SPS1.9-125%M (M = Cs, Na, Cu, Mg, and Zn), and found that $N(cation, R_1) \approx N(cation, N_p)$ for all cations. Since the SPS1.9 acid copolymers were over-neutralized with metal cation (125%), the ionic aggregates are able to achieve $r\approx1$, which is consistent with our findings. The ionic aggregates in partially sulfonated SPS*x*-*y*Zn ($0<y<100$) ionomers likely contain un-neutralized acids. As shown previously (Figure 3.2), sulfonic acids in SPS9.5 can also form aggregates even though there is no metal cation present in the system, which makes perfect sense, since the acid proton can hydrogen bond to the SO_3 oxygens but not to the hydrocarbon PS.

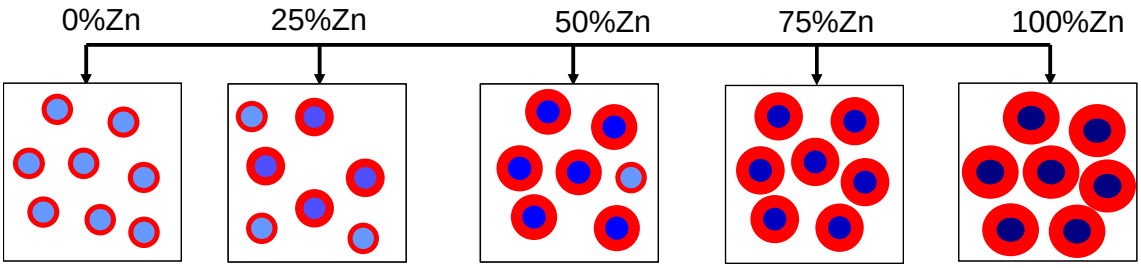

Figure 3.10 Schematic view of the morphological change with neutralization level for SPS9.5-*y*Zn. The blue circle represents aggregates of SO_3H and $Zn(SO_3)_2$. The diameter of the blue circle is $2R_1$, which is independent of neutralization level. As the neutralization level increases, the blue color gets dark, representing increasing ionic density inside the aggregates. The red corona represents the layer of hydrocarbon around aggregates which defines the radius of closest approach, R_{CA}. R_{CA} increases with increasing neutralization level.

Based on the analysis above, the evolution of morphology with neutralization level for SPS9.5-*y*Zn is illustrated in Figure 3.10. The sulfonic acids in SPS9.5 form aggregates due to the large energy penalty of dissolving the acid in polystyrene matrix. Conversion of H^+ to Zn^{2+} results in the formation of Zn-rich ionic aggregates, which contribute the most to the ionomer peak in X-ray scattering profile. However, there might still be a small fraction of aggregates that consist mainly of sulfonic acids. In addition, the Zn-rich ionic aggregates in SPS9.5-25%Zn also contain un-neutralized sulfonic acids. As the neutralization level increases to 50%, more Zn-rich ionic aggregates form, as shown by the increase of N_p. Further increasing the neutralization level does not change N_p much. Instead, the additional Zn^{2+} cations are predominately incorporated into the existing ionic aggregates, increasing the occupancy ratio (r) of ionic

aggregates. As the sulfonic acids are converted to $Zn(SO_3)_2$ with stronger ionic interaction, the radius of closest approach between ionic aggregates, $2R_{CA}$, also increases, as shown in Figure 3.8a.

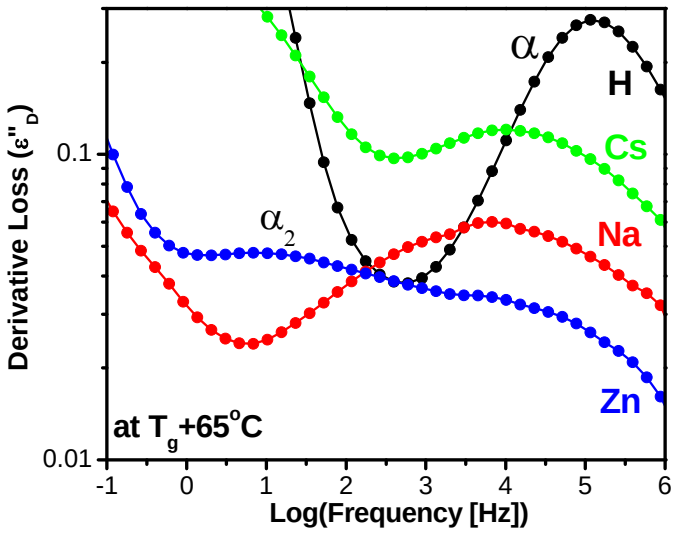

Figure 3.11 Derivative spectra at T_g+65 °C for SPS9.5-100%M, M=H, Na, Cs, or Zn.

Figure 3.11 shows the derivative spectra of SPS9.5-100%M (M = H, Na, Cs, or Zn) at T_g+65 °C. The α process broadens as the ionic association strength increases from H^+ to Cs^+ to Na^+. For divalent cation Zn^{2+}, a second relaxation, α_2, becomes evident at lower frequency. It should be noted that the α_2 process might also be present in the Na- and Cs- neutralized SPS ionomers. Due to the proximity in the frequency positions of the α and α_2 processes, the α_2 process is obscured by the broad α process. Changing the cation from monovalent to divalent (Zn^{2+}) shifts the α_2 process to lower frequency, indicating stronger binding energy of Zn^{2+}-SO_3^-. Zn^{2+} has two positive charges and smaller effective ionic radius (0.74Å) compared to Na^+ (1.02 Å) or Cs^+ (1.67Å), thus the charge density of Zn^{2+} is the highest among three cations.

To understand the origin of the α_2 relaxation, the α and α_2 processes of SPS9.5-*y*Zn (*y* = 0%, 25%, 50%, 75%, and 100%) were investigated as a function of neutralization level, Figure 3.12. As *y* increases, the α relaxation shifts to lower frequency (Figure 3.12a) and decreases in strength (Figure 3.12b). It is well-known that ionic aggregates act as effective crosslinks and greatly slow down the dynamics of polymer matrix between the aggregates.[32] Since the α relaxation mainly arises from the segmental motion of polystyrene in the region farther away from the ionic aggregates, the decreases in the α relaxation strength suggests that more polystyrene segments are slowed down by the ionic aggregates and do not participate in the relatively faster α relaxation, as *y* increases. The normalized α process displayed in Figure 3.12c clearly shows the broadening of α process towards lower frequency and appearance of the α_2 process as the neutralization level increases. The strength of the α_2 increases with neutralization level (Figure 3.12d), and becomes the dominant process as the neutralization level reaches 100%. From our findings by X-ray scattering above, the R_{CA} increases with increasing neutralization level in SPS9.5-*y*Zn while R_1 remains almost unchanged. Thus, the α_2 process could be attributed to the slower relaxation of the restricted region around the aggregates.

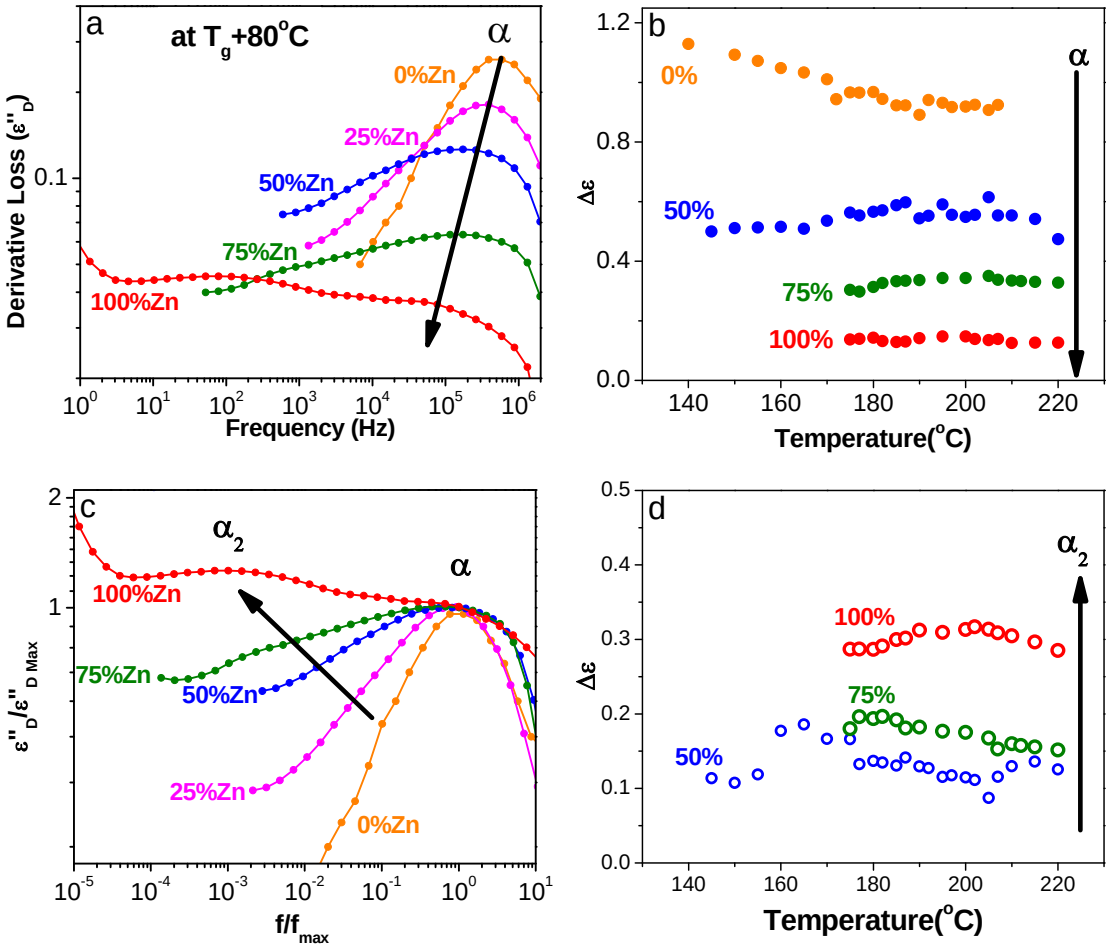

Figure 3.12 (a) derivative loss, (b) relaxation strength of α process, (c) normalized derivative loss (by $\varepsilon''_{D\ \max}$ and $f_{\max}$), and (d) relaxation strength of α_2 process for SPS9.5-*y*Zn at different neutralization levels (*y* = 0%, 25%, 50%, 75%, and 100%).

To facilitate our understanding of the α_2 process, the region of restricted mobility surrounding each aggregate are calculated. The total volume% of ionic aggregates (V_A%) and restricted region around the aggregates (V_R%) can be estimated using the following equations:

$$V_A\% = \frac{4}{3}\pi R_1^3 \cdot N_p \tag{3.10}$$

$$V_R\% = \frac{4}{3}\pi(R_{CA}^3 - R_1^3)\cdot N_p \tag{3.11}$$

Figure 3.13 shows that the V_A% is independent of neutralization level in SPS9.5-*y*Zn. The volume fraction of polystyrene matrix decreases almost linearly with increasing neutralization level, while V_R% shows the opposite trend. This is consistent with our assignment of the α and α_2 processes. As the neutralization level increases, more and more polystyrene chains are involved in the slower dynamics, resulted in increasing strength of α_2 process.

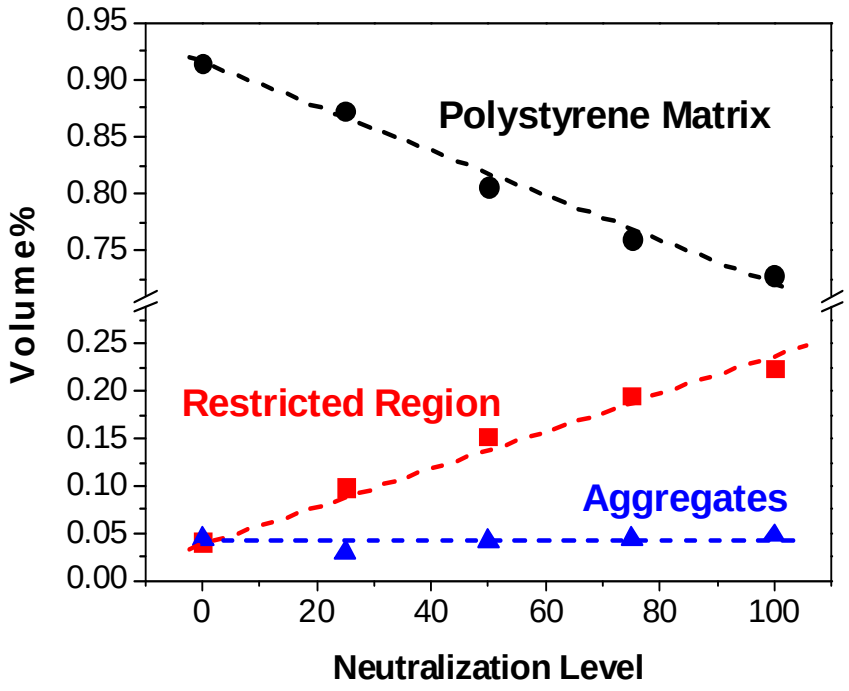

Figure 3.13 Volume fraction of ionic aggregates (V_A%), restricted region surrounding the aggregates (V_R%), and polystyrene matrix (1-V_A%-V_R%) as a function of neutralization level for SPS9.5-*y*Zn.

The V_R% in SPS9.5-100%Zn is ~ 22% and V_R%+ V_A% is ~ 27%, thus the volume fraction of restricted region is still much less than that of the unrestricted matrix region.

However, the relaxation strength of α_2 process is much larger than the α process in the fully neutralized ionomers. Two possibilities are explored to explain this discrepancy. One might argue that the radius of closest approach R_{CA} from the modified hard-sphere model underestimates the amount of polymer matrix under restricted region. As the distance of closest approach distance mainly provides the steric limitation on the relative position of two nearby ionic aggregates, it might not represents the dynamic properties. Eisenberg *et al.* has proposed that the thickness of restricted region to be approximately on the order of the persistent length of the polymer chain, which is ~1nm for polystyrene.[32] From X-ray scattering, R_1=0.84 nm for SPS9.5-100%Zn, such that the radius of the restricted region would be 1.84 nm, which is larger than R_{CA} (1.5 nm) obtained from X-ray scattering. Based on Eq. 3.11 & 3.12, the high values of V_R% (45%) and V_R%+V_A% (50%) are insufficient to explain the much stronger α_2 process than α process in SPS9.5-100%Zn. Another possibility is that the slower α_2 process also involves the ionic groups inside the aggregates. The relatively larger dipoles of ionic groups could account for the high relaxation strength of the α_2 process while occupying a smaller volume fraction. As the ionic groups are pendant to the phenyl rings of polystyrene, the relaxation of the polystyrene segments adjacent to aggregates could cause the local motion of ionic groups inside the aggregates. As a result, the α_2 process is attributed to the relaxation of slowed-down dynamics of the polymer chain in the restricted region and some localized ion motion within the aggregates.

3.4 Conclusion

The morphology and dynamics of SPS acid copolymers and ionomers have been investigated as a function of acid content and neutralization level by FTIR, X-ray scattering, HAADF STEM, and broadband DRS. Sulfonic acids groups in the SPS6.7 and SPS9.5 acid copolymers form aggregates due to the large energy penalty of dissolving the acid in the polystyrene matrix. Sulfonation increases the relaxation time and strength of the α process, which arises from the segmental relaxation of polystyrene and sulfonated polystyrene with isolated -SO_3H. The increase in the relaxation strength is not linear with percent sulfonation, due to different extents of acid aggregation.

For Zn-neutralized SPS ionomers, the size of the ionic aggregates is almost independent of acid content and neutralization level. The distance of closest approach between aggregates ($2R_{CA}$) increases linearly with increasing neutralization level in SPS9.5-*y*Zn, which can be explained by the increasing number of Zn^{2+} inside the aggregates. The ionic aggregates in partially neutralized ionomers contain unneutralized acid. When the acids are converted to divalent Zn^{2+}, the much stronger electrostatic interactions between the ionic groups enhanced the restriction in the mobility of the chains around the aggregates. As a result, the region of restricted mobility increases in volume% as the neutralization increases. DRS revealed a secondary process, α_2, at a slightly lower frequency than the α process. The α_2 process mainly arises from the segmental relaxation of polystyrene in the region of restricted mobility around the aggregates and might also involve some localized ion motion. The strength of α process decreases with increasing neutralization level of SPS9.5-yZn, while the α_2 process shows the opposite trend. Those findings correlate well with the morphology of SPS9.5-yZn.

3.5 References

1. Earnest, T. R.; Higgins, J. S.; Handlin, D. L.; Macknight, W. J. *Macromolecules* **1981,** 14, (1), 192-196.

2. Yarusso, D. J.; Cooper, S. L. *Macromolecules* **1983,** 16, (12), 1871-1880.

3. Weiss, R. A.; Lefelar, J. A. *Polymer* **1986,** 27, (1), 3-10.

4. Ding, Y. S.; Hubbard, S. R.; Hodgson, K. O.; Register, R. A.; Cooper, S. L. *Macromolecules* **1988,** 21, (6), 1698-1703.

5. Zhou, N. C.; Chan, C. D.; Winey, K. I. *Macromolecules* **2008,** 41, (16), 6134-6140.

6. Li, Y. J.; Peiffer, D. G.; Chu, B. *Macromolecules* **1993,** 26, (15), 4006-4012.

7. Li, C.; Register, R. A.; Cooper, S. L. *Polymer* **1989,** 30, (7), 1227-1233.

8. Oconnell, E. M.; Root, T. W.; Cooper, S. L. *Macromolecules* **1994,** 27, (20), 5803-5810.

9. Oconnell, E. M.; Root, T. W.; Cooper, S. L. *Macromolecules* **1995,** 28, (11), 3995-3999.

10. OConnell, E. M.; Peiffer, D. G.; Root, T. W.; Cooper, S. L. *Macromolecules* **1996,** 29, (6), 2124-2130.

11. Weiss, R. A.; Fitzgerald, J. J.; Kim, D. *Macromolecules* **1991,** 24, (5), 1071-1076.

12. Colby, R. H.; Zheng, X.; Rafailovich, M. H.; Sokolov, J.; Peiffer, D. G.; Schwarz, S. A.; Strzhemechny, Y.; Nguyen, D. *Phys. Rev. Lett.* **1998,** 81, (18), 3876-3879.

13. Weiss, R. A.; Yu, W. C. *Macromolecules* **2007,** 40, (10), 3640-3643.

14. Tierney, N. K.; Register, R. A. *Macromolecules* **2003,** 36, (4), 1170-1177.

15. Atorngitjawat, P.; Runt, J. *Macromolecules* **2007,** 40, (4), 991-996.

16. Zhou, N. C.; Xu, C.; Burghardt, W. R.; Composto, R. J.; Winey, K. I. *Macromolecules* **2006,** 39, (6), 2373-2379.

17. Heiney, P. A. *Commission on Powder Diffraction Newsletter* **2005,** 32, 9-11.

18. Kinning, D. J.; Thomas, E. L. *Macromolecules* **1984,** 17, (9), 1712-1718.

19. Benetatos, N. M.; Heiney, P. A.; Winey, K. I. *Macromolecules* **2006,** 39, (16), 5174-5176.

20. Percus, J. K.; Yevick, G. J. *Phys. Rev.* **1958,** 110, (1), 1-13.

21. Fournet, G. *Acta Crystallogr.* **1951,** 4, 293-301.

22. Zhou, N. C.; Burghardt, W. R.; Winey, K. I. *Macromolecules* **2007,** 40, (17), 6401-6405.

23. Lu, X. Y.; Weiss, R. A. *Macromolecules* **1995,** 28, (9), 3022-3029.

24. Chen, W. J.; Sauer, J. A.; Hara, M. *Polymer* **2003,** 44, (25), 7729-7738.

25. Ayyagari, C.; Bedrov, D.; Smith, G. D. *Macromolecules* **2000,** 33, (16), 6194-6199.

26. Yarusso, D. J.; Cooper, S. L. *Polymer* **1985,** 26, (3), 371-378.

27. Wubbenhorst, M.; van Turnhout, J. *J. Non-Cryst. Solids* **2002,** 305, (1-3), 40-49.

28. Steeman, P. A. M.; Vanturnhout, J. *Macromolecules* **1994,** 27, (19), 5421-5427.

29. Kremer, F.; Schönhals, A.; Eds., *Broadband Dielectric Spectroscopy*. Springer-Verlag: Heidelberg 2003.

30. Wang, W.; Chan, T. T.; Perkowski, A. J.; Schlick, S.; Winey, K. I. *Polymer* **2009,** 50, (5), 1281-1287.

31. Benetatos, N. M.; Chan, C. D.; Winey, K. I. *Macromolecules* **2007,** 40, (4), 1081-1088.

32. Eisenberg, A.; Hird, B.; Moore, R. B. *Macromolecules* **1990,** 23, (18), 4098-4107.

Chapter 4

Multi-Length Scale Morphology of Poly(ethylene oxide)-Based Sulfonate Ionomers with Alkali Cations at Room Temperature

4.1 Introduction

Ion-conducting polymers have been the subject of intensive research for potential applications in energy storage and conversion devices, such as rechargeable lithium ion batteries and fuel cells.[1-5] The conductivity of the material is determined by both the ion mobility and the total number of mobile charge carriers, which in turn depend on the primary chemical structures and the secondary structures, namely the morphologies. In order to understand the ion conduction mechanism, a comprehensive understanding of the multiscale structure is essential.

The most widely studied systems for lithium batteries are based on poly(ethylene oxide) (PEO), which can effectively solvate a variety of alkali and alkaline cations.[6-8] Most of the earlier work has been focused on mixtures of PEO with salts. FTIR and Raman studies have assigned various vibration bands of anionic groups, such as triflates and sulfonates, to free anion, cation-anion pairs, and aggregated structures.[9-11] In addition, the complexation of ether oxygens with cations results in conformational changes of the PEO polymer backbone, which yields indirect information about the cation environment.[11-13] X-ray diffraction studies have been focused mainly on crystalline PEO-salt complexes. Cations are found to be incorporated into the crystalline complex and form various crystalline structures with PEO chains.[14-16] It was recently

demonstrated that polymer electrolytes of certain ordered crystalline structures can exhibit higher conductivity than disordered amorphous structures.[17] Although polymer/salt mixtures are able to provide reasonable conductivity, they suffer from undesirable concentration polarization, in which anions build up at the electrode/electrolyte interface due to their high mobility in the electrolyte and exclusion from the electrode.[18] The concentration polarization degrades battery performance.

Recently, there has been increasing interest in the study of single-ion conductors with anions fixed to the polymer backbone, because they can achieve a cation transference number of 1 and solve the concentration polarization problem.[18] However, most single-ion conductors show much lower conductivity than the polymer/salt mixtures. Dielectric spectroscopy studies on PEO-based sulfonated polyester and polyurethane ionomers indicate these materials have extremely low concentrations of conducting ions, and the conductivity exhibit a strong dependence on the glass transition temperature of ionomers.[19-21] A recent FTIR study on PEO-based sulfonated polyester ionomers neutralized by sodium cation showed no detectable free SO_3^- ions,[22] consistent with the dielectric studies. However, an overall picture of the morphology of these ionomers is still not available, and might hold the key to developing strategies to improve ion conductivity.

In this study, we analyze X-ray scattering data to determine the multiscale structure and ion association states of PEO-based sulfonated polyester ionomers with the structure shown in Scheme 4.1. A series of sulfonated polyester ionomers with well-defined PEO spacer lengths are investigated as a function of PEO segment length and

alkali cation type. Here we focus on the room-temperature multiscale morphology of these ionomers.

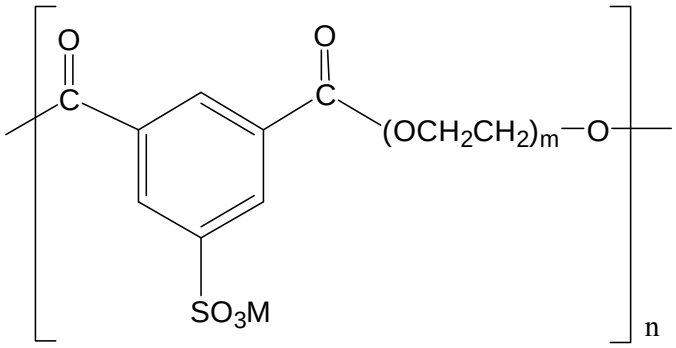

Scheme 4.1 PEO-based sulfonated polyester ionomers with well-defined PEO spacer (M_n = 400, 600, 1100, 3300 g/mol, and m = 9, 13, 25, 75). M represents the cation (M = Li, Na, or Cs) associated with the sulfonate group.

4.2 Experimental Section

4.2.1 Materials: The materials are provided by Professor Ralph Colby's group at the Pennsylvania State University. Poly(ethylene oxide) (PEO) based ionomers were prepared by a two-step catalyzed melt transesterification of poly(ethylene glycol) (PEG) oligomer diols of different molecular weights with dimethyl 5-sulfoisophthalate sodium salt to give ionomers of varying ion contents. The detailed synthesis procedures have been described in the previous publication.[23] ^{1}H nuclear magnetic resonance (NMR) is employed to verify the chemical structure and determine the number-average molecular weight (M_n) of the ionomers, Table 4.1. The molecular weights of PEO spacers are 400, 600, 1100, or 3300 g/mol, which were also determined by ^{1}H NMR. The cation was exchanged from sodium to lithium or cesium by aqueous diafiltration with an excess of LiCl or CsCl salts.[23] The concentrated ionomer solutions were then freeze-dried and

vacuum-dried at 120 °C to constant mass. The ionomers are denoted as PEO*x*-*y*M, where *x* is the molecular weight of PEO spacers in g/mol, *y* is the percent of sulfonated phthalates over the total amount of phthalates in the ionomer, and M represents the cation (M = Li, Na or Cs). For example, PEO600-100%Na designates the ionomer with PEO spacer length of 600 g/mol and 100% sulfonated phthalates neutralized with Na. Note that all the ionomers studied in this paper are 100% sulfonated and fully neutralized with alkali metal cations; thus, *y* is always 100%.

In addition to these ionomers, we also investigated the X-ray scattering of PEO600-0% and poly(ethylene glycol) oligomers (PEG9900 and PEG2800). PEO600-0% is a neutral polymer that contains only non-charged phthalates between PEO spacers, and was synthesized by reacting PEG diols with dimethyl isophthalate.[23] PEG9900 (M_n=9900 g/mol) and PEG2800 (M_n=2800 g/mol) were supplied by Sigma-Aldrich and TCI America, Inc, respectively. The molecular weights of these PEG oligomers were determined by ^{1}H NMR.

4.2.2 Thermal Analysis: The glass transition temperatures (T_g) of the ionomers were determined by differential scanning calorimetry (DSC) during the second heating cycle from -90 °C to 200 °C. Both heating and cooling rates are 10 °C/min. The melting temperatures (T_m) and percent crystallinities for semicrystalline ionomers (PEO1100-100%M and PEO3300-100%Na) and PEG oligomers are determined from the first heating cycle at a heating rate of 10 °C/min for the purpose of maintaining similar thermal history as the samples used in X-ray scattering.

4.2.3 X-ray Scattering: Because of the hygroscopic nature and low T_g of these ionomers, the samples were handled very carefully to minimize the exposure of samples

to moisture. The previously dried PEO-based ionomers were loaded into sandwich cells with mica windows, and further dried under vacuum at 70-80 ^{o}C for at least 2 days. The samples in the sandwich cell were gradually cooled down to room temperature under vacuum. The sandwich cell was then tightened and stored in a vacuum desiccator before being transferred to the X-ray vacuum chamber for data collection. It should be noted that PEO1100-100%M crystallizes very slowly at room temperature (~20 ^{o}C) compared to PEO3300-100%Na and PEG oligomers (PEG2800 and PEG9900) due to the presence of ions and the shorter PEO segment length. In order to study the crystalline structures of PEO1100-100%M, the dried materials were stored in a vacuum desiccator at room temperature for at least one week before data collection. As a comparison, PEG oligomers with M_n = 2800, and 9900 g/mol were also characterized by X-ray scattering. PEG oligomers were annealed in the vacuum oven at 70-80 ^{o}C for 24 hours, and then slowly cooled down to room temperature under vacuum.

The multi-angle X-ray scattering system (MAXS) used Cu Kα X-ray from a Nonius FR 591 rotating-anode generator operated at 40 kV and 85 mA. The bright, highly collimated beam was obtained via Osmic Max-Flux optics and triple pinhole collimation under vacuum. The scattering data were collected using a Bruker Hi-Star multiwire detector with sample to detector distances of 7, 11, 54, and 150 cm. The 2-D data reduction and analysis were performed using the Datasqueeze software.[24] Background scattering from an empty sandwich cell with mica windows are subtracted from the scattering data of samples. The normalized X-ray scattering data from PEO600-0% and PEO600-100%M were obtained by normalizing the scattering intensity by sample thickness, data collection time and percent of transmission.

4.2.4 *Ab Initio* Calculations: The *ab initio* calculations were performed by Wenjuan Liu in Professor Ralph Colby's group at the Pennsylvania State University. All the calculations reported in this paper were carried out with the Gaussian03 program[25] with the anion on the polymer modeled by benzenesulfonate. Calculations for Li^+, Na^+, and K^+ used the B3LYP/6-31+G* basis set, which considers all electrons in its optimization of configurations. Cs^+ has many electrons, so the B3LYP/LANL2DZ basis set was used for all calculations involving Cs^+. Both methods use density functional theory with Becke's three-parameter hybrid method and the LYP correlation functional (B3LYP) as the exchange - correlation functional.[26-29] Configurations were optimized and calculations were made at 0 K in vacuum for ion pairs and quadrupoles. Limited calculations were also performed using the polarizable continuum model (PCM) developed by Tomasi,[30-33] which is a simple extension of the Onsager model[34] to non-spherical cavities, which contain the ions, ion pairs and quadrupoles. The PCM calculations indicate that the 0K/vacuum calculations underestimate the actual ion spacings of isolated ion contact pairs and quadrupoles by about 10% at 300 K. The spacings between electron-rich atoms in these structures are useful for our interpretation of X-ray scattering in the 13 $nm^{-1} < q < 20$ nm^{-1} range for the amorphous ionomers.

4.3 Results and Discussion

Table 4.1 presents number-average molecular weight (M_n), glass transition temperature (T_g) and melting temperature (T_m) of ten PEO-based ionomers, one neutral counterpart (PEO600-0% from condensing PEG600 oligomer with non-sulfonated phthalates), and two PEG oligomers studied in this paper. The T_g values of all the

ionomers in Table 4.1 are below room temperature and increase with increasing ion content (decreasing PEO-spacer length). Since these ionomers have very low T_g and relatively low molecular weight, they are able to reach thermodynamic equilibrium rapidly. Previous rheological studies have shown that the terminal relaxation time of these materials is on the scale of 1 second or less at 30 ^{o}C.[23]

Table 4.1 Number average molecular weights (M_n) determined by ^{1}H NMR, and glass transition temperature (T_g), melting temperature (T_m), and percent crystallinity determined by DSC for PEO-based ionomers and PEG oligomers.

Notation	M_n, polymers (g/mol)	M_n, PEO Spacer (g/mol)	T_g (^{o}C) (DSC)	T_m (^{o}C) (DSC)	Percent crystallinity
PEO400-100%Li	3300	400	12[b]	N/A	0%
PEO400-100%Na	3400	400	22[b]	N/A	0%
PEO400-100%Cs	4000	400	21[b]	N/A	0%
PEO600-0%	6000	600	-46[b]	N/A	0%
PEO600-100%Li	4500	600	-15[b]	N/A	0%
PEO600-100%Na	4600	600	-6[b]	N/A	0%
PEO600-100%Cs	5200	600	-3[b]	N/A	0%
PEO1100-100%Li[a]	4500	1100	-36	32	8%
PEO1100-100%Na[a]	4500	1100	-31	33	4%
PEO1100-100%Cs[a]	4900	1100	-34	33	2%
PEO3300-100%Na	18,800	3300	N/A	47	48%
PEG2800	2800	N/A	N/A	58	91%
PEG9900	9900	N/A	N/A	63	84%

[a] In reference 23, these materials are labeled PE900-M (M = Li, Na, or Cs), but more recent analysis has determined that the PEO spacer length is 1100 g/mol. [b] Values from reference 23.

The percent crystallinity is estimated by comparing the measured heat of melting (ΔH_m) with that of 100% crystalline PEO with molecular weight of 4000 g/mol (215.6 J/g)[35]. The ionomers are amorphous when the PEO spacer length is 400 or 600 g/mol.

As the PEO segment length increases to 1100 or 3300 g/mol, polymer chains partially crystallize. The percent crystallinity of PEO3300-100%Na is about 48%, and the percent crystallinities of PEO1100-100%M with different cations are all less than 10%. The presence of ionic groups in the polymer backbone greatly reduces the crystallinity and slows the crystallization kinetics of the PEO spacer. The PEO1100-100%M did not show any crystallization or melting transitions during the second heating cycle (10 ^{o}C / min) due to their slow crystallization rate.

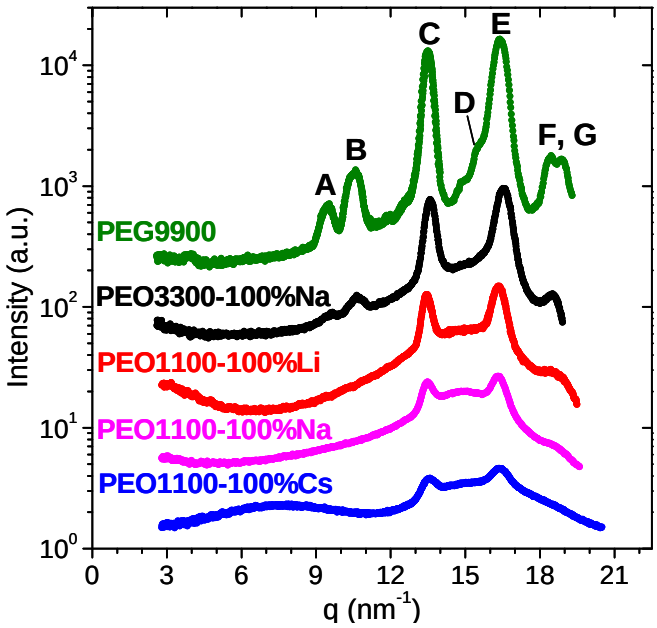

Figure 4.1 Comparison of crystal reflection peaks from semicrystalline PEO-based ionomers and the PEG9900 oligomer at room temperature. The X-ray scattering peaks labeled by letters correspond to crystalline PEO reflections; see details in Table 4.2.

The crystalline peaks from the four semicrystalline PEO-based ionomers are compared to the PEG oligomer with M_n = 9900 g/mol in Figure 4.1. All the scattering data presented in this paper are collected at room temperature. The crystalline reflections at 13.6, 16.5, and 18.5 nm^{-1} (labeled C, E, and F in Figure 4.1 and Table 4.2) correspond

well to the main reflections of typical PEO crystals having a helical chain conformation and a monoclinic lattice.[36] Each unit cell consists of four helical molecules along the *c*-axis.[29] The helices adopt 7/2 conformations,[36] in which 7 monomer units are required to complete two revolutions along the helix. The monoclinic unit cell is defined by the following parameters: a = 0.805 nm, b = 1.304 nm, c = 1.948 nm, and $\beta = 125.4^{o}$.[36, 37] The crystallinity of ionomers decreases with decreasing PEO segment length and increasing cation size, as shown in the relative intensity of the crystal peaks.

Table 4.2 Observed crystalline peaks in PEG oligomers and PEO-based ionomers in Figure 4.1 and the corresponding PEO crystal reflections [a]

Peak	*d*-spacing[b] (nm)	Reflections[36] (h k l)	PEG 2800, 9900	PEO1100-100%Li, Na, Cs	PEO3300-100%Na
A	0.59	020, $0\bar{2}0$	yes	no	yes
B	0.65	110, $\bar{1}\bar{1}0$, $\bar{1}10$, $1\bar{1}0$	yes	no	yes
C	0.46	120, $\bar{1}\bar{2}0$, $\bar{1}20$, $1\bar{2}0$	yes	yes	yes
D	0.40	004, $00\bar{4}$	yes	no	no
E	0.38-0.39	032, $0\bar{3}2$, 112, $1\bar{1}2$ $\bar{1}32$, $\bar{1}\bar{3}2$, $\bar{2}12$, $\bar{2}\bar{1}2$ $\bar{2}04$	yes	yes	yes
F, G	0.33-0.34	024, $0\bar{2}4$, $\bar{2}24$, $\bar{2}\bar{2}4$	yes	yes	yes

[a] "Yes" indicates the peak is observed, and "no" indicates the peak is not observed. [b] The *d*-spacing values are calculated by $2\pi/q^*$, where q^* is the position of peak A-G.

The *d*-spacings and corresponding crystalline reflections from both PEO-based ionomers and PEG oligomers are listed in Table 4.2. Some of the weaker crystal reflections are missing in the ionomer data due to their low crystallinity. The observed reflections in semicrystalline ionomers neutralized with three different cations (Li, Na, and Cs) and PEG oligomers are identical, indicating PEO spacers all crystallize into the

monoclinic lattice structure of pure PEO. Because the lattice parameters remain unchanged in PEO-based ionomers, we conclude that the ions are excluded from the crystal and reside in the amorphous phase.

Figure 4.2 shows the room temperature X-ray scattering data from PEO*x*-100%M ionomers over a wide range of scattering angles. PEO400-100%M and PEO600-100%M are fully amorphous. These ionomers exhibit a strong peak at $q \approx 15$ nm^{-1} corresponding to the amorphous halo of PEO. In semicrystalline ionomers (PEO1100-100%M and PEO3300-100%Na), the crystallinity is coupled with multiple small-angle peaks. Two different origins have been identified, as shown in Figure 4.2. The peak designated by "L" is assigned to the lamellar scattering, as observed in typical semicrystalline polymers and schematically drawn in Figure 4.3. The broad peak corresponding to the lamellar spacing in semicrystalline PEO3300-100%Na is obscured by the crystallite thickness peak (1) and the strong upturn at lower angles. The additional three peaks show a positional ratio of 1:2:3, as labeled in Figure 4.2, indicating a layered structure. The spacing of these layered structures (t_{expt}) is obtained from the periodic peak positions ($t_{\text{expt}} = \langle 2\pi / q_i \rangle$) and listed in Table 4.3. As a comparison, the lengths of 7/2 helices of the PEO spacers (t_{helix}) are calculated based on the monoclinic lattice parameters and reported in Table 4.3.

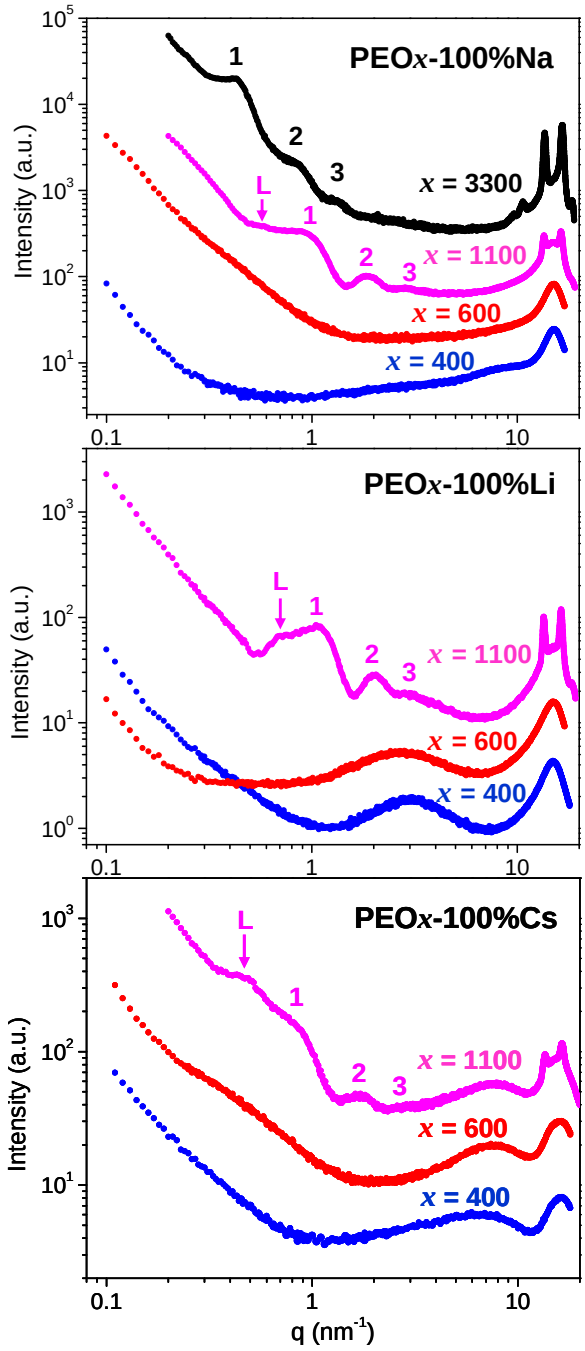

Figure 4.2 X-ray scattering intensity as a function of scattering vector q from PEOx-100%M ionomers with different PEO spacer lengths (x) and cations (M) at room temperature. The scattering peaks labeled L and numbers (1,2,3) correspond to the lamellar spacing (L) and the crystallite thickness (t_{expt}), respectively; see Table 4.3.

Table 4.3 PEO crystallite thickness (t) and lamellar spacing (L) from calculation and X-ray scattering experiment.

	m (PEO)[a]	t_{helix} (nm)	t_{expt} (nm)	L_{expt} (nm)	PEO Chain
PEO1100-100%Li	25	7.0	6.2	9.0	Extended
PEO1100-100%Na	25	7.0	6.8	11.2	Extended
PEO1100-100%Cs	25	7.0	7.2	14.3	Extended
PEO3300-100%Na	75	20.8	15.3	--	Extended
PEG2800	64	17.8	19.3	--	Extended
PEG9900	224	62.3	23.8	--	Folded

[a] m denotes the degree of polymerization of the PEO spacer.

Based on the consistency of t_{helix} with t_{expt} in Table 4.3, the higher order peaks (labeled 1, 2, 3 in Figure 4.2) are assigned to the scattering between the two amorphous-crystalline interfaces of each PEO crystallite and correspond to the crystallite thickness (t). This multiscale structure in semicrystalline ionomers is shown schematically in Figure 4.3. Note that the crystallite thickness increases with cation size (Li, Na, and Cs). It is expected that the ionic groups at the crystalline-amorphous interfaces also contributed to the scattering, and thus the crystallite thickness obtained from X-ray scattering also includes the size of the ions. It is expected that the long PEO spacer might not be fully crystallized in PEO3300-100%Na, resulting in shorter periodicity in X-ray scattering ($t_{expt} < t_{helix}$). Connor *et al.* found by dynamic measurement that the crystallinity of PEG oligomers reached a maximum at M_n around 1000 g/mol.[38] This is because the number of lattice defects tends to increase with molecular weight while the packing problem of chain ends dominates in polymers of low molecular weight.

Typical semicrystalline polymers usually show only the L peak due to the polydispersity in crystallite thickness and limited contrast between the amorphous and

crystalline domains. The appearance of multiple peaks in PEO-based ionomers is caused by well-defined crystallite thicknesses and the increased electron density difference provided by the cations. Typically, the thickness of polymer crystallites (t) is predominantly controlled by the crystallization temperature and time. In contrast, for PEO1100-100%M ionomers, the segment length is short enough that each segment of PEO chain between phthalates is *fully extended* in the crystallites. The experimental crystallite thickness t_{expt} is less than 12% different from the calculated value t_{helix}. Thus, the thickness of PEO crystallites in these ionomers is controlled by the well-defined PEO segment length.

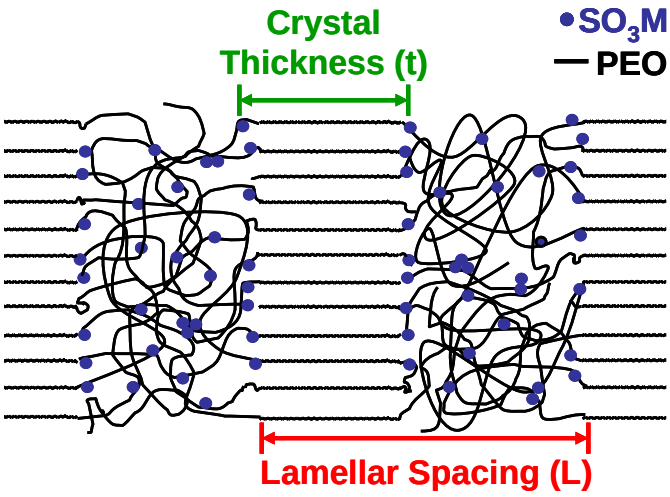

Figure 4.3 Schematic of the semicrystalline morphology of PEO-based ionomers showing crystalline lamellae-lamellae spacing (L) and well-defined crystallites of thickness (t).

On the other hand, the percent crystallinity of PEO1100-based ionomers is highly dependent on the thermal history and cation type. The lamellar spacing increases rather significantly with increasing cation size. The upper limit of the percent crystallinity in

PEO1100-100%M ionomers can be estimated by t_{expt}/L_{expt}, which is 69%, 61%, 50% for ionomers neutralized with Li, Na, and Cs, respectively. Because of the presence of ionic groups, the actual percentages of crystallinity of these ionomers are all less than 10% and decrease with increasing cation size, Table 4.1. Moreover, the ionomers crystallize very slowly over several days at room temperature under vacuum. Increasing the cation size reduces both the crystallization rate and the percent crystallinity of the ionomer, because the larger cation generally requires more ether oxygen coordination in both amorphous state and PEO-salt crystalline complex.[39, 40]

To further understand the multiscale crystalline structure in semicrystalline PEO-based ionomers, PEG oligomers with different molecular weights (2800 g/mol and 9900 g/mol) were also studied by X-ray scattering, Figure 4.4. Both PEG oligomers show multiple peaks with positional ratios of 1:2:3… in this angular regime. These PEG oligomers show high percentages of crystallinity by DSC: 91% for PEG2800 and 84% for PEG9900. Thus, t_{expt} is comparable to L_{expt}, and, as a result, the lamellar-lamellar scattering peaks in the PEG oligomers are probably obscured by the crystallite thickness peaks due to their proximity in position. The size of the crystallites in PEG2800 obtained from X-ray scattering (t_{expt}) corresponds well with the calculated value based on the PEG2800 molecular weight (t_{helix}), Table 4.3. The oligomer chain of PEG2800 is fully extended when it crystallizes. In contrast, the longer oligomer PEG9900 forms folded structures, since $t_{helix} \approx 3\,t_{expt}$. The observed behavior (extended or folded chain) in these two PEG oligomers is consistent with previous findings.[41, 42] In particular, Sánchez-Soto *et al*. observed the melting temperature of PEO reached the plateau at the critical

molecular weight of 4000 g/mol, which was interpreted as transition from extended chain to folded chain in PEO crystallites.[42]

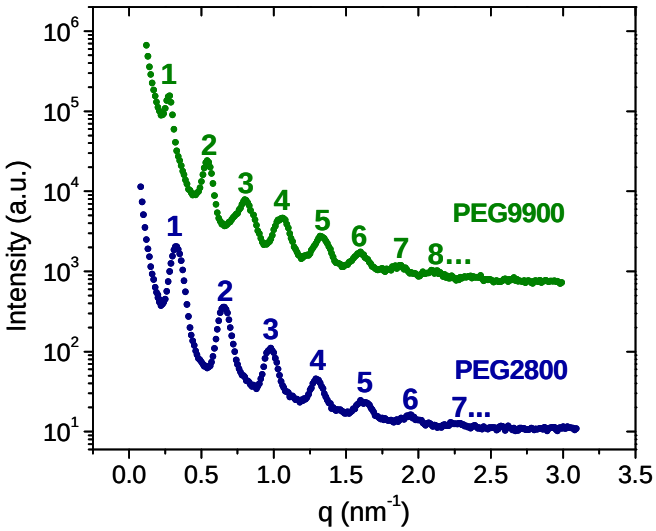

Figure 4.4 X-ray scattering intensity as a function of scattering vector q plotted in log-linear scale for PEG oligomers with different molecular weights at room temperature. The numbers correspond to higher order scattering from the crystallite thickness (t_{expt}), Table 4.3.

The states of ions in PEO-based ionomers neutralized with different cations are quite different from conventional ionomers. Previous X-ray scattering data from a variety of model ionomers show an ionomer peak at q = 1-5 nm^{-1}.[43] Examples include Na- and Zn-neutralized poly(ethylene-*ran*-methacrylic acid) ionomers,[44, 45] sulfonated polystyrene ionomers neutralized with Cu, Mg, Zn, Na, Ba, and Cs,[46, 47] or Li-, Cs-, and Cu-neutralized poly(styrene-*ran*-methacrylic acid) ionomers.[48, 49] PEO600-100%Li shows an ionomer peak at $q \approx 2.7$ nm^{-1} (Figure 4.2), indicating microphase separated structures with ~2.3 nm spacing. The peak shifts to higher q value (smaller inter-particle spacing) as the PEO segment length decreases from 600 to 400 g/mol, meaning that the

number density of ionic aggregates increases with ion content. PEO1100-100%Li also showed an ionomer peak, which overlaps with higher-order scattering peaks from crystal thickness and has been observed in thermally quenched PEO1100-100%Li when the ionomer was amorphous. The presence of a well-defined correlation scattering peak, as opposed to an asymmetric shoulder, upturn, or tail, suggests that the ionic aggregates are homogeneously distributed in the matrix and are of sufficiently high number density to generate inter-particle scattering.

In contrast, the Na- and Cs-neutralized PEO-ionomers do not show any ionomer peak in Figure 4.2. The Cs-neutralized PEO-ionomers show a broad peak around 6-8 nm^{-1}. Based on the peak position and total ion concentration in these ionomers, the peak is attributed to the scattering from mostly isolated ion pairs. (Additional evidence will be presented later when we discuss Figure 4.5b.) Contrary to the Li-ionomers, the peak shifts to lower q value (larger inter-particle spacing) and broadens as the PEO segment is shortened, which is probably caused by the increasing fraction of Cs ions forming aggregates at higher ion content. As the ion pairs aggregated due to decreasing ethylene oxide (EO) /Cs ratio, the average correlation distance between scatters increased. Our results are consistent with previous spectroscopic study of PEO-based sulfonate ionomers, which found that the band due to aggregated sulfonate increased in intensity with increasing ion concentration.[22] Even though the PEO*x*-100%Na and PEO*x*-100%Cs ionomers do not exhibit an ionomer peak, these materials could still contain a small amount of randomly distributed ionic aggregates, as the subsequent analysis suggests.

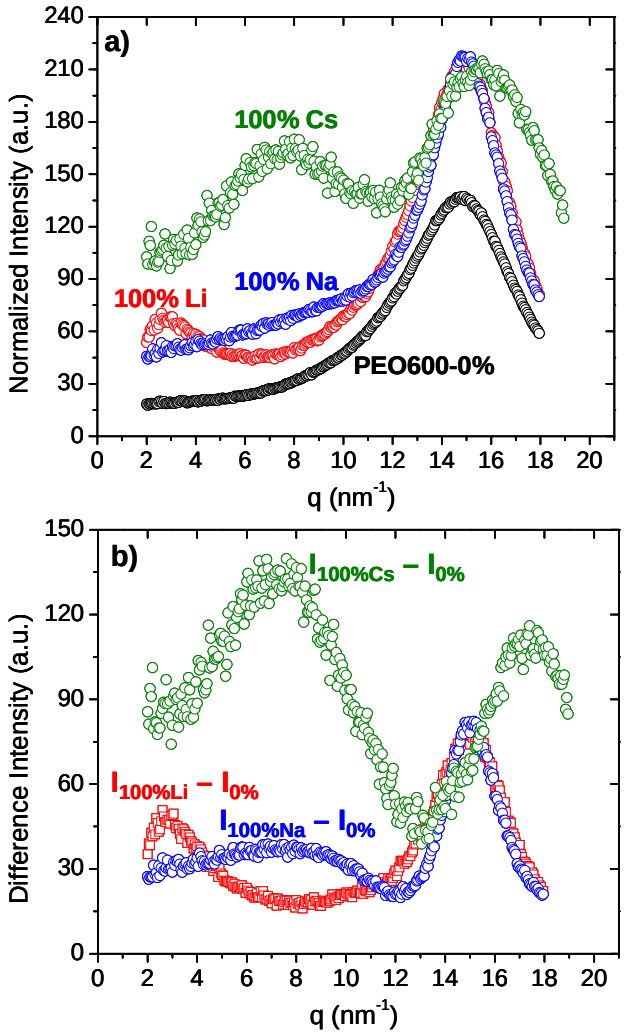

Figure 4.5 a) Wide-angle X-ray scattering intensity at room temperature from PEO600-100%M (M = Li, Na, Cs) and PEO600-0% normalized by sample thickness, collection time, and percent of transmission. b) Difference intensity of PEO600-100%M after subtracting scattering intensity of PEO600-0% from PEO600-100%M.

To obtain quantitative comparison between the scattering data from ionomers neutralized with three different cations, the wide-angle X-ray scattering intensities of PEO600-100%M are normalized by sample thickness, data collection time and percent of transmission, as shown in Figure 4.5a. PEO600-100%M ionomers showed stronger

amorphous peak intensity at 14-16 nm^{-1} compared to PEO600-0%, which is caused by the additional scattering from S, O, and metal cations. Figure 4.5b displays the difference scattering intensity of PEO600-100%M after subtracting the scattering from PEO600-0%, and shows apparent peaks at q = 2-12 nm^{-1} from PEO600-100%M. These peaks result from the interparticle scattering from closely assembled and strongly interacting ions in various associated states, such as isolated ion pairs, quadrupoles, or larger aggregates. Figure 4.6 shows equilibrated structures of an ion pair and a quadrupole generated by *ab initio* calculations of lithium benzenesulfonate.

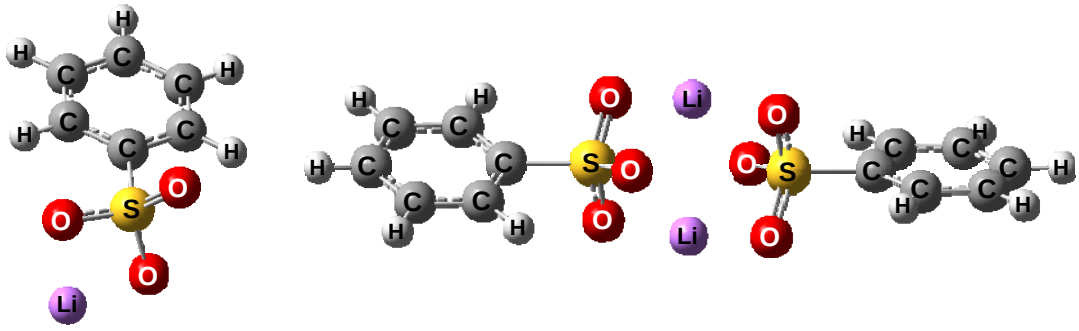

Ion Pair **Quadrupole**

Figure 4.6 Simulation results for an ion pair and a quadrupole equilibrated at 0 K in vacuum using *ab initio* calculations.

The sharp peak centered at 2.7 nm^{-1} in PEO600-100%Li is virtually unchanged from Figure 4.5a to Figure 4.5b and indicated the presence of ionic aggregates, as discussed above. The broad peak centered at ~7 nm^{-1} from subtracted PEO600-100%Cs in Figure 4.5b corresponds to a correlation distance of 0.9 nm. If all the ionic groups form isolated ion pairs, the distance between ion pairs estimated from the total concentration of cations (~0.75 nm^{-3})[19] is ~1.1 nm by assuming simple cubic packing. Since the ion pairs are randomly distributed in the matrix rather than in a lattice, we

expect the average distance between ion pairs to be slightly smaller than 1.1 nm. This estimate is comparable to the distance obtained from X-ray scattering, indicating the majority of the ions in PEO600-100%Cs exist in isolated ion pairs. However, due to the broadness of the difference peak, the presence of a small fraction of disordered ionic aggregates cannot be excluded.

The weak peak centered at 7 nm^{-1} from subtracted PEO600-100%Na is even broader than that from PEO600-100%Cs, suggesting a wider range of distributions of ionic states and correlation distances. The weakness of this peak corresponds to a smaller difference in electron density between SO_3Na and PEO. The asymmetry and broadness of the peak suggests that PEO600-100%Na contains both isolated ion pairs and some disordered ionic aggregates. Previous studies of PEO600-100%Na ionomers by FTIR have identified two different states of sulfonate groups, corresponding to a majority of isolated ion pairs (SO_3Na) and a considerable amount of aggregates (with higher frequency S-O stretching vibrations indicating $NaSO_3Na$).[22] Without subtracting the scattering from PEO600-0%, the peak for PEO600-100%Na is hidden underneath the broad amorphous peak due to its low intensity and proximity to the stronger amorphous peak. The intensity of this broad peak increases with ion content, as observed by comparing PEO600-100%Na and PEO400-100%Na at q = 6-11 nm^{-1} in Figure 4.2.

The peaks at 12-18 nm^{-1} in Figure 4.5b arise from interatomic scatterings of ionic groups in various states, because the contribution from amorphous PEO scattering has been subtracted. The peak at 15.0 nm^{-1} in PEO600-100%Li and Na corresponds to a correlation distance (*d*) of 0.42 nm, while PEO600-100%Cs shows *d* = 0.36 nm (q = 17.4 nm^{-1}). To facilitate interpretation, *ab initio* calculations at 0K in vacuum were made on

ion pairs and quadrupoles of benzenesulfonate with various alkali cations (M), with the results shown in Table 4.4. In ion pairs, only the sulfur-cation (S-M) distances are shown, since sulfur has higher electron density than oxygen. In quadrupoles, three interatomic spacings are considered: sulfur-cation (S-M), sulfur-sulfur (S-S), and cation-cation (M-M). As expected, the S-M spacing of the isolated ion pairs are consistently smaller than the S-M spacings in quadrupoles, since the latter has cation-cation and sulfonate-sulfonate repulsions in addition to sulfonate-cation attractions. Ion pairs and quadrupoles of sulfonated dimethyl phthalate have also been calculated for comparison. Adding ester groups to the benzene ring changes electronic states of the benzene ring only slightly, because the charged sulfonate group dominates the electronic states. Thus, the relatively subtle effects of the ester groups cause little change to interatomic distances. For example, the Li sulfonated dimethyl phthalate pair has 0.5% larger Li-S spacing and the Li sulfonated dimethyl phthalate quadrupoles have 1.2% larger S-S spacing. These changes are well within uncertainties.

Table 4.4 *Ab initio* calculations of interatomic spacings at 0 K in vacuum for benzenesulfonate with alkali cations (M = Li^+, Na^+, K^+ or Cs^+).

Cation	Effective Cation Radius (nm)[a]	Ion Pair	Quadrupole		
		S-M (nm)	S-M (nm)	S-S (nm)	M-M (nm)
Li^+	0.076	0.24	0.29 (2), 0.25 (2)	0.41	0.35
Na^+	0.102	0.27	0.29 (4)	0.46	0.33
K^+	0.138	0.31	0.33 (4)	0.51	0.41
Cs^+	0.167	0.33	0.38 (4)	0.59	0.47

[a] Effective ionic radii are based on a six-coordination oxygen environment.[50]

Interatomic distances at room temperature in the significantly more polar environment of our ionomers are expected to be ~10% larger than those in Table 4.4. To facilitate comparison with our X-ray scattering results at room temperature, we multiply the interatomic distances in Table 4.4 by 1.1 for the following discussion. The *d* value (0.42 nm) from X-ray scattering of PEO600-100%Li correlates best with the S-S spacing of the quadrupoles from *ab initio* calculations (0.41 nm × 1.1 = 0.45 nm), suggesting that S-S scattering in quadrupoles contributes the most to the peak at 15 nm^{-1} in PEO600-100Li. The higher q peak (with *d* = 0.36 nm) in PEO600-100%Cs is consistent with the S-Cs spacing (0.33 nm × 1.1 = 0.36 nm) in ion pairs. This is consistent with our interpretation above that ions in PEO600-100%Cs mainly form mostly ion pairs, while ions in PEO600-100%Li form aggregated structures, which by their nature could include quadrupoles. For PEO600-100%Na, the experimental *d* value (0.42 nm) lies between S-S spacing of the quadrupoles (0.46 nm × 1.1 = 0.51 nm) and M-M spacing of the quadrupoles (0.33 nm × 1.1 = 0.36 nm). Given that S and Na are close in electron density, the comparison with *ab initio* is inconclusive. More accurate prediction of the peak shape and intensity would require form factor and structure factor simulation, as well as the exploration of additional types of ionic assemblies.

Our results show that the size of the cation plays a critical role in the ionic states of PEO-based ionomers. This is different from conventional ionomers where the ionic aggregation behavior is relatively insensitive to the neutralizing cations.[45, 47] The dependence of ionic association on the cation size in PEO-based ionomers is attributed to the interactions between the ether oxygens from PEO and the cations. The association energy of cations with anions and cations with ether oxygens increases with decreasing

cation size to produce different coordination structures and local morphologies with different cation sizes. Our results from X-ray scattering are consistent with the previous findings by dielectric relaxation spectroscopy that showed the mobile ion concentration increased with increasing cation size in PEO-based ionomers.[21]

4.4 Conclusion

The multiscale morphologies of PEO-based sulfonated polyester ionomers have been investigated by X-ray scattering. The morphologies of ionomers are highly dependent on the PEO segment length and cation size. Increasing the PEO segment length results in the crystallization of PEO segments into monoclinic unit cells that are identical to PEG oligomers. Thus, the ionic groups (SO_3^- and M^+) are apparently excluded to the amorphous domains of these PEO-based ionomers, which is in contrast to traditional crystalline PEO/salt mixtures. The crystalline PEO segments form crystallites with well-defined thickness as exemplified by the higher order scattering peaks, where the crystallite thickness is defined by the PEO segment length. The presence of ionic groups reduces the percent of crystallinity and slows crystallization kinetics relative to PEO. Although PEO has been shown to have maximum crystallinity at M_n around 1000 g/mol,[38] our PEO1100-100%M ionomers crystallize over a period of several days at room temperature in dry conditions and only obtain crystallinity of ~10% or less.

These PEO-based ionomers exhibit a wider range of microphase segregation of ions from polymer backbones than is seen in conventional hydrocarbon-based ionomers,[43] because there is significant solvation interaction between the cations and ether oxygens. Our results showed the ionic states are highly dependent on the cation

type, due to the different association energies of cations with anion and ether oxygens. PEO-based ionomers containing Li cations form ionic aggregates, while the majority of ionic groups in Cs-neutralized ionomers exist as isolated ion pairs. PEO*x*-100%Na ionomers have a broader range of local ionic states, including both isolated ion pairs as well as aggregated states. The conductivity of ionomers is highly dependent on the association states of the ions. These PEO-based ionomers do not have high conductivity due to the low concentrations of conducting free ions,[23] because most of the ions form bound states. To improve the ionic conductivity, bulky ion with weaker binding energy or/and more polar functional groups that can effectively solvate the ions need to be introduced into the polymer structure. Our results provide important insights regarding the hierarchical structures of the ionomers for rational design of molecular structures to improve the ionic conductivity. Since the conductivity of ionomers is highly dependent on temperature, a thorough investigation of morphology as a function of temperature is underway and will be the subject of a future publication.

4.5 References

1. Takeoka, S.; Ohno, H.; Tsuchida, E. *Polym. Adv. Technol.* **1993,** 4, (2-3), 53-73.

2. Meyer, W. H. *Adv. Mater.* **1998,** 10, (6), 439-448.

3. Armand, M.; Tarascon, J. M. *Nature* **2008,** 451, (7179), 652-657.

4. Hickner, M. A.; Ghassemi, H.; Kim, Y. S.; Einsla, B. R.; McGrath, J. E. *Chem. Rev.* **2004,** 104, (10), 4587-4611.

5. Smitha, B.; Sridhar, S.; Khan, A. A. *J. Membr. Sci.* **2005,** 259, (1-2), 10-26.

6. Wright, P. V. *British Polymer Journal* **1975,** 7, (5), 319-327.

7. Xu, K. *Chem. Rev.* **2004,** 104, (10), 4303-4417.

8. Armand, M. B.; Chabagno, J. M.; Duclot, N. J., In *Fast Ion Transport in Solids*, Vashishta, P.; Mundy, J. N.; Shenoy, G. K., Eds. North Holland, New York 1979; p 131.

9. Kakihana, M.; Schantz, S.; Torell, L. M.; Stevens, J. R. *Solid State Ionics* **1990,** 40-1, 641-644.

10. Huang, W. W.; Frech, R.; Wheeler, R. A. *J. Phys. Chem.* **1994,** 98, (1), 100-110.

11. Rhodes, C. P.; Khan, M.; Frech, R. *J. Phys. Chem. B* **2002,** 106, (40), 10330-10337.

12. Frech, R.; Huang, W. W. *Macromolecules* **1995,** 28, (4), 1246-1251.

13. Frech, R.; Rhodes, C. P.; Khan, M. *Macromol. Symp.* **2002,** 186, 41-49.

14. Lightfoot, P.; Nowinski, J. L.; Bruce, P. G. *J. Am. Chem. Soc.* **1994,** 116, (16), 7469-7470.

15. Lightfoot, P.; Mehta, M. A.; Bruce, P. G. *Science* **1993,** 262, (5135), 883-885.

16. Andreev, Y. G.; Bruce, P. G. *Electrochimica Acta* **2000,** 45, (8-9), 1417-1423.

17. Gadjourova, Z.; Andreev, Y. G.; Tunstall, D. P.; Bruce, P. G. *Nature* **2001,** 412, (6846), 520-523.

18. Wright, P. V. *MRS Bull.* **2002,** 27, (8), 597-602.

19. Fragiadakis, D.; Dou, S.; Colby, R. H.; Runt, J. *J. Chem. Phys.* **2009,** 130, (6), 064907.

20. Fragiadakis, D.; Dou, S. C.; Colby, R. H.; Runt, J. *Macromolecules* **2008,** 41, (15), 5723-5728.

21. Klein, R. J.; Zhang, S. H.; Dou, S.; Jones, B. H.; Colby, R. H.; Runt, J. *J. Chem. Phys.* **2006,** 124, (14), 144903.

22. Lu, M.; Runt, J.; Painter, P. *Macromolecules* **2009,** 42, (17), 6581-6587.

23. Dou, S. C.; Zhang, S. H.; Klein, R. J.; Runt, J.; Colby, R. H. *Chem. Mater.* **2006,** 18, (18), 4288-4295.

24. Heiney, P. A. *Commission on Powder Diffraction Newsletter* **2005,** 32, 9-11.

25. M. J. Frisch*, et al. GAUSSIAN 03*, Revision B.05; Gaussian Inc.: Pittsburgh, PA, 2003.

26. Becke, A. D. *J. Chem. Phys.* **1993,** 98, (2), 1372-1377.

27. Becke, A. D. *Phys. Rev. A* **1988,** 38, (6), 3098-3100.

28. Lee, C. T.; Yang, W. T.; Parr, R. G. *Phys. Rev. B* **1988,** 37, (2), 785-789.

29. Stephens, P. J.; Devlin, F. J.; Chabalowski, C. F.; Frisch, M. J. *J. Phys. Chem.* **1994,** 98, (45), 11623-11627.

30. Mennucci, B.; Tomasi, J. *J. Chem. Phys.* **1997,** 106, (12), 5151-5158.

31. Cances, E.; Mennucci, B.; Tomasi, J. *J. Chem. Phys.* **1997,** 107, (8), 3032-3041.

32. Cossi, M.; Barone, V.; Mennucci, B.; Tomasi, J. *Chem. Phys. Lett.* **1998,** 286, (3-4), 253-260.

33. Cossi, M.; Scalmani, G.; Rega, N.; Barone, V. *J. Chem. Phys.* **2002,** 117, (1), 43-54.

34. Onsager, L. *J. Am. Chem. Soc.* **1936,** 58, 1486.

35. Beaumont, R. H.; Clegg, B.; Gee, G.; Herbert, J. B. M.; Marks, D. J.; Roberts, R. C.; Sims, D. *Polymer* **1966,** 7, (8), 401-417.

36. Zhu, L.; Cheng, S. Z. D.; Calhoun, B. H.; Ge, Q.; Quirk, R. P.; Thomas, E. L.; Hsiao, B. S.; Yeh, F. J.; Lotz, B. *J. Am. Chem. Soc.* **2000,** 122, (25), 5957-5967.

37. Takahash.Y; Tadokoro, H. *Macromolecules* **1973,** 6, (5), 672-675.

38. Connor, T. M.; Williams, G.; Read, B. E. *J. Appl. Chem. USSR* **1964,** 14, (2), 74.

39. Besner, S.; Prudhomme, J. *Macromolecules* **1989,** 22, (7), 3029-3037.

40. Thomson, J. B.; Lightfoot, P.; Bruce, P. G. *Solid State Ionics* **1996,** 85, (1-4), 203-208.

41. Godovsky, Y. K.; Slonimsky, G. L.; Garbar, N. M. *J. Polym. Sci. Part C: Polym. Symp.* **1972,** 38, 1-12.

42. Sanchez-Soto, P. J.; Gines, J. M.; Arias, M. J.; Novak, C.; Ruiz-Conde, A. *J. Therm. Anal. Calorim.* **2002,** 67, (1), 189-197.

43. Eisenberg, A.; Kim, J.-S., *Introduction to Ionomers*. John Wiley & Sons: New York, 1998.

44. Marx, C. L.; Caulfield, D. F.; Cooper, S. L. *Macromolecules* **1973,** 6, (3), 344-353.

45. Yarusso, D. J.; Cooper, S. L. *Polymer* **1985,** 26, (3), 371-378.

46. Yarusso, D. J.; Cooper, S. L. *Macromolecules* **1983,** 16, (12), 1871-1880.

47. Zhou, N. C.; Chan, C. D.; Winey, K. I. *Macromolecules* **2008,** 41, (16), 6134-6140.

48. Eisenber.A; Navratil, M. *Macromolecules* **1974,** 7, (1), 90-94.

49. Wang, W.; Chan, T. T.; Perkowski, A. J.; Schlick, S.; Winey, K. I. *Polymer* **2009,** 50, (5), 1281-1287.

50. Shannon, R. D. *Acta Crystallographica Section A* **1976,** 32, (Sep1), 751-767.

Chapter 5

Thermally Reversible Formation of Ionic Aggregates in Poly(Ethylene Oxide)-Based Sulfonate Ionomers

5.1 Introduction

Ionomers are an interesting class of ion-containing polymers with a small fraction of ionic functional groups chemically attached to the polymer backbone.[1] Due to their exceptional physical and chemical properties, ionomers have found wide-ranging applications from chemical resistant coatings and adhesives to ion-transport membranes. The unique properties of ionomers arise from the self-assembly of ionic groups into various associated structures that act as physical crosslinks. Significant research efforts have been devoted to understanding ionomer morphologies with state-of-the-art spectroscopy, scattering, and microscopy techniques.[2-7] In particular, X-ray scattering is a powerful tool to probe the nanoscale morphology of ionomers.[7] The formation of ionic aggregates is manifested by the appearance of a broad, isotropic scattering peak typically in the angular region between 1 - 5 nm^{-1}. The ionomer peak has been observed in a variety of ionomers.[1, 7] While several models have been proposed to interpret the ionomer peak, it is widely accepted that the peak arises from the interparticle scattering between the ionic aggregates.[2, 8-11]

Variable-temperature X-ray scattering studies on ionomers neutralized with metal cations have shown that the ionomer peak persists to at least 200 ^{o}C, suggesting strong ionic aggegation.[4, 12-15] Williams *et al.* observed that the ionomer peak in Mg-neutralized

carboxy-telechelic polybutadiene ionomers broadened and shifted to lower angle as the temperature was raised above the glass transition temperature.[15] Nevertheless, the ionomer peak was still observed at the highest temperature studied (209 ^{o}C).[15] The authors argued that these changes would be thermally reversible if their polymer had not degradated.[15] The association strength dramatically decreases when the cation is changed to bulky organic ions, such as alkylammonium.[16] Page *et al.* found that the ionomer peak in Nafion neutralized with alkylammonium exhibited an abrupt decrease in intensity with increasing temperature, which is attributed to the transition from a static, physically cross-linked system to a dynamic network.[16] The transition temperature decreases from 260 to 80 ^{o}C as the counterion size increases.[16] The evolution of scattering patterns with temperature, i.e. the ionomer peak intensity, shape, and position, not only varies between ionomer types but is also affected by sample preparation conditions and thermal histories.[7, 12-14, 17] In particular, Weiss *et al.* observed that an ionomer peak developed at ~165 ^{o}C and increased in intensity with increasing temperature in a Mn-neutralized SPS ionomer with 7.6 mol% sulfonation (Mn-$SPS_{0.076}$).[17] The formation of this ionomer peak in Mn-SPS was **not** thermally reversible.[17] It should be noted that this ionomer was solution cast from a highly polar solvent (a 90/10 by volume% mixture of THF and water) and was not thermally annealed above the glass transition temperature (T_g) before the scattering experiment was performed.[17] Register *et al.* investigated the effect of thermal treatment on the same ionomer and found that the ionomer peak developed after annealing at 120 ^{o}C for 4 days or compression-molding at 188 ^{o}C.[18] Thus, the absence of an ionomer peak in Mn-$SPS_{0.076}$ before annealing or at the beginning of the initial heating

cycle during the X-ray scattering reflects a kinetically trapped non-equilibrium state caused by the solvation of the ionic groups by polar solvent in solution.

The presence of various associated states of ionic groups, such as quadrupoles or larger aggregates, greatly increases the viscosities and relaxation times of ionomers.[19] The viscoelastic behavior of ionomers typically exhibit multiple relaxation processes, including segmental motion of polymer matrix, the ion-hopping process, and terminal relaxation. Although the ionomer peak persists at high temperatures, ions in the aggregates can diffuse through an ion-hopping process.[19, 20] Many researchers have reported that the time-temperature superposition (TTS) of viscoelastic data breaks down in ionomers, which is attributed to the presence of a secondary relaxation mechanism.[21-23] Tierney and Register reported that the ion-hopping and terminal relaxations have a similar temperature dependence in both sulfonated poly(styrene-ethylene-butene) (SBE) and poly(ethylene-methacrylic acid) ionomers, i.e. these two processes have a similar activation energy in the two materials.[20, 22] It is found that the failure of TTS in sulfonated SBE ionomers is caused by the difference between the activation energy for the above two processes and that for the relaxation of chains of non-ionic end sections.[22] However, it should be noted that the ionomer dynamics are often complicated by non-ideal molecular architectures, e.g. polydispersity or branching, thus the successful implementation of TTS does not necessarily indicate the absence of ionic aggregation.[24]

Poly(ethylene oxide) (PEO)-based ionomers are single-ion conductors with anions fixed to the polymer backbone and are of great interest for potential applications in lithium ion batteries.[25] It is well-known that PEO is able to solvate a variety of alkali and alkaline cations through coordination of ether oxygens with each cation.[26-28] In addition,

the low glass transition temperature of PEO is advantageous for ion transport, as ion mobility in polymer electrolytes has been found to be strongly coupled with the segmental motion of polymer chain.[29, 30] Moreover, single-ion conductors can prevent the concentration polarization problem that is typically seen in bi-ion conductors, e.g. polymer/salt mixtures, in which anions build up at the electrode/electrolyte interface due to their high mobility in the electrolyte and exclusion from the electrode.[25] However, most single-ion conductors show much lower conductivity than polymer/salt mixtures. The ion conductivity is highly dependent on the association states of the ionic groups. Dielectric spectroscopy studies on PEO-based sulfonated polyester and polyurethane ionomers indicate the ions in these single-ion conductors mostly form bound states and do not contribute to ion conduction.[31-34] The temperature dependence of ion mobility in these ionomers follows the Vogel-Fulcher-Tammann equation, consistent with the coupling of ion motion to segmental mobility.[32-34] The conducting ion concentration increases with increasing temperature in an Arrhenius fashion,[32-34] suggesting a thermally activated process. Nevertheless, a detailed picture about the evolution of morphologies with temperature in these PEO-based ionomers is still not available, and could provide important insights for effective design of materials with improved ion conductivity.

In Chapter 4, we have reported the room-temperature morphology of PEO-based sulfonated polyester ionomer as a function of PEO segment length and alkali cation type (Li, Na and Cs).[35] The chemical structure of the ionomers is shown in Scheme 5.1. The scattering contribution of PEO and neutral phthalates was removed from the 100% sulfonated ionomers by subtracting the normalizing the X-ray scattering intensities, which enables the analysis of scattering from ions only.[35] The subtracted scattering

profiles from both the Cs- and Na-neutralized ionomers exhibit a broad peak centered at ~ 7 nm^{-1}, corresponding predominantly to the scattering from isolated ion pairs.[35] As the cation size decreases to Li, the states of ionic groups change from a majority of isolated ion pairs to aggregated structures, as shown by an ionomer peak at 2.7 nm^{-1}.[35] These results show that the states of ionic association in PEO-based ionomers at room temperature are highly dependent on the cation size. This paper presents ionic association behaviors in these ionomers at temperatures from 25 -150 ^{o}C and reports that the effect of cation size is diminished at 150 ^{o}C.

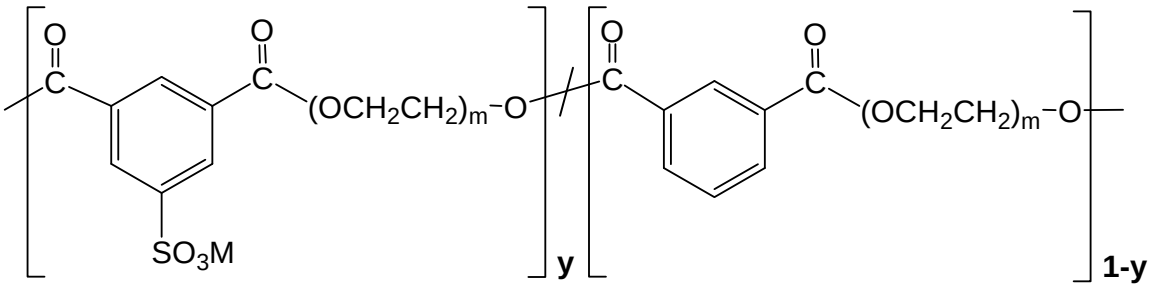

Scheme 5.1 PEO*x*-*y*M ionomers with well-defined PEO spacer (*x* = 400, 600, 1100 g/mol, and m = 9, 13, 25). M represents the cation (M = Li, Na, or Cs) associated with the sulfonate group and *y* represents percent of randomly charged phthalates (0, 17%, 49% and 100%).

5.2 Experimental Section

5.2.1 Materials: Poly(ethylene oxide) (PEO) based ionomers were prepared by a two-step melt polycondensation. Poly(ethylene glycol) diols of different molecular weights were reacted with a mixture of dimethyl 5-sulfoisophthalate sodium salt and neutral dimethyl isophthalate to give ionomers of varying ion contents. The detailed

synthesis procedures have been described in a previous publication.[31] ^{1}H nuclear magnetic resonance (NMR) verified the chemical structure, Scheme 5.1. The molecular weights of these ionomers range from 3k-10k g/mol, as published previously.[35] The molecular weights of PEO spacers are 400, 600, or 1100g/mol, which were determined by ^{1}H NMR. The cation was exchanged from sodium to lithium or cesium by aqueous diafiltration with an excess of LiCl or CsCl salts.[31] The concentrated ionomer solutions were freeze-dried after diafiltration and then vacuum-dried at 120 ^{o}C to constant mass. The ionomers are denoted as PEO*x*-*y*M, where *x* is the molecular weight of PEO spacers in g/mol, *y* is the percent of phthalates that are sulfonated in the ionomer, and M denotes the cation (M = Li, Na or Cs). For example, PEO600-49%Na designates the ionomer with PEO spacer length of 600 g/mol and 49% of the phthalates have -SO_3Na pendants on their phenyl rings. Note that there is no un-neutralized acid in any of the PEO-based ionomers studied in this paper. PEO600-0% refers to a neutral polymer that contains only neutral phthalates between the PEO spacers.

5.2.2 X-ray Scattering: To minimize the exposure of the materials to moisture, previously dried materials were loaded into the capillaries under vacuum at elevated temperatures (70-110 ^{o}C, depending on the viscosity of the ionomers). As the samples flow into the capillary under vacuum, bubbles are eliminated. The filled capillaries were cooled to room temperature under vacuum and then quickly flame sealed for X-ray scattering experiments. Alternatively, capillaries loaded with high-viscosity ionomers were kept open at both ends and stored under vacuum. Temperature scanning was performed from room temperature to 150 ^{o}C with a step size of 25 ^{o}C and a heating and cooling rate of 10 ^{o}C/min. The samples were equilibrated at each temperature for 10 min

before starting the X-ray data collection; typically, data collection times were 60 min/sample. Note that these ionomers have very low T_g (< 25 ^oC) and relatively low molecular weight,[35] so they are able to reach thermodynamic equilibrium rapidly. Previous rheological studies have showed that the terminal relaxation time of these materials is ~ 1 second or less at 30 ^oC.[31]

The multi-angle X-ray scattering system (MAXS) used Cu Kα X-ray from a Nonius FR 591 rotating-anode generator operated at 40 kV and 85 mA. The bright, highly collimated beam was obtained via Osmic Max-Flux optics and triple pin-hole collimation under vacuum. The scattering data were collected using a Bruker Hi-Star multiwire detector with sample to detector distances of 11 and 54 cm. The 2-D data reduction and analysis were performed using *Datasqueeze* software.[36] Background scattering from an empty capillary was subtracted from the samples' scattering.

Selected samples have been measured at the Advanced Photon Source at Argonne National Laboratory for comparison. The samples dried under high vacuum at 90^oC for a minimum of 3 days while using stainless steel cells with Kapton windows to define sample geometry. Immediately upon purging the oven with argon, the sandwich cells were hermetically sealed then allowed to reach room temperature. Variable-temperature SAXS data were collected using pinhole collimation on a Mar CCD detector at beamline 12-BM during beam conditions of 21 keV and 100mA. Variable-temperature USAXS data were collected using 2-D collimation and Bonse-Hart detector at beamline 32-ID during beam conditions of 12 keV and 90mA.[37] The heating and cooling rate was 10 ^oC/min, and samples were equilibrated for 40-60 minutes at set point value ± 1 ^oC; data

collection times were 10 min/sample. Data reduction and analysis were performed using the *Irena* macro package within *Igor* software.[38]

5.3 Results and Discussion

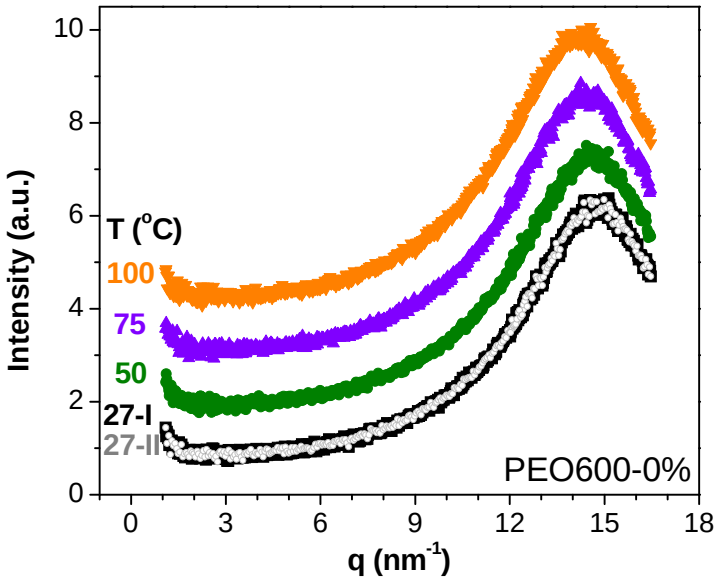

Figure 5.1 X-ray scattering data of PEO600-0% as a function of temperature. The scattering data at higher temperatures were vertically shifted for clarity. The amorphous peak shifts to lower angle as temperature is raised, due to the thermal expansion. The identical patterns at 27 oC before (black, 25-I) and after (grey, 25-II) heating indicate the changes in scattering are thermally reversible.

Figure 5.1 shows the variable-temperature X-ray scattering of PEO600-0% which does not contain any ionic groups. The amorphous peak at q ~ 15 nm^{-1} shifts slightly to lower q as the temperature increases, which is caused by the thermal expansion of the polymer. This expansion is reversible; as the sample is cooled it contracts, as shown by the identical scattering profiles collected at room temperature before and after the heating

cycle. The scattering data of PEO600-0% over a broader angular range (0.03 <q < 10 nm^{-1}) were also collected at Argonne National Laboratory at different temperatures. Patterns are unresponsive to temperature below q~1 nm^{-1} (see Appendix C - Figure C.1). Therefore, our discussion will focus only on the wide- angle region.

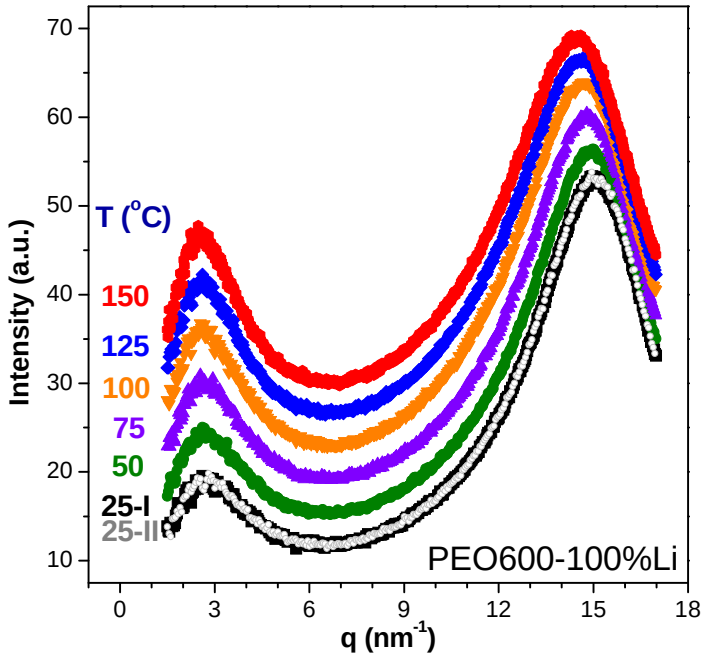

Figure 5.2 X-ray scattering data of PEO600-100%Li as a function of temperature. The scattering data at higher temperatures were vertically shifted for clarity. The intensity of the ionomer peak at q = 2-3 nm^{-1} increases with temperature. The identical patterns at 25°C before (black, 25-I) and after (grey, 25-II) heating indicate the morphology changes are thermally reversible.

Figure 5.2 shows the variable-temperature X-ray scattering of PEO600-100%Li. As the temperature increases, the intensity of the peak at ~2.7 nm^{-1} at room temperature increases, and the peak position shifts very slightly to lower angle (~2.5 nm^{-1} at 150 °C).

From our previous work on the room temperature morphology of these ionomers[35], this peak is the ionomer peak caused by interparticle scattering from ionic aggregates. The increase in ionomer peak intensity suggests an increase in the electron density contrast between the aggregates and matrix. As the temperature increases, the ionic aggregates experience much less thermal expansion than the PEO matrix due to their strong electrostatic interactions. The difference in the thermal expansion of matrix and aggregate would result in a net increase in electron density contrast. Additionally, the composition of the ionic aggregates might also become more ionic as the temperature is increased. Previous work has shown that ionic aggregates can contain non-ionic species, such as un-neutralized acids and backbone segments.[39] Ether oxygens from PEO have favorable interactions with the cations, and thus ionic aggregates might contain PEO chains. As temperature increases, there is an entropic driving force to expel flexible PEO backbones from the aggregates. This results in increased electron density of aggregates. The morphology in PEO600-100%Li is also thermally reversible, as exemplified by the identical scattering patterns at 25 ^{o}C before and after heating. Similar changes in X-ray scattering patterns with temperature were also observed in other Li-neutralized PEO ionomers, including PEO400-100%Li and PEO1100-100%Li. The X-ray scattering data of these ionomers are provided in Supporting Information.

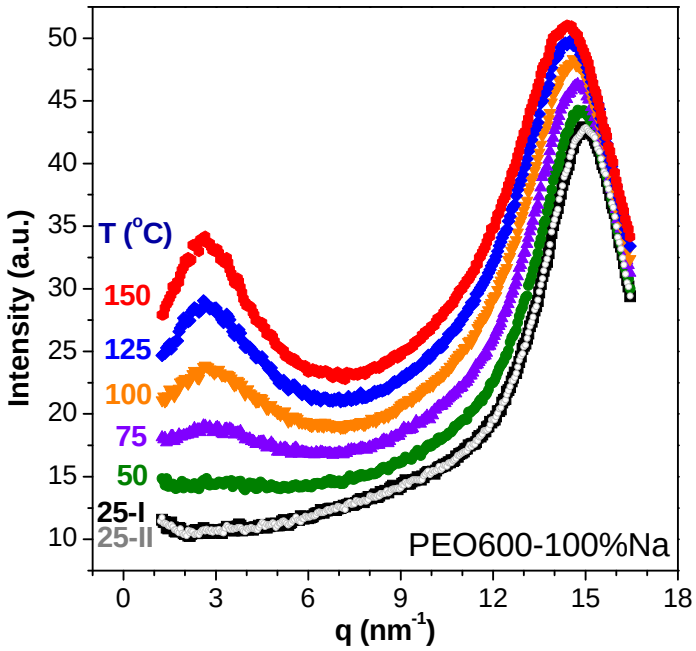

Figure 5.3 X-ray scattering data of PEO600-100%Na as a function of temperature. The scattering data at higher temperatures were vertically shifted for clarity. An ionomer peak gradually appears at q = 2-3 nm^{-1} as the temperature increases, indicating an increasing extent of microphase separation with increasing temperature. The identical patterns at 25°C before (black, 25-I) and after (grey, 25-II) heating indicate the morphology changes are thermally reversible.

Figure 5.3 shows the variable-temperature X-ray scattering of PEO600-100%Na. As temperature increases an ionomer peak at q ~ 2.5 nm^{-1} is formed. Its position is similar to that of the ionomer peak observed at all temperatures for PEO600-100%Li. The transition is gradual with the peak intensity increasing smoothly with temperature. From our previous work, the ionic groups in PEO600-100%Na exist in a range of states from isolated ion pairs to ionic aggregates at room temperature.[35] Due to the low number density of ionic aggregates as well as their possibly inhomogeneous size and spatial

distributions, no ionomer peak is observed at room temperature for PEO600-100%Na. The appearance of the ionomer peak indicates that the extent of ionic aggregation in PEO600-100%Na increases with temperature. Similar ionic aggregation behavior was observed in other Na-neutralized PEO ionomers, PEO400-100%Na and PEO1100-100%Na; see Supporting Information. These X-ray scattering results are consistent with recent findings from an infrared spectroscopic study of PEO600-100%Na ionomers.[40] Analysis of the SO_3^- symmetric stretching band shows that the relative population of aggregated SO_3^-, which vibrate as $2Na^+(SO_3^-)$, increases with increasing temperature, indicating an increasing extent of ionic aggregation.[40] The scattering data of PEO600-100%Na collected at Argonne National Laboratory shows no apparent changes in the scattering pattern at $q<1$ nm^{-1} as temperature is varied; see Supporting Information.

PEO ionomers neutralized with Cs show distinctly different behavior as a function of temperature, Figure 5.4. The broad peak at 7.5 nm^{-1} observed at room temperature disappears gradually as temperature increases while a new peak develops at lower q with increasing temperature. At 75 ^oC, the coexistence of both peaks is apparent. From our previous work by X-ray scattering and *ab initio* calculations, the Cs^+ and sulfonate groups in PEO600-100%Cs exist mainly in isolated ion pairs at room temperature.[35] The transition from a high-q peak to a low-q peak with increasing temperature indicates the reorganization of isolated ion pairs into ionic aggregates with larger correlation distances. Again, the PEO-based ionomers with shorter and longer PEO segments, PEO400-100%Cs and PEO1100-100%Cs, exhibit similar scattering profiles as a function of temperature; see Supporting Information; the PEO1100-100%Cs shows two clear peaks in addition to the amorphous peak at both 75 ^oC and 100 ^oC.

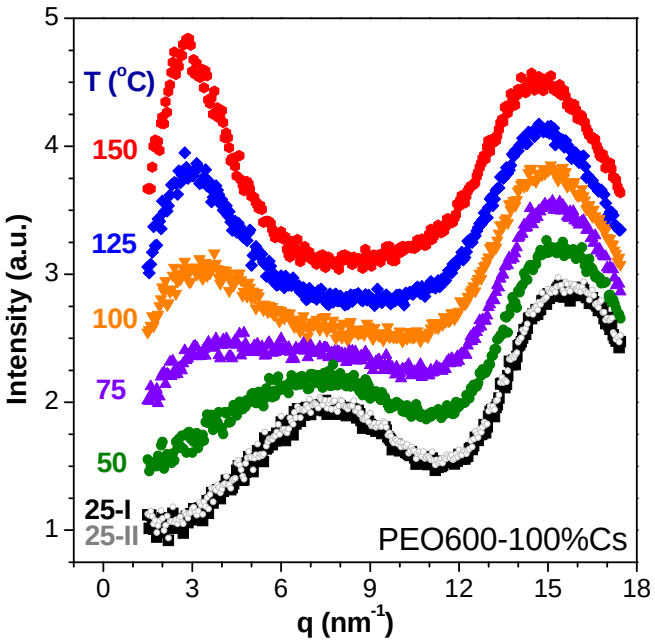

Figure 5.4 X-ray scattering data of PEO600-100%Cs as a function of temperature. The scattering data at higher temperatures were vertically shifted for clarity. An ionomer peak gradually appears at q = 2-3 nm^{-1} as the temperature increases, suggesting reorganization of ionic groups into ionic aggregates. The identical patterns at 25°C before (black, 25-I) and after (grey, 25-II) heating indicate the morphology changes are thermally reversible.

The ionomer peaks that are observed at elevated temperatures in PEO600-100%Na and PEO600-100%Cs and at all temperatures in PEO600-100%Li shift to lower angle as the temperature increases. To understand the effect of thermal expansion on the shift of the ionomer peak position, the average correlation distances between ionic aggregates are estimated from ionomer peaks using $2\pi/q^*$, Figure 5.5. For PEO600-100%Na and PEO600-100%Cs ionomers, ionomer peaks at 50°C and below are not identifiable without subtracting the scattering contribution from PEO600-0%. The polymer backbone-backbone correlation distances as a function of temperature are

determined from the amorphous peak positions for comparison. Interestingly, the correlation distances of both the ionomer peak and the amorphous halo decrease with increasing cation size at all temperatures. This is likely due to the different ionic association strengths and surface areas of cations, which cause different ionic aggregation morphologies.

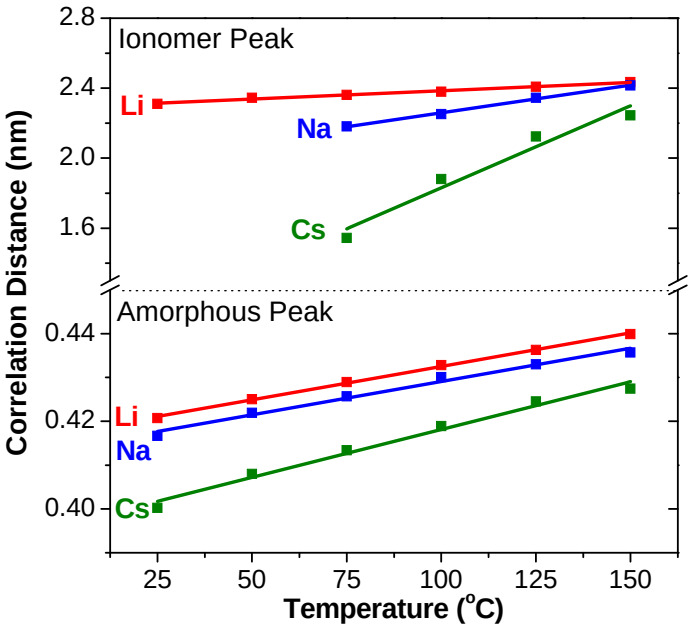

Figure 5.5 Correlation distance ($d = 2\pi/q^*$) of ionomer peaks and amorphous peaks in PEO600-100%M (M = Li, Na, and Cs) as a function of temperature.

The ionomer peak shows much stronger temperature dependence than the amorphous peak, suggesting that the increase in the inter-aggregates spacing is not simply caused by thermal expansion of the PEO matrix. Instead, the increase suggests that the ionic groups self-assemble into more strongly microphase separated ionic aggregates with larger inter-aggregate separation distances. This trend is more pronounced in Cs ionomers, in which the scatterers transition from ion pairs to aggregates. However, more accurate analysis of the size and number density of the ionic

aggregates would require structural modeling. The T_g of PEO-based ionomers is approximately room temperature or below.[35] Thus, direct imaging of the nanoscale ionic aggregates formed at elevated temperature using scanning transmission electron microscopy (STEM) is very challenging, because the nanometer-thick section will flow upon heating. Due to the lack of information regarding the shape of the ionic aggregates, we do not employ any structural model to fit the ionomer peak.

The X-ray scattering data of PEO*x*-100%Na (*x* = 400, 600, and 1100) at 150 ^{o}C are shown in Figure 5.6a. The ionomer peak increases in intensity and shifts to higher *q* as the ion content increases (the PEO segment length decreases). This is consistent with the ionomer peak arising from the inter-particle scattering between aggregates.[2, 4, 9, 11, 41] The average inter-aggregate spacing (*d*) obtained from the ionomer peak position ($d=2\pi/q^*$) at 150 ^{o}C in PEO$_x$-100%M follows a power law dependence on the ion content (*C*): $d \sim C^b$ (Figure 5.6b), where b = -0.26, -0.28, and -0.32 for Li, Na, and Cs respectively. For ionomer with relatively low ion content, i.e. the ionic aggregates do not connect with each other, if the size of ionic aggregates, number of ions in each aggregate, and percent of ions forming aggregates do not vary with ion concentration, then the scaling law would work and b=-1/3. The fact that *b* values for PEO-based ionomers are very close to the power relationship of -1/3 suggests that the ionic aggregation behaviors in these PEO-based ionomers at 150 ^{o}C are consistent in different ion contents. This is because our PEO-based ionomers have well-defined PEO spacers between the ionic groups. Previous work on random ionomers showed that *d* has much weaker dependence on the ion content *C*, *b* = -0.1 to -0.2.[12, 42] While for ionomers with regular spacing between ionic groups, such as sulfonated polyurethanes[13] or carboxy-telechelic

polyisoprenes,[15] -1/3 power law relationship works within experimental error,[42] consistent with our findings.

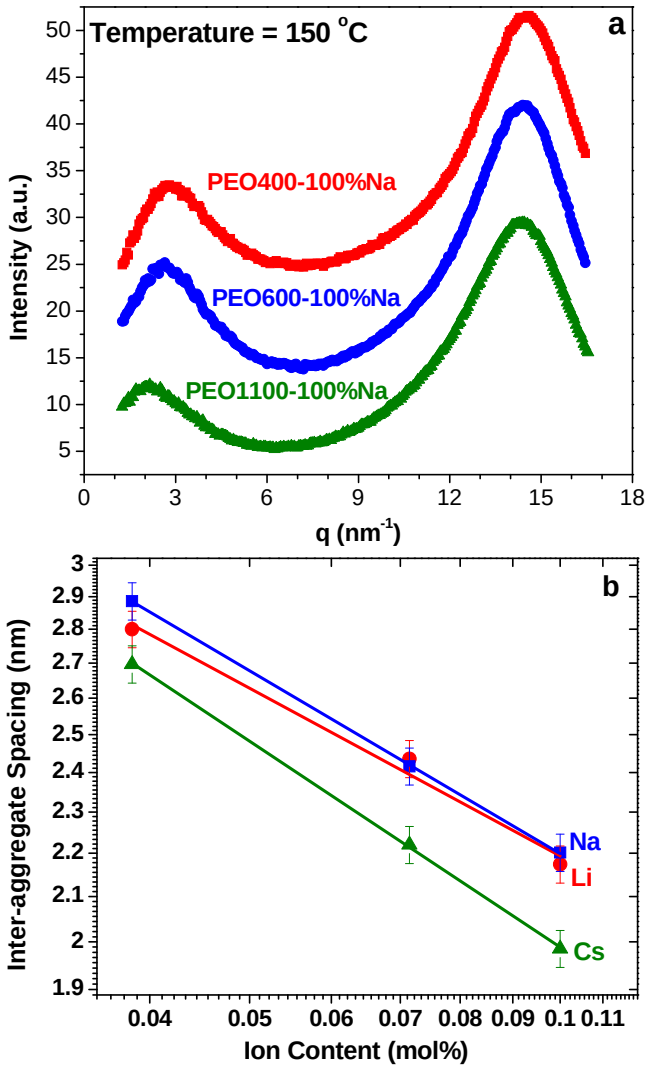

Figure 5.6 a) X-ray scattering data of PEO*x*-100%Na (*x* = 400, 600, and 1100 g/mol) at 150 °C. The ionomer peak position (q ~ 2-3 nm^{-1}) in PEO*x*-100%Na at 150°C shifts to higher scattering wavevector as *x* decreases because the ion content increases. b) The average inter-aggregate spacing (*d*) obtained from the ionomer peak position ($d=2\pi/q^*$) at 150 °C in PEO_x-100%M (M = Li: ●, Na: ■, and Cs: ▲) follows a power law dependence on the ion content. The lines are the best fit of the data with the allometric function.

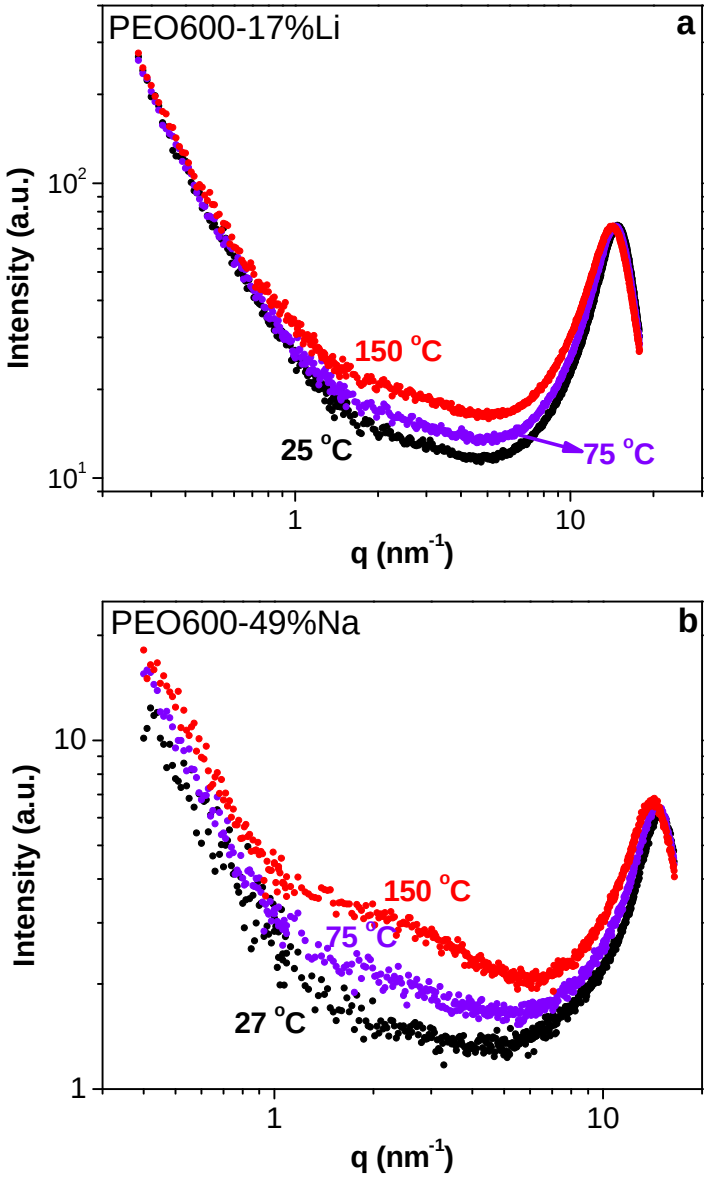

Figure 5.7 X-ray scattering data of PEO600-17%Li (a) and PEO600-49%Na (b) as a function of temperature. The morphology changes are thermally reversible.

Thus far, we have focused on the X-ray scattering profiles of PEO-based ionomers with well-defined PEO spacer length between the ionic groups. PEO600-17%Li and PEO600-49%Na with randomly separated ionic groups were also examined to investigate the effect of the ionic group's placement along the polymer backbone on ionic

association behaviors. Although the molecular weight of PEO spacer is still well-defined (600 g/mol), only 17% or 49% of the phthalates between the PEO segments have -SO_3M pendants on their phenyl rings. A mixture of charged and non-charged phthalates in the polymerization leads to more variable charge spacing for the partially sulfonated ionomers as compared to the fully sulfonated ionomers. In contrast to the fully charged ionomers (y = 100%, Figure 5.2), PEO600-17%Li only exhibits slight excess scattering at q = 1-4 nm^{-1} with increasing temperature, Figure 5.7a. A broad shoulder centered at q = 2-3 nm^{-1} develops at high temperatures for the randomly sulfonated PEO600-49%Na, Figure 5.7b. Although PEO600-49%Na has similar ion content as PEO1100-100%Na, the lack of a well-defined ionomer peak in PEO600-49%Na indicates that the size and/or spatial distribution of ionic aggregates are more disordered. Randomizing the placement of pendant ionic groups on the polymer backbone greatly reduces the order of ionic aggregation.

The formation of ionic aggregates in PEO-based ionomers with increasing temperatures is thermally reversible, i.e. the original morphology is recovered on cooling. Selected materials were thermally cycled several times, and the observed scattering patterns are independent of cycle number. As a result, the observed morphologies at both room temperature and higher temperatures are representative of equilibrated morphologies at each corresponding temperature. To the best of our knowledge, this study is the first report of temperature driven reversible formation of ionic aggregates in an ionomer system. The origin of ionic aggregation with increasing temperature in our ionomers differs from that of the Mn-SPS ionomer studied by Weiss *et al.*[17] mentioned in

the introduction, where *irreversible* formation of ionomer peak with temperature was observed.

The formation of ionic aggregates in PEO-based ionomers is likely entropic in origin. At room temperature, ether oxygens from PEO stabilize the ionic groups through ion-dipole interactions. The PEO chains lose a lot of entropy by adopting sequences of trans and gauche conformations. As the temperature increases, the interaction between PEO and the cations is reduced due to increased thermal energy and the PEO chains prefer to obtain greater entropy by releasing the ions. As a result, the capability of PEO to solvate ions decreases and the ionic groups aggregate by excluding the PEO from the ionic domains. Similar phase behavior with temperature have been observed in mixtures of poly(alkyl oxide) with salts[43-47] and polymer blends of poly(alkyl oxide) or polyamide with ionomers.[48-50] For example, Raman spectroscopic study of poly(propylene oxide) (PPO) and $NaCF_3SO_3$ mixture showed that the amount of dissociated free ions decreases with increasing temperature in an Arrhenius-type fashion.[44] Increasing temperature resulted in ion pairing or aggregation in poly(alkyl oxide) and salt mixtures, depending on the ion concentration, i.e. molar ratio of oxygen in polymer chain vs. cation.[44] In some cases, salt precipitation in the mixture of poly(alkyl oxide) with salts was observed as the temperature increased.[43, 47, 51] Schantz showed that the entropy of forming ion pair from free ions in PPO and $LiClO_4$ or $NaCF_3SO_3$ mixtures is very large and positive, confirming that entropy is an important driving force for microphase separation in poly(alkyl oxide)-based systems.[46] These studies are consistent with our findings in PEO-based ionomer systems by X-ray scattering. The uniqueness of PEO-based ionomers can be attributed to two aspects. The first is the extensive interaction between

the ionic groups and PEO chains, which makes the entropy driven microphase separation favorable at elevated temperatures. The second is the well-defined ion placement along the polymer backbone, greatly increasing the order of ionic self-assembly.

5.4 Conclusion

The temperature-dependent morphology of PEO-based ionomers neutralized with three different alkali cations have been studied by *in situ* X-ray scattering. The ionomer peak in PEO*x*-100%Li increases in intensity and shifts to slightly lower angle with increasing temperature. In PEO*x*-100%Na and PEO*x*-100%Cs, which have no ionomer peak at room temperature, reversible formation of an ionomer peak at q = 2-3 nm^{-1} was observed with increasing temperature. The formation of an ionomer peak with increasing temperature is attributed to the rearrangement of ionic groups into ionic aggregates of increasing order in size and spatial distribution, which could also be accompanied by increasing ionic composition in the aggregates. It is expected that the entropy of the ionomers increases with increasing extent of ionic aggregation, as the PEO chains can adopt more configurations by releasing the ionic groups. Although the morphology in PEO600-100%M (M = Li, Na and Cs) ionomers are greatly affected by the cation type at room temperature, they all exhibit similar ionic association behaviors at 150 ^{o}C, as indicated by a well-defined ionomer peak at similar scattering angles. This behavior suggests reduced PEO-cation interactions and a greater degree of ionic aggregation at elevated temperature.

5.5 Reference

1. Eisenberg, A.; Kim, J.-S., *Introduction to Ionomers*. John Wiley & Sons: New York, 1998.

2. Yarusso, D. J.; Cooper, S. L. *Macromolecules* **1983,** 16, 1871-1880.

3. Brozoski, B. A.; Coleman, M. M.; Painter, P. C. *Macromolecules* **1984,** 17, 230-234.

4. Yarusso, D. J.; Cooper, S. L. *Polymer* **1985,** 26, 371-378.

5. Coleman, M. M.; Lee, J. Y.; Painter, P. C. *Macromolecules* **1990,** 23, 2339-2345.

6. Winey, K. I.; Laurer, J. H.; Kirkmeyer, B. P. *Macromolecules* **2000,** 33, 507-513.

7. Grady, B. P. *Polym. Eng. Sci.* **2008,** 48, 1029-1051.

8. Macknight, W. J.; Taggart, W. P.; Stein, R. S. *J. Polym. Sci. Part C: Polym. Symp.* **1974,** 45, 113-128.

9. Marx, C. L.; Caulfield, D. F.; Cooper, S. L. *Macromolecules* **1973,** 6, 344-353.

10. Benetatos, N. M.; Chan, C. D.; Winey, K. I. *Macromolecules* **2007,** 40, 1081-1088.

11. Benetatos, N. M.; Heiney, P. A.; Winey, K. I. *Macromolecules* **2006,** 39, 5174-5176.

12. Weiss, R. A.; Lefelar, J. A. *Polymer* **1986,** 27, 3-10.

13. Ding, Y. S.; Register, R. A.; Yang, C. Z.; Cooper, S. L. *Polymer* **1989,** 30, 1213-1220.

14. Wang, J.; Li, Y. J.; Peiffer, D. G.; Chu, B. *Macromolecules* **1993,** 26, 2633-2635.

15. Williams, C. E.; Russell, T. P.; Jerome, R.; Horrion, J. *Macromolecules* **1986,** 19, 2877-2884.

16. Page, K. A.; Cable, K. M.; Moore, R. B. *Macromolecules* **2005,** 38, 6472-6484.

17. Galambos, A. F.; Stockton, W. B.; Koberstein, J. T.; Sen, A.; Weiss, R. A.; Russell, T. P. *Macromolecules* **1987,** 20, 3091-3094.

18. Register, R. A.; Sen, A.; Weiss, R. A.; Cooper, S. L. *Macromolecules* **1989,** 22, 2224-2229.

19. Colby, R. H.; Zheng, X.; Rafailovich, M. H.; Sokolov, J.; Peiffer, D. G.; Schwarz, S. A.; Strzhemechny, Y.; Nguyen, D. *Phys. Rev. Lett.* **1998,** 81, 3876-3879.

20. Tierney, N. K.; Register, R. A. *Macromolecules* **2002,** 35, 2358-2364.

21. Navratil, M.; Eisenber.A. *Macromolecules* **1974,** 7, 84-89.

22. Tierney, N. K.; Register, R. A. *Macromolecules* **2003,** 36, 1170-1177.

23. Earnest, T. R.; Macknight, W. J. *J. Polym. Sci., Part B: Polym. Phys.* **1978,** 16, 143-157.

24. Weiss, R. A.; Fitzgerald, J. J.; Kim, D. *Macromolecules* **1991,** 24, 1071-1076.

25. Wright, P. V. *MRS Bull.* **2002,** 27, 597-602.

26. Wright, P. V. *British Polymer Journal* **1975,** 7, 319-327.

27. Xu, K. *Chem. Rev.* **2004,** 104, 4303-4417.

28. Armand, M. B.; Chabagno, J. M.; Duclot, N. J., In *Fast Ion Transport in Solids*, Vashishta, P.; Mundy, J. N.; Shenoy, G. K., Eds. North Holland, New York 1979; p 131.

29. Meyer, W. H. *Adv. Mater.* **1998,** 10, 439-448.

30. Ratner, M. A., In *Polymer Electrolyte Reviews*, MacCallum, J. R.; Vincent, C. A., Eds. Elsevier: New York, 1987; Vol. 1.

31. Dou, S. C.; Zhang, S. H.; Klein, R. J.; Runt, J.; Colby, R. H. *Chem. Mater.* **2006,** 18, 4288-4295.

32. Fragiadakis, D.; Dou, S.; Colby, R. H.; Runt, J. *J. Chem. Phys.* **2009,** 130, 064907.

33. Fragiadakis, D.; Dou, S. C.; Colby, R. H.; Runt, J. *Macromolecules* **2008,** 41, 5723-5728.

34. Klein, R. J.; Zhang, S. H.; Dou, S.; Jones, B. H.; Colby, R. H.; Runt, J. *J. Chem. Phys.* **2006,** 124, 144903.

35. Wang, W.; Liu, W.; Tudryn, G. J.; Colby, R. H.; Winey, K. I. *Macromolecules* **2010,** 43, 4223-4229.

36. Heiney, P. A. *Commission on Powder Diffraction Newsletter* **2005,** 32, 9-11.

37. Ilavsky, J.; Jemian, P. R.; Allen, A. J.; Zhang, F.; Levine, L. E.; Long, G. G. *J. Appl. Crystallogr.* **2009,** 42, 469-479.

38. Ilavsky, J.; Jemian, P. R. *J. Appl. Crystallogr.* **2009,** 42, 347-353.

39. Wang, W.; Chan, T. T.; Perkowski, A. J.; Schlick, S.; Winey, K. I. *Polymer* **2009,** 50, 1281-1287.

40. Lu, M.; Runt, J.; Painter, P. *Macromolecules* **2009,** 42, 6581-6587.

41. Macknigh.Wj; Taggart, W. P.; Stein, R. S. *Journal of Polymer Science Part C-Polymer Symposium* **1974,** 45, 113-128.

42. Tomita, H.; Register, R. A. *Macromolecules* **1993,** 26, 2791-2795.

43. Teeters, D.; Frech, R. *Solid State Ionics* **1986,** 18-9, 271-276.

44. Kakihana, M.; Schantz, S.; Torell, L. M. *J. Chem. Phys.* **1990,** 92, 6271-6277.

45. Schantz, S.; Torell, L. M.; Stevens, J. R. *J. Chem. Phys.* **1991,** 94, 6862-6867.

46. Schantz, S. *J. Chem. Phys.* **1991,** 94, 6296-6306.

47. Bastek, J.; Stolwijk, N. A.; Köster, T. K.-J.; van Wüllen, L. *Electrochim. Acta* **2010,** 55, 1289-1297.

48. Hara, M.; Eisenberg, A. *Macromolecules* **1987,** 20, 2160-2164.

49. Lu, X. Y.; Weiss, R. A. *Macromolecules* **1995,** 28, 3022-3029.

50. Feng, Y.; Weiss, R. A.; Han, C. C. *Macromolecules* **1996,** 29, 3925-3930.

51. Wintersgill, M. C.; Fontanella, J. J.; Greenbaum, S. G.; Adamic, K. J. *British Polymer Journal* **1988,** 20, 195-198.

Chapter 6

Morphology of Segmented Poly(tetramethylene oxide)-Based Polyurethanes Containing Phosphonium Salts

6.1 Introduction

Polyurethanes are useful thermoplastic elastomers due to their superior mechanical strength and elastomeric behavior derived from microphase separation of soft and hard segments and hydrogen bonding.[1] The hard segments are prepared by reaction of an isocyanate with a low molecular weight diol chain extender, and the soft segments are typically based on a low T_g polyol. Polyurethanes are used in many applications such as abrasion-resistant components, biomaterials, durable coatings, and foams.[2-8]

Polyurethane ionomers have also received intense attention as high-strength elastomers for biomedical[9, 10] and conductive polymer[11-14] applications. Incorporation of ions into macromolecular structure causes formation of more complex morphological features and drastically influences the thermal and mechanical behavior of polyurethane ionomers. Ions can increases or reduce the degree of microphase separation, depending on the location of the ionic group and polymer composition.[15] Early reports of cation-containing polyurethanes usually involved postpolymerization functionalization to introduce quaternary ammonium groups.[16-18] Anionic polyurethanes, which commonly consist of either sulfonate or carboxylate groups in the hard segment, are more prevalent in the literature. Many researchers have modeled the presence of ionic aggregates within the microphase-separated polyurethane morphology.[19-23]

The literature on phosphonium halide salt containing polymers is abundant. However, to our knowledge, researchers have not reported the synthesis of polyurethanes containing phosphonium groups in the hard segment. McGrath *et al.* reported the synthesis of poly(arylene ether) phosphonium ionomers for high-performance polymers in a variety of applications including ion-exchange membranes and conductive polymers.[24] However, in sharp contrast to our work, the phosphonium ionomers were prepared via reduction of polymeric phosphine oxides to phosphines and subsequently quaternizing the phosphines with alkyl halides. Lindsell *et al.* reported synthesis and characterization of telechelic poly(butadiene) based elastomers that contained phosphonium ions.[25] A temperature dependence of the ionic aggregate interactions was observed with dynamic mechanical thermal analysis, and the ionic aggregates dissociated at temperatures ranging from 70 to 120 °C.[25] Mather *et al.* recently reported the synergy of ionic interactions and hydrogen bonding where phosphonium salts containing a uracil hydrogen bond were blended with adenine-containing ABA triblock copolymers.[26] Addition of the ionic guest altered the dynamic mechanical behavior and morphology compared to the polymer in the absence of the cationic phosphonium salt. It was concluded that the phosphonium salt was located in the adenine-containing blocks. X-ray scattering indicated a change in morphology from cylindrical to lamellar structure as the uracil-containing phosphonium salt was incorporated. ^{1}H NMR spectroscopy revealed complementary hydrogen bonding in the presence of the phosphonium salt.

In this work, urethane hydrogen bonding and phosphonium salt functionality were incorporated into the same polyurethane to elucidate the fundamental structure-property relationships of phosphonium-containing polyurethanes. This differs from the previous

work described above, where the ionic group was the guest molecule and hydrogen bonding was based on more sophisticated complementary structures. Specifically, the effect of ionic interactions in a polyurethane hard segment on morphology and mechanical properties was elucidated using a variety of complementary analytical techniques. Appropriate noncharged polyurethanes containing only urethane hydrogen-bonding interactions were prepared for comparison.

6.2 Experimental

The materials synthesis, NMR, FAB-MS, thermogravimetric analysis, dynamic mechanical analysis, FTIR, and tensile tests were performed by Sharlene Williams in Professor Timothy Long's Group at Virginia Tech.

6.2.1 Synthesis: PTMO oligomer (Terathane, Du Pont) with number-average molecular weight of 2000 g/mol and 1,4-butanediol were purchased from Aldrich and dried *in vacuo* (0.1 mmHg) at 23 °C for 24 h prior to use. Bayer kindly provided bis(4-isocyanatocyclohexyl)methane (HMDI) with purity greater than 99.5%. Chloroform ($CHCl_3$, Fisher Scientific, Optima grade) was distilled from calcium hydride. Tetrahydrofuran (THF, EMD Science, HPLC grade), hexanes (Fisher Scientific, HPLC grade), dichloromethane (Fisher Scientific, HPLC grade), and diethyl ether (Fisher Scientific, 99.9%, anhydrous) were used as received. Dibutyl tin dilaurate (DBTDL, 99%) was dissolved in THF as a 1 wt % solution. A mixed solvent recrystallization was used to purify 1,4-bis(diphenylphosphino)butane (Aldrich, 98%) using hexanes and dichloromethane under nitrogen. Recrystallization was performed under nitrogen to

minimize phosphine oxide formation. ^{31}P NMR spectroscopy revealed one peak after recrystallization. 2-Bromoethanol (Aldrich, 95%) was distilled prior to use.

Synthesis of butane-1,4-bis[(2-hydroxyethyl)diphenylphosphonium] bromide chain extender: in a two-necked, round-bottomed flask equipped with a stir bar and condenser, 1,4-bis(diphenylphosphino)butane (5.694 g, 0.0134 mol) was introduced and purged under nitrogen. Chloroform (dry, 15 mL) and 2-bromoethanol (2.83 mL, 0.0401 mol) were subsequently syringed into the flask. The reaction was allowed to proceed at 60 °C for 24 h. The reaction product was precipitated into diethyl ether twice. The final product was obtained in 90 % yield. ^{1}H NMR (400 MHz, CD_3Cl_3) δ = 7.56-7.80 (m, 20H), 5.36 (s, 2H), 3.88-3.97 (m, 4H), 3.46 (m, 4H), 3.19 (m, 4H), 1.99 (m, 4H). FAB MS: M+Br = 595.15 (found), molecular weight = 515.25 (calculated). Melting point = 123.8-124.1 °C.

Synthesis of polyurethanes: all reactions were conducted in three-necked, round-bottomed flasks that were equipped with an addition funnel, nitrogen inlet, and overhead stirrer. In the first step, HMDI end-capped PTMO prepolymers were prepared in the absence of solvent at 80 °C with 1 wt % DBTDL in THF (0.01 mL) as the catalyst.[1] In the second step, the chain extenders were dissolved in $CHCl_3$ (20 wt % solids), and the polyurethanes were prepared via the dropwise addition (over 60 min) of the chain extender solution into the HMDI end-capped PTMO prepolymer. Polymerizations were allowed to proceed for 24 h at 80 °C, and the solutions remained homogeneous throughout the polymerization. The polymer films containing butane diol chain extenders were optically clear; however, films containing butane-1,4-bis[(2-

hydroxyethyl)diphenylphosphonium] bromide were opaque. Hard segment content was deduced using the following equation:

$$\text{Hard segment content} = 100 \times \frac{(\text{HMDI+Chain Extender})}{(\text{HMDI+Chain Extender+PTMO})} \tag{6.1}$$

6.2.2 Molecular Structure Characterization: ^{1}H NMR spectroscopy was utilized to determine monomer composition in $CDCl_3$ at 23 °C with a 400 MHz Varian UNITY spectrometer. FAB-MS was obtained on a JOEL HX110 dual focusing mass spectrometer.

6.2.3 Thermal and Mechanical Analysis: A TA Instruments Hi-Res TGA 2950 with a temperature ramp of 10 °C/min in a nitrogen atmosphere was used for thermogravimetric analysis (TGA). Dynamic mechanical analysis (DMA) was conducted on a TA Instruments Q800 dynamic mechanical analyzer in tension mode at a frequency of 1 Hz and temperature ramp of 3 °C/min. The sample was cooled from room temperature to -30 °C prior to heating. The glass transition temperature (T_g) was determined at the peak of the tan δ curve. Differential scanning calorimetry (DSC) was performed using a TA Instruments Q2000 differential scanning calorimeter under a nitrogen flow of 50 mL/min. The sample was first heated from -20 °C to 200 °C at a heating rate of 10 °C/min and held for 5 min to minimize the effect of thermal history. The cooling rate was 10 °C/min, and a subsequent heating from -130 °C to 200 °C at a heating rate of 5 °C/min was conducted. Dogbone-shaped film specimens, which were cut with a die according to ASTM D3368 specifications, were used for tensile tests performed on a 5500R Instron universal testing instrument with a cross-head speed of 50 mm/min using manual grips at 23 °C.

6.2.3 Morphological Characterization: Morphological analysis was conducted using a variety of complementary techniques. X-ray scattering was performed on solvent-cast polyurethane films that were dried *in vacuo* (0.1 mm Hg) at 60 °C for 24 h to ensure complete removal of $CHCl_3$. The multi-angle X-ray scattering system (MAXS) used Cu X-ray from a Nonius FR 591 rotating-anode generator operated at 40 kV and 85 mA. The bright, highly collimated beam was obtained via Osmic Max-Flux optics and pin collimation in an integral vacuum system. The scattering data were collected using a Bruker Hi-Star multiwire detector with a sample to detector distance of 7, 11, 54 and 150 cm. The MAXS system provides an uncommonly wide range of scattering angle that was critical in evaluating the morphology of these segmented copolymers. The 2-D data reduction and analysis were performed using *Datasqueeze* software.[27]

Scanning transmission electron microscopy (STEM) specimens were sectioned from solvent-cast and dried films using a Reichert-Jung ultramicrotome equipped with a cryo unit operated at -145 °C. Thin sections with nominal thickness of 50 nm were obtained with a dry diamond knife and transferred onto copper grids. The grids were stored in a vacuum desiccator at room temperature prior to imaging. STEM experiments were performed using a JEOL 2010F field emission scanning transmission electron microscope equipped with a Gatan Image Filter (GIF). High-angle annular dark field (HAADF) images were recorded with a 0.7 nm STEM probe at an accelerating voltage of 200 keV. X-ray energy-dispersive spectroscopy (EDS) experiments were performed in a JEOL 2010F, which is equipped with a Princeton Gamma Tech (PGT) X-ray energy-dispersive spectrometer and a Bruker digital processing unit. Spectra were acquired

through the placement of a stationary 0.7 nm probe at the point of interest and collecting a spectrum for 60 s. Data analysis was performed with the ESPRIT EDS Software.

The extent of hydrogen bonding of solvent-cast films was evaluated using a MIDAC M2004 ATR-FTIR at ambient conditions. The spectra, including the background scan, were collected at a resolution of 4 cm^{-1}, and 128 scans were averaged. In all characterizations, great care was used in drying polymer samples before testing.

6.3 Results and Discussion

6.3.1 Synthesis: A novel ion-containing polyurethane was synthesized in a two-step process using 2000 g/mol PTMO as the soft segment, HMDI as the diisocyanate, and butane-1,4-bis[(2-hydroxyethyl)diphenylphosphonium] bromide as the chain extender (Scheme 6.1). The phosphonium-based polyurethanes containing PTMO soft segments and HMDI was referred to as PTMO-HMDI-P+. The prepolymer method was utilized to synthesize novel polyurethanes, and the first step involved the conventional preparation of an oligomeric HMDI end-capped PTMO.[1] After the reaction was cooled to room temperature, films were cast directly from the reaction mixture. For comparative purposes, noncharged polyurethanes containing a 1,4-butanediol chain extender were synthesized (PTMO-HMDI-BD). The chemical compositions of both the ion-containing and noncharged polyurethanes were similar. Each polymer had an equal concentration of hard segment on a mol % basis, and a similar content on a wt % basis, based on Eq. 6.1 in the Experimental Section. These values were calculated based on the charged amounts of reactants. PMTO-HMDI-P+ contained 75 mol % and 37 wt % hard segment, and PTMO-HMDI-BD possessed 75 mol % and 24 wt % hard segment. Researchers have

shown that using 1,4-butanediol as a chain extender resulted in polyurethanes that possessed excellent tensile properties and elasticity.[3] For this reason, 1,4-butanediol was utilized as the chain extender in the noncharged polyurethanes.

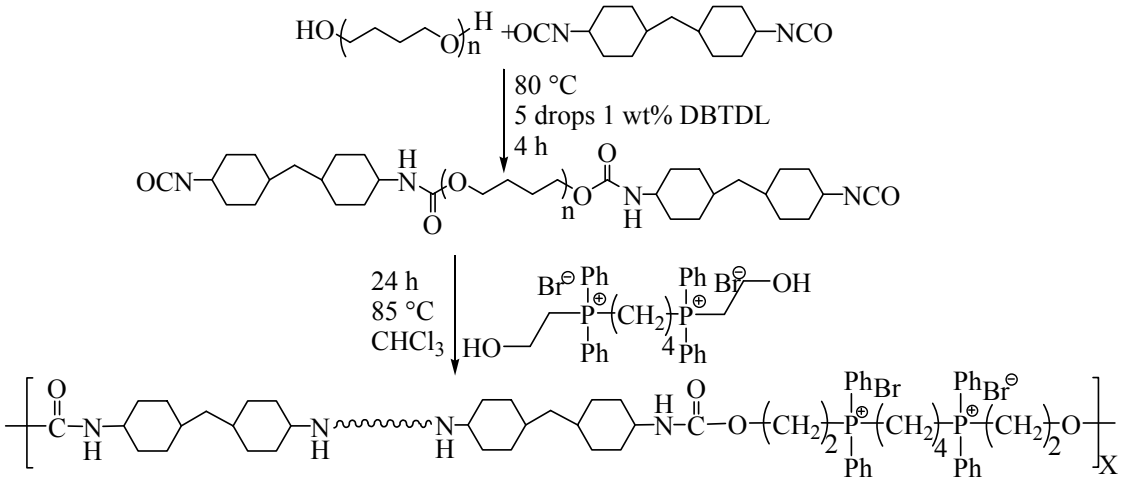

Scheme 6.1 Synthesis of phosphonium-containing polyurethanes (PTMO-HMDI-P+).

6.3.2 Thermal Properties: The PTMO-HMDI-P+ polyurethane had a T_d of 280 °C, and the PTMO-HMDI-BD noncharged polyurethane had a slightly lower T_d of 263 °C, according to TGA data. The difference in thermal stability is considered insignificant since the error in TGA is approximately 2 %, and the thermal stability difference between the two types of polyurethanes was only 17 °C.

DSC provided interesting information about crystallinity differences between the phosphonium bromide containing and noncharged polyurethanes and confirmed many of the DMA results described below. Both DSC traces (Figure 6.1) are from the second heat in order to minimize effects of thermal history. The phosphonium polyurethane possessed crystallinity, and a T_g, T_c, and T_m were observed on heating (5 °C/min) at -79 °C, -35 °C, and 14 °C, respectively. Conversely, only a T_g at -78 °C was observed for

the noncharged polyurethane. Based on this observation, it appeared that hydrogen bonding restricted the mobility of the polymer chain and reduced the crystallinity of PTMO segment for the noncharged polyurethanes. This was in agreement with Schneider et al., who reported that hydrogen bonding occurred between ether oxygens within the soft segment and urethane and urea units, and thus hindered crystallization of the soft segment.[28] Moreover, the organic nature and bulkiness of the ionic groups suggested less dense packing of ionic groups in the aggregates; thus, the geometric constraint on the PTMO segments surrounding the ionic aggregates was much less than those traditional ionomers with metal cations.

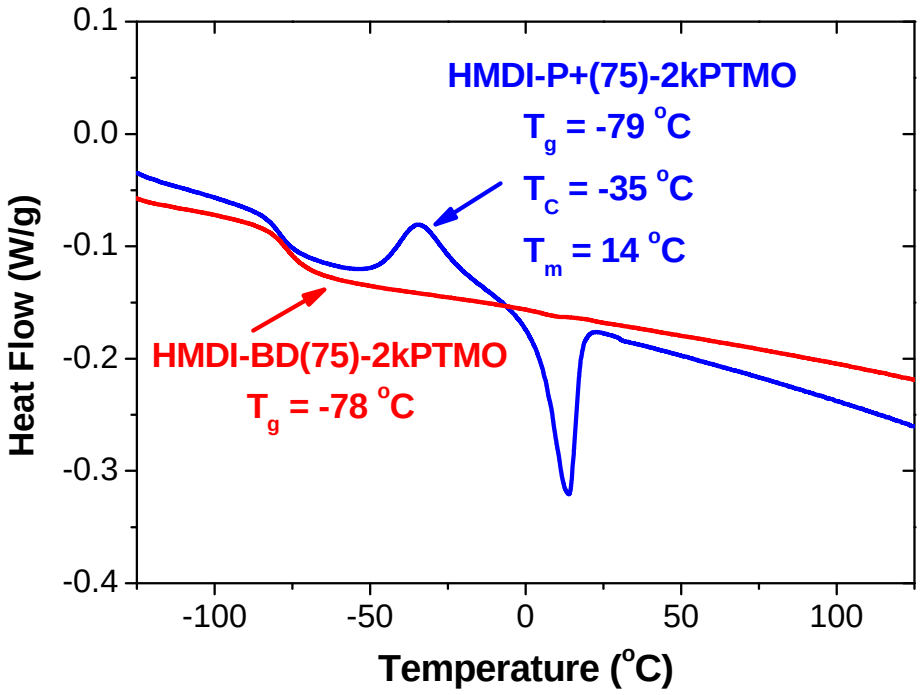

Figure 6.1 DSC traces for PTMO-HMDI-P+ (dashed lines and arrows), and PTMO-HMDI-BD (solid lines and arrows). Conditions: 5 °C/min, 2nd heat.

6.3.3 Dynamic Mechanical Behavior: Figure 6.2 summarizes the comparative dynamic mechanical behavior of the phosphonium-containing and noncharged polyurethanes, PTMO-HMDI-P+ and PTMO-HMDI-BD. Both polymers showed similar PTMO soft segment T_gs, with values ranging from -60 to -64 °C. This transition was higher than pure PTMO (-79 °C), which suggested some phase mixing. The greater modulus of the phosphonium polyurethane indicated that the polymer had higher crystallinity, which was consistent with DSC as described above. This is in agreement with Wilkes et al., where they reported that the presence of PTMO crystals increased the glassy modulus.[29] A second transition that caused a decrease in the storage modulus occurred in the phosphonium-containing polyurethane at 47 °C, and this was attributed to the melting of the crystalline PTMO segments.[28] The same transition occurred in the PTMO-HMDI-BD polyurethanes but to a much lesser extent since the decrease in modulus is very slight. The higher modulus in the rubbery plateau region (30 MPa) for the noncharged polyurethane suggested a greater extent of hydrogen bonding[30] in comparison to the phosphonium polyurethane, which had a lower rubbery plateau modulus (1 MPa). The lower plateau modulus could also suggest that the phosphonium polyurethane had a lower entanglement density,[31-33] which was possibly due to the presence of bulky aryl groups around the phosphonium cations. Both polymers possessed similar flow temperatures at ~135 °C, and retained a relatively flat rubbery plateau modulus prior to the onset of flow. It is interesting that both polyurethanes have similar flow temperatures, which indicated that the ionic aggregates persist to approximately the same temperature as the urethane hydrogen bonds.

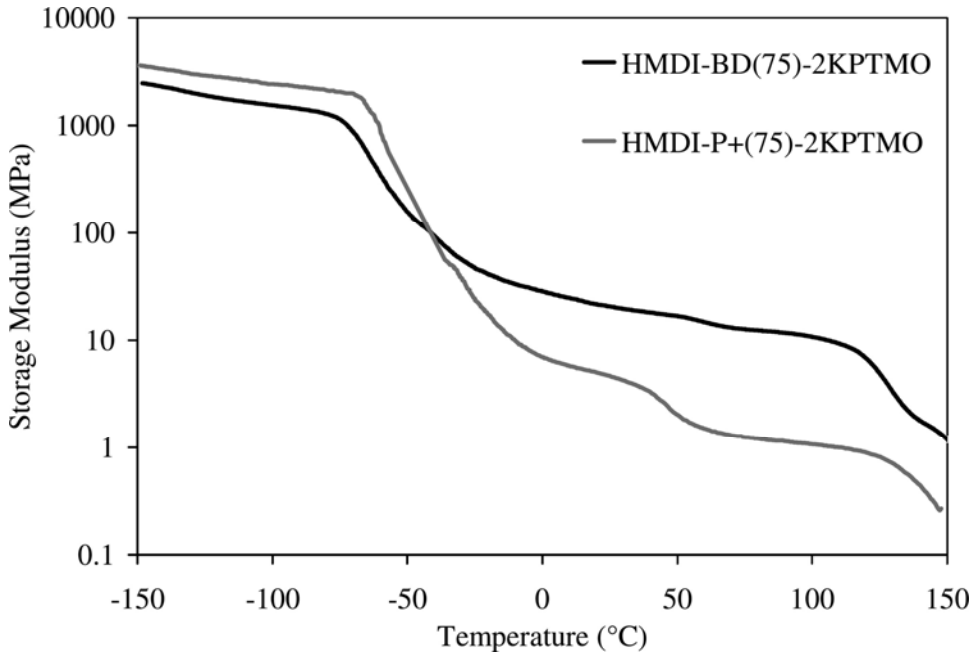

Figure 6.2 DMA curves demonstrating the transitions of the phosphonium-containing (dashed line) and noncharged polyurethanes (solid line). Conditions: 3 °C/min, 1 Hz, film tension mode.

6.3.4 Morphology: Figure 6.3 shows the X-ray scattering data plotted in log-log scale. PTMO oligomers (M_n = 2000 g/mol) used in the synthesis of the polyurethanes were highly crystalline, showing two sharp crystalline reflection peaks at angular positions of 14 nm^{-1} and 17 nm^{-1}, which corresponded to (020) and (110) peaks of PTMO crystals.[34] The PTMO oligomers also showed three crystalline lamellae-lamellae peaks at 0.36 nm^{-1}, 0.78 nm^{-1}, and 1.23 nm^{-1} that corresponded to a spacing of 16.3 nm. PTMO typically crystallizes into a monoclinic crystal structure with molecular chains having a planar zigzag conformation along the c axis of the unit cell.[35] The length of a fully extended, crystalline PTMO chain of 2000 g/mol is ~16.8 nm, which is comparable to the inter-lamellar spacing measured via X-ray scattering.

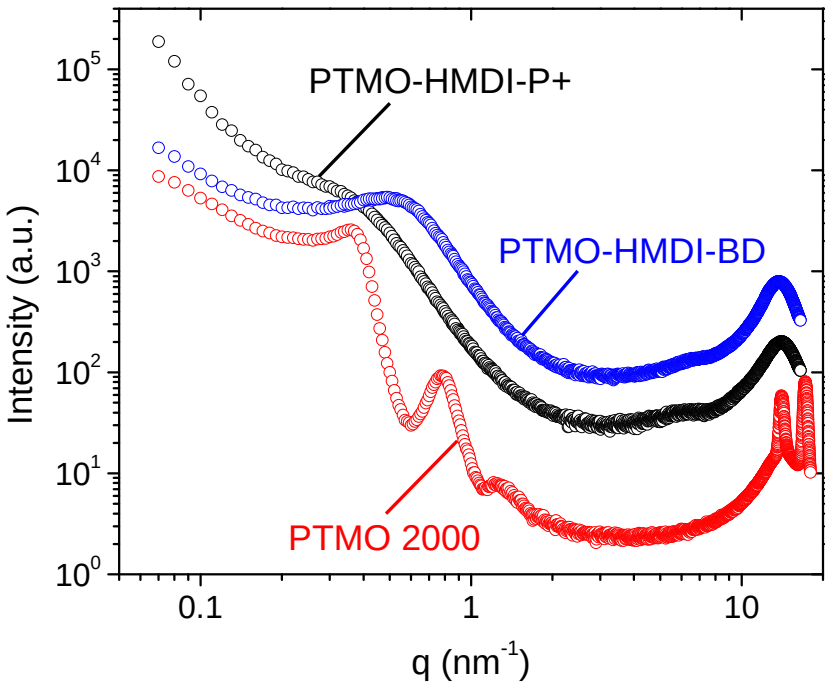

Figure 6.3 X-ray scattering intensity vs. scattering vector (q) plotted in log-log scale for unstretched PTMO oligomer and unstretched PTMO-based polyurethane films containing different chain extenders.

The scattering data of both PTMO-HMDI-P+ and PTMO-HMDI-BD displayed an amorphous peak at ~14 nm^{-1}, arising from PTMO soft segment.[34] In addition, both charged and noncharged polyurethanes also showed a weak broad peak at ~6 nm^{-1} that was absent in the pure PTMO oligomer X-ray profile. This broad peak was attributed to the intramolecular scattering from the diisocyanate hard segments. The amorphous nature of both the soft and hard segments detected via X-ray scattering at room temperature was consistent with DSC results, which showed a T_m of PTMO at 14 °C for PTMO-HMDI-P+ and non-crystalline behavior of PTMO-HMDI-BD. The crystallinity of hard segments is highly dependent on the structure and symmetry of diisocyanate groups.[55] Wilkes et al. previously showed that hard segments containing a kinked

diisocyanate structure or a mixture of isomers, i.e. HMDI in this case, are less able to form ordered crystalline structures,[56] as observed herein.

In addition to the two higher angle peaks, PTMO-HMDI-BD also demonstrated a well-defined scattering peak at an angular position of ~0.49 nm^{-1}, indicating microphase separation. This scattering peak is believed to arise from the interparticle scattering of hard domains with an average interdomain spacing of ~12.8 nm in PTMO-HMDI-BD. Others have observed the incompatibility between soft and hard segments resulting in the formation of microphase-separated structures in various segmented polyurethane elastomers.[36-40] Small-angle X-ray scattering data also revealed a broad peak for PTMO-HMDI-P+ at a lower angle relative to the noncharged polyurethane, and this peak appeared less distinct due to the overlap with the small-angle upturn. The degree of microphase separation is highly dependent on the chemical composition. The PTMO-HMDI-BD polyurethanes did not possess bulky ionic groups in the middle of the urethane hard segments and thus had better packing of the hard segments to form well-defined microphase-separated domains. For polyurethanes containing ionic groups, there were two driving forces for microphase separation, namely hydrogen-bonding interactions and ionic interactions. Additional experiments described below, were conducted to clarify the morphology of the materials.

Scanning transmission electron microscopy (STEM) was applied to directly image the nanoscale morphology of PTMO-HMDI-P+. The high-angle annular dark-field (HAADF) STEM image of PTMO-HMDI-P+ (Figure 6.4a) showed bright, circular ion-rich regions dispersed in dark, hydrocarbon-rich matrix. The mean diameter of STEM features was 43 nm ± 15 nm (Figure 6.4b), which was determined using Gaussian

fits to line scans of intensity on >50 ionic aggregates. The size of ionic aggregates observed in STEM images was unexpected given the angular position of the broad X-ray scattering peak (Figure 6.3), which was ~ 0.2-0.4 nm^{-1}. It is important to note that polyurethanes are potentially hydrophilic due to the presence of hydrogen bonds. Thus, the ultrathin films used for STEM imaging might have absorbed water after cryomicrotome during grid transfer in ambient conditions. This moisture was difficult to remove under room temperature vacuum in the microscope. The extensive projection overlap in the STEM images and the diffuse boundary of the bright features also increased the error during measurement of the feature sizes. These ionic aggregates in the phosphonium polyurethane were much bigger than those observed in ion-containing vinyl polymers, such as sulfonated polystyrene and poly(styrene-*ran*-methacrylic acid) copolymers neutralized with metal cations.[41, 42] Previous STEM images of those solvent-cast ionomers have shown monodisperse, spherical ionic aggregates of 1-2 nm in diameter.[41, 42] The large size of ionic aggregates observed here might have partially resulted from the bulkiness of the phosphonium ions, which each possess two phenyl groups. In addition, the rigid diisocyanate hard segments adjacent to the ionic groups may also participate in the observed ion-rich aggregates.

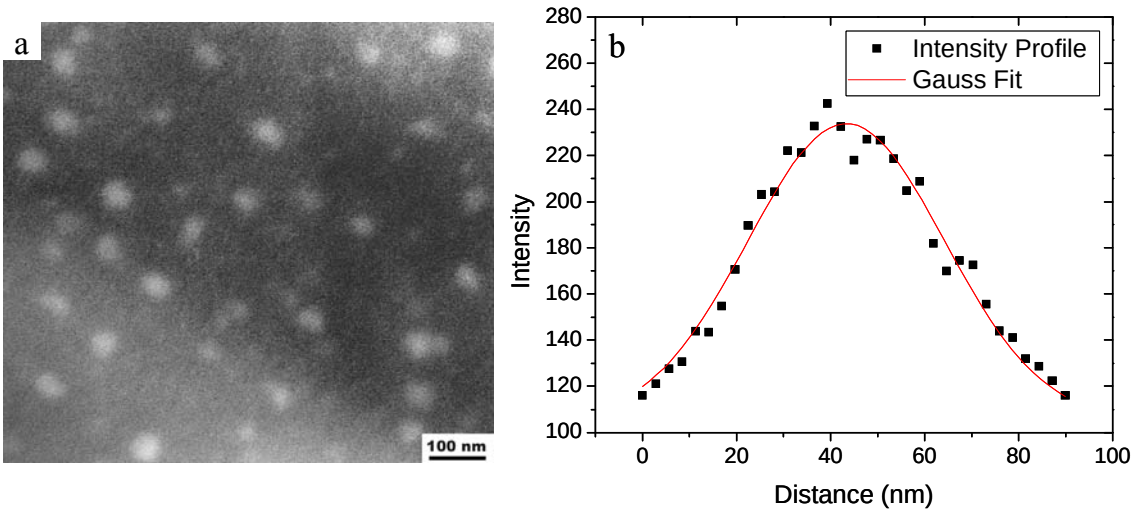

Figure 6.4 a) HAADF STEM image of phosphonium polyurethane showed bright, spherical ion-rich regions dispersed in the dark, hydrocarbon-rich matrix. b) Fitting the intensity profile across an isolated ionic aggregate with a Gaussian function provided the diameter of a STEM feature.

Energy-dispersive X-ray spectroscopy (EDS) was used to determine the elemental composition of ionic aggregates during STEM imaging (Figure 6.5). The spectra were collected by placing a focused electron beam of 0.7 nm diameter on bright and dark regions in the same field of view at high magnification to ensure similar thickness of the two locations. EDS results indicated that the bright, ion-rich region contained more Br and P elements in comparison to the matrix. A small amount of Br, P and O elements were also detected in the dark matrix region. However, a definite conclusion was not made about whether there were any ionic groups dispersed in the matrix exclusively based on the EDS results due to the limited lateral resolution of EDS.

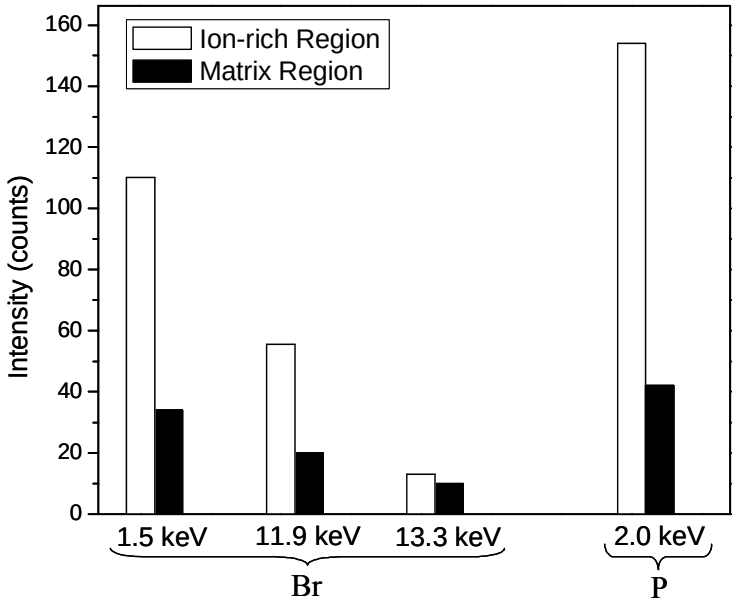

Figure 6.5 Spot EDS intensities taken from phosphonium polyurethane ultrathin films during STEM imaging with a stationary 0.7 nm probe placed on bright and dark regions in the specimen. The quantity of Br and P is greater in the bright ion-rich domains.

To further refine the morphological description of the polyurethanes, the PTMO-HMDI-BD film was stretched to ~600% strain at room temperature using a tensile testing instrument and studied via X-ray scattering in the stretched state. The 2-D wide-angle scattering pattern showed two equatorial scattering peaks at angular positions of 14 nm^{-1} and 17 nm^{-1} (Figure 6.6a), which were the same as the crystalline reflection peaks of PTMO oligomers. Strain-induced crystallization has been observed in various polymers.[43-45] Uniaxial stretching aligned the soft segment of the polymer backbone along the drawing direction, which effectively reduced the entropy of the polymer chain and promoted crystallization of the PTMO segment at room temperature. Furthermore, at high strain of 600%, the intramolecular hydrogen bonding that restricted the mobility of PTMO segments was broken, thereby rendering more freedom for PTMO chain to

reorganize into crystalline structures. Moreover, the 2-D wide-angle scattering pattern revealed weak meridional reflections at 6 nm^{-1} (Figure 6.6b), indicating alignment of the hard segment along the stretching direction. As shown previously in Figure 6.3, this peak at 6 nm^{-1} was absent in the PTMO oligomers. It was attributed to the urethane-urethane spacing along the backbone (Figure 6.6d). The peak position of 6 nm^{-1} corresponded to a real-space distance of 1.05 nm. The intramolecular distance between the two urethane groups was estimated to be 1.15 nm.[46] Stretching also introduced meridional scattering in the 2-D small-angle scattering pattern (Figure 6.6c), indicating that the orientation of the interparticle scattering between the microphase-separated hard domains was parallel to the stretching direction. Compared to the unstretched PTMO-HMDI-BD, the peak position in the stretched film shifted from 0.49 nm^{-1} to 0.35 nm^{-1}, signifying a larger spacing between the microphase-separated domains due to the elongation of PTMO soft segments. Thus, uniaxial stretching altered the morphology in ways that were consistent with the proposed peak assignments. The intermolecular crystalline scattering signified PTMO chains crystallinzing along the stretching direction. The intramolecular scattering from the hard segment also showed the alignment of hard segments along the stretching direction, and the interparticle scattering from the domains indicated that the alignment of the microphase-separated domains was parallel to the stretching direction.

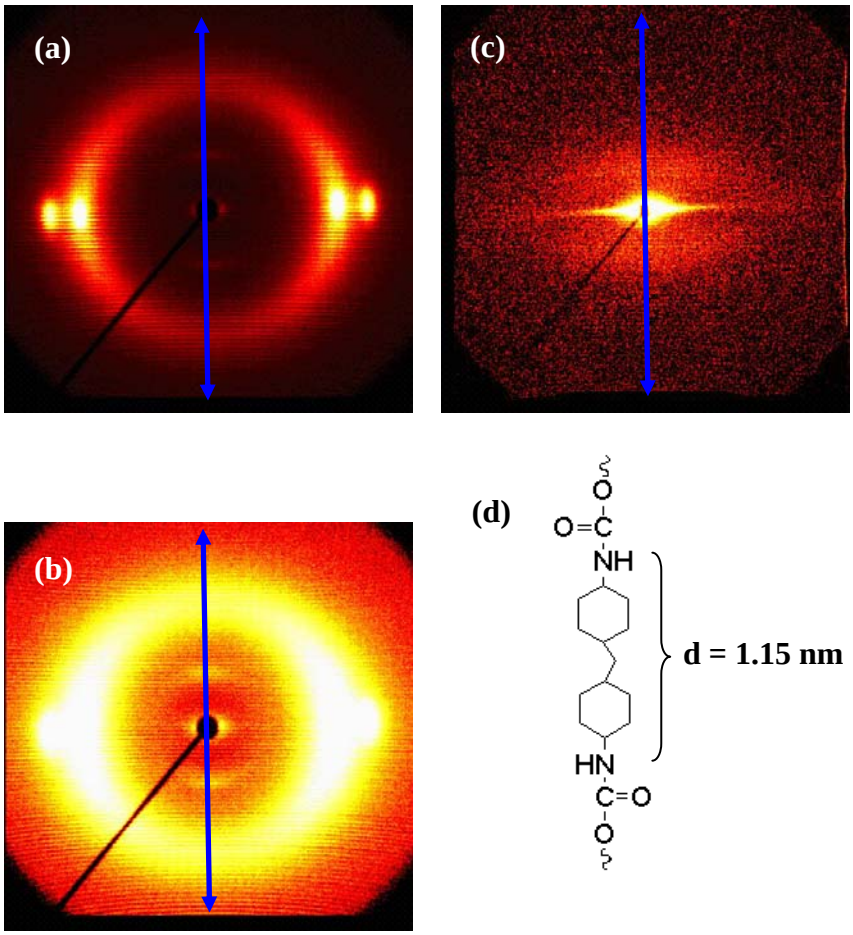

Figure 6.6 2-D X-ray scattering patterns of the stretched PTMO-HMDI-BD films at 600% strain (a) Wide-angle pattern shows two equatorial scattering peaks at angular positions of 14 nm^{-1} and 17 nm^{-1} that correspond to PTMO crystallization. (b) Same wide-angle pattern as (a), but in a different color scale to show the weak meridional reflections at 6 nm^{-1} that correspond to intramolecular scattering from hard segment. (c) Small-angle pattern shows meridional reflections at ~0.35 nm^{-1} that correspond to interparticle scattering from microphase-separated hard domains. The blue arrow indicates the stretching direction. (d) Chemical structure of the urethane segment in PTMO-HMDI-BD.

FT-IR spectroscopy was utilized to observe the extent of hydrogen bonding in both polyurethanes (Figure 6.7). Wilkes et al. demonstrated FT-IR spectroscopy was a simple and efficient means to determine the extent of hydrogen bonding in the carbonyl absorbing region of 1610-1760 cm^{-1} for noncharged polyurethanes.[47] Specifically, they confirmed that there are distinct peaks in the carbonyl region that are attributed to hydrogen-bonding interactions for carbonyl groups. Non-hydrogen-bonded carbonyls have a peak at higher wavenumbers than hydrogen-bonded carbonyls. Furthermore, Wu et al. investigated the extent of hydrogen bonding in Nylon-6,6 in the presence of lithium salts.[48] They determined that the NH peak in the FT-IR spectrum narrows as the extent of hydrogen bonding increased. In the case of PTMO-HMDI-BD and PTMO-HMDI-P+, FT-IR spectroscopy was a very powerful tool to examine the extent of hydrogen bonding. As shown in Figure 6.7, the NH region is distinctly sharper for PTMO-HMDI-BD than PTMO-HMDI-P+. In addition, the carbonyl region of PTMO-HMDI-BD had two peaks, at 1716 cm^{-1} and 1686 cm^{-1}. The peak at 1716 cm^{-1} was attributed to free carbonyl groups, and the peak at 1686 cm^{-1} was attributed to carbonyls that participated in hydrogen bonding. Clearly, a lack of hydrogen bonding was demonstrated for PTMO-HMDI-P+, as evidenced with the absence of a peak in the hydrogen-bond carbonyl region at 1686 cm^{-1}. This demonstrated that the hydrogen-bonding interactions were significantly reduced due to the presence of ionic groups. As a result, ionic interactions were the primary driving force for microphase separation in the phosphonium polyurethanes. Furthermore, this finding supported the tensile property results that are described below.

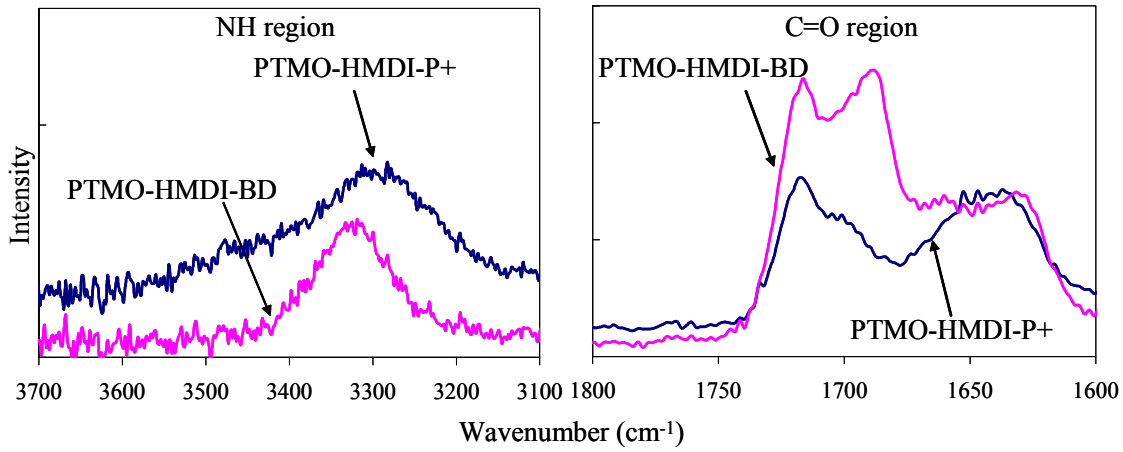

Figure 6.7 FT-IR spectroscopy of NH (left) and C=O (right) region of PTMO-HMDI-BD and PTMO-HMDI-P+.

6.3.5 Tensile Properties: Representative stress-strain curves for both the phosphonium-containing and noncharged polyurethanes are shown in Figure 6.8. The charged and noncharged polyurethanes had comparable maximum elongation, which were 1330 ± 63 % and 1170 ± 180 %, respectively. The tensile stress at break was slightly higher for noncharged polyurethanes (24.0 ± 1.2 MPa) comparing to PTMO-HMDI-P+ polyurethanes (19.2 ± 1.1 MPa). All polyurethanes displayed excellent recovery after elongation. However, the presence of ionic groups disrupted hydrogen bonding and resulted in the slightly lower tensile performance of the phosphonium polyurethanes in comparison to the noncharged polymers. Interestingly, the tensile behavior after ~200 % elongation was quite different as the PTMO-HMDI-BD polyurethane displayed pronounced strain hardening behavior. The strain-induced crystallization was confirmed previously with X-ray scattering (Figure 6.6a), and was due to the recognized strain induced crystallization of PTMO.[29, 49] In addition, during

uniaxial stretching, it was speculated that the intramolecular hydrogen bonding between the ether oxygen in PTMO segments and urethane group was broken and replaced with intermolecular hydrogen bonds,[50] which also increased the number of physical cross-links and resulted in the straining-hardening behavior. In contrast, the presence of disruptive ionic groups prevented an upturn in modulus for the phosphonium polyurethane. Repeated experiments of PTMO-HMDI-P+ polyurethanes resulted in the reproducible behavior as shown in Figure 6.8.

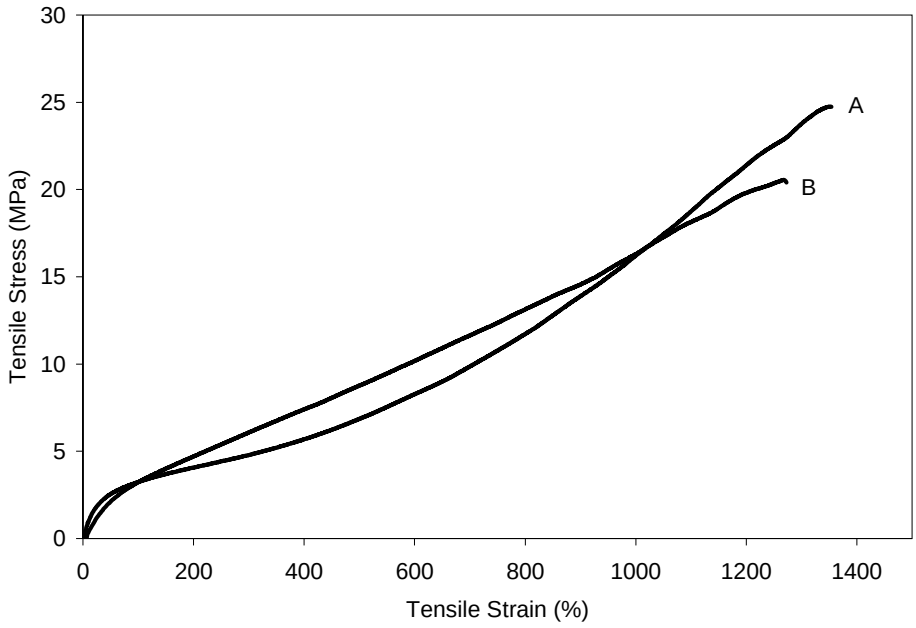

Figure 6.8 Comparison of the stress-strain behavior of linear, segmented, ion-containing polyurethane elastomer compared to the noncharged polyurethane: (A) PTMO-HMDI-BD (B) PTMO-HMDI-P+.

6.4 Conclusion

Novel phosphonium-containing polyurethanes were synthesized using a prepolymer method and characterized using a variety of methods. For comparative purposes, polyurethanes containing 1,4-butanediol as the chain extender were also synthesized. The noncharged PTMO-based polyurethane had hydrogen bonding as evident by FT-IR spectroscopy, while secondary bonding in the charged PTMO-based polyurethanes was dominated by the ionic interactions. Hydrogen-bonding interactions in PTMO-HDMI-BD reduced chain mobility and crystallinity of the PTMO segment. DSC detected crystallization in PTMO-HMDI-P+ with a T_c (-30 °C) and a T_m (14 °C). At room temperature, X-ray scattering of both polyurethanes indicated that they were amorphous with scattering features corresponding to interparticle scattering between microphase-separated hard domains (~ 0.2-0.5 nm^{-1}), intramolecular scattering from hard segments (~ 6 nm^{-1}), and intermolecular amorphous scattering at ~ 14 nm^{-1}. For ion-containing polyurethanes, STEM imaging confirmed the presence of ionic aggregates that were enriched with Br and P, although the observed size of aggregates was surprisingly large, perhaps due to their hygroscopic nature. X-ray scattering on stretched films verified the assignments of scattering peaks and detected strain-induced crystallization. Strain-induced crystallization was also observed in tensile testing, wherein PTMO-HMDI-BD had an upturn in modulus at the high strain region. Both charged and noncharged polyurethanes exhibited excellent elasticity, high strain to break (>1100 %), and high tensile strengths (>19 MPa). A future study will investigate the antimicrobial properties of these novel phosphonium polyurethanes. Furthermore, this type of

phosphonium diol chain extender opens a wide field of potential research in polyurethane ionomers for different applications.

6.5 References

1. Unal, S.; Yilgor, I.; Yilgor, E.; Sheth, J. P.; Wilkes, G. L.; Long, T. E. *Macromolecules* **2004,** 37, (19), 7081-7084.

2. Woods, G., *The ICI polyurethanes book*. John Wiley: New York, 1990.

3. Szycher, M., *Szycher's handbook of polyurethanes*. CRC Press: Boca Raton, 1999.

4. Chattopadhyay, D. K.; Raju, K. V. S. N. *Progress in Polymer Science* **2007,** 32, (3), 352-418.

5. Petrovic, Z. S.; Ferguson, J. *Prog. Polym. Sci.* **1991,** 16, (5), 695-836.

6. Hepburn, C., *Polyurethane elastomers*. 2nd ed.; Elsevier Applied Science: London, 1992.

7. Thomson, J. B.; Lightfoot, P.; Bruce, P. G. *Solid State Ionics* **1996,** 85, (1-4), 203-208.

8. *The polyurethanes book*. J. Wiley: New York, 2002.

9. Dickinson, R. B.; Nagel, J. A.; Proctor, R. A.; Cooper, S. L. *Journal of Biomedical Materials Research* **1997,** 36, (2), 152-162.

10. Culkin, D. A.; Jeong, W. H.; Csihony, S.; Gomez, E. D.; Balsara, N. R.; Hedrick, J. L.; Waymouth, R. M. *Angewandte Chemie-International Edition* **2007,** 46, (15), 2627-2630.

11. Krol, P.; Krol, B.; Subocz, L.; Andruszkiewicz, P. *Colloid and Polymer Science* **2006,** 285, (2), 177-183.

12. Polizos, G.; Georgoussis, G.; Kyritsis, A.; Shilov, V. V.; Shevchenko, V. V.; Gomza, Y. P.; Nesin, S. D.; Klimenko, N. S.; Wartewig, S.; Pissis, P. *Polymer International* **2000,** 49, (9), 987-992.

13. Shilov, V. V.; Shevchenko, V. V.; Pissis, P.; Kyritsis, A.; Georgoussis, G.; Gomza, Y. P.; Nesin, S. D.; Klimenko, N. S. *Molecular Crystals and Liquid Crystals* **2001,** 361, 269-274.

14. Vatalis, A. S.; Kanapitsas, A.; Delides, C. G.; Viras, K.; Pissis, P. *Journal of Applied Polymer Science* **2001,** 80, (7), 1071-1084.

15. Reiff, H.; Dieterich, D., Urethane-based dispersions. In *Ionomers: Synthesis, Structure, Properties, and Applications*, Tant, M. R.; Mauritz, K. A.; Wilkes, G. L., Eds. Blackie Academic and Professional: London, 1997; pp 444-501.

16. Dieterich, D.; Keberle, W.; Witt, H. *Angew. Chem., Int. Ed.* **1970,** 9, (1), 40-50.

17. Chen, S. A.; Hsu, J. S. *Polymer* **1993,** 34, (13), 2769-2775.

18. Chen, S. A.; Hsu, J. S. *Polymer* **1993,** 34, (13), 2776-2782.

19. Ding, Y. S.; Register, R. A.; Yang, C. Z.; Cooper, S. L. *Polymer* **1989,** 30, (7), 1204-1212.

20. Register, R. A.; Cooper, S. L. *Abstracts of Papers of the American Chemical Society* **1989,** 197, 203-POLY.

21. Register, R. A.; Pruckmayr, G.; Cooper, S. L. *Macromolecules* **1990,** 23, (11), 3023-3026.

22. Register, R. A.; Yu, X. H.; Cooper, S. L. *Polymer Bulletin* **1989,** 22, (5-6), 565-571.

23. Yang, C. Z.; Grasel, T. G.; Bell, J. L.; Register, R. A.; Cooper, S. L. *Journal of Polymer Science Part B-Polymer Physics* **1991,** 29, (5), 581-588.

24. Hickner, M. A.; Ghassemi, H.; Kim, Y. S.; Einsla, B. R.; McGrath, J. E. *Chem. Rev.* **2004,** 104, (10), 4587-4611.

25. Lindsell, W. E.; Radha, K.; Soutar, I.; Stewart, M. J. *Polymer* **1990,** 31, (7), 1374-1378.

26. Mather, B. D.; Baker, M. B.; Beyer, F. L.; Green, M. D.; Berg, M. A. G.; Long, T. E. *Macromolecules* **2007,** 40, 4396-4398.

27. Heiney, P. A. *Comm Powder Diffr Newsletter* **2005,** 32, 9-11.

28. Hu, C. B.; Ward, R. S.; Schneider, N. S. *Journal of Applied Polymer Science* **1982,** 27, (6), 2167-2177.

29. Gomez, E. D.; Das, J.; Chakraborty, A. K.; Pople, J. A.; Balsara, N. P. *Macromolecules* **2006,** 39, (14), 4848-4859.

30. Christenson, C. P.; Harthcock, M. A.; Meadows, M. D.; Spell, H. L.; Howard, W. L.; Creswick, M. W.; Guerra, R. E.; Turner, R. B. *Journal of Polymer Science Part B-Polymer Physics* **1986,** 24, (7), 1401-1439.

31. Fetters, L. J.; Lohse, D. J.; Graessley, W. W. *Journal of Polymer Science Part B-Polymer Physics* **1999,** 37, (10), 1023-1033.

32. Llorens, J.; Rude, E.; Marcos, R. M. *Journal of Polymer Science Part B-Polymer Physics* **2000,** 38, (11), 1539-1546.

33. Wang, D. H.; Shen, Z. H.; Guo, M. M.; Cheng, S. Z. D.; Harris, F. W. *Macromolecules* **2007,** 40, (4), 889-900.

34. Sun, Y.; Jeng, U.; Huang, Y.; Liang, K.; Lin, T.; Tsao, C. *Physica B* **2006,** 385, 650-652.

35. Tadokoro, H. *J. Poly. Sci., Part C* **1966,** 15, 1-15.

36. Aneja, A.; Wilkes, G. L. *Polymer* **2003,** 44, (23), 7221-7228.

37. Klinedinst, D. B.; Yilgor, E.; Yilgor, I.; Beyer, F. L.; Wilkes, G. L. *Polymer* **2005,** 46, (23), 10191-10201.

38. O'Sickey, M. J.; Lawrey, B. D.; Wilkes, G. L. *Polymer* **2002,** 43, (26), 7399-7408.

39. Sheth, J. P.; Klinedinst, D. B.; Wilkes, G. L.; Iskender, Y.; Yilgor, E. *Polymer* **2005,** 46, (18), 7317-7322.

40. Sheth, J. P.; Unal, S.; Yilgor, E.; Yilgor, I.; Beyer, F. L.; Long, T. E.; Wilkes, G. L. *Polymer* **2005,** 46, (23), 10180-10190.

41. Benetatos, N. M.; Chan, C. D.; Winey, K. I. *Macromolecules* **2007,** 40, (4), 1081-1088.

42. Zhou, N. C.; Chan, C. D.; Winey, K. I. *Macromolecules* **2008,** 41, (16), 6134-6140.

43. Martins, C. I.; Cakmak, M. *Polymer* **2007,** 48, (7), 2109-2123.

44. Bartczak, Z.; Kozanecki, A. *Polymer* **2005,** 46, (19), 8210-8221.

45. Klimov, E.; Hoffmann, G. G.; Gumenny, A.; Siesler, H. W. *Macromolecular Rapid Communications* **2005,** 26, (13), 1093-1098.

46. The distance is calculated based on the size of cyclohexane (0.45 nm) and the carbon-carbon bond length of 0.145 nm with bond angle of 120^{o}.

47. Yilgor, I.; Yilgor, E.; Guler, I. G.; Ward, T. C.; Wilkes, G. L. *Polymer* **2006,** 47, 4105-4114.

48. Wu, Y.; Xu, Y.; Wang, D.; Zhao, Y.; Weng, S.; Xu, D.; Wu, J. *J. Appl. Polym. Sci.* **2004,** 91, 2869-2875.

49. Feng, Y.; Weiss, R. A.; Han, C. C. *Macromolecules* **1996,** 29, (11), 3925-3930.

50. Myung, D.; Koh, W. U.; Ko, J. M.; Hu, Y.; Carrasco, M.; Noolandi, J.; Ta, C. N.; Frank, C. W. *Polymer* **2007,** 48, (18), 5376-5387.

Chapter 7

Conclusions and Future Work

7.1 Conclusions

Ionomers exhibit exceptional chemical and physical properties due to the presence of ionic groups. Although ionomers have found a remarkable range of commercial applications, understanding the fundamental structure-property relationships in ionomers has proven to be a challenging problem. The morphology and corresponding properties of ionomers are highly sensitive to sample preparation conditions and thermal history, which complicate the interpretation of the results. As a result, separate studies of the structure or property on the same class of ionomers prepared by different groups might lead to inconsistent results. It is highly desirable to combine different techniques to study the same ionomers in order to elucidate the fundamental principles that control the structures and properties of ionomers. This dissertation conveys a new level of understanding regarding the multi-scale morphologies and dynamics of ionomers by employing multiple techniques to study the same ionomers, and establish the correlation between structure, dynamics, and ion conduction through extensive collaborations.

In Chapter 2, we explore the morphology of Cu-neutralized poly(styrene-ran-methacrylic acid) (SMAA-Cu) ionomers, including the local structure and composition of the ionic aggregates, as a function of acid content and neutralization level. X-ray scattering and scanning transmission electron microscopy (STEM) results showed that the sizes of the ionic aggregates in SMAA-Cu ($<2R_1>$ = 1.12 nm) are independent of the

acid content and neutralization level. The number density of ionic aggregates increased slightly with acid content and neutralization level, but the increase was significantly less than expected for aggregates of fixed composition. Electron spin resonance (ESR) spectra of Cu(II) detected three distinct cation sites whose relative amounts changed with acid content. These results combined to indicate that the ionic aggregates contain non-ionic species and that the aggregate compositions become more ionic with increasing acid content and neutralization level. The strength of ionic association and ion mobility are strongly related to the local structure and composition of ionic aggregates, such that these findings provide valuable information for the understanding of ion diffusion and polymer dynamics in these ionomers.

In Chapter 3, the morphology and dynamics of sulfonated polystyrene acid copolymers and ionomers are explored. X-ray scattering shows that SPS copolymers form acid aggregates, with peak intensity increasing with sulfonation level. Sulfonation increases the dielectric relaxation strength of the α process, due to the introduction of -SO_3H dipoles. In addition, the hydrogen bonding or aggregation of -SO_3H significantly slows down the dynamics. The size of the ionic aggregates ($<2R_1> = 1.62$ nm) is almost independent of acid content, neutralization level, and cation. The results from both chapter 2 and 3 suggest that the size of ionic aggregates in these strongly segregating ionomers is mainly controlled by polymer backbone structure and acid type. Increasing the neutralization level increases the distance of closest approach between aggregates ($2R_{CA}$). This is because the ionic aggregates in partially neutralized SPS ionomers contain unneutralized acid as the neutralization level increases and more zinc sulfonate groups are incorporated into the aggregates. Thus, the stronger electrostatic interactions

between the ionic groups enhanced the restriction in the mobility of chains around the aggregates. A secondary relaxation (α_2 process) appears at lower frequency than the segmental relaxation in SPS-Zn (α process), which is attributed the relaxation of polystyrene segment in the region of restricted region and local motion of ionic groups inside the aggregates. The relaxation strength of the α_2 process increases with neutralization level, while the strength of the α process shows the opposite trend. These findings correlate well with the morphological results.

Chapter 4 and Chapter 5 investigate the morphology of Li, Na, and Cs-neutralized polyester ionomers with well-defined PEO spacer lengths between sulfonated phthalates over a wide range scale. The room-temperature morphology of PEO-based ionomers is explored in Chapter 4. As the PEO spacer lengths are increased the PEO segments crystallize, as evidenced by multiple crystal reflections that are identical to those of pure poly(ethylene glycol) oligomers. This crystallization also produces multiple small-angle peaks, which correspond to the well-defined thickness of PEO crystallites. The ionic groups are excluded from the crystallites and into the amorphous domain in the semicrystalline PEO ionomers. By normalizing the X-ray scattering intensity of PEO-based ionomers with 0% and 100% sulfonation, the scattering contribution from PEO and phthalates can be subtracted, which enables analysis the scattering from ions and comparison with *ab inito* calculations. Detailed analysis of the subtracted X-ray scattering intensity from these ionomers reveals a variety of ionic states that are highly dependent on the cation size. The states of ionic groups change from a majority of isolated ion pairs to aggregated structures as the cation size decreases from Cs to Li.

Chapter 5 focuses on the states of ionic association in PEO-based ionomers as a function of temperature. As the temperature increases, an X-ray scattering peak at q = 2-3 nm^{-1} gradually appears in Na and Cs-neutralized ionomers, while Li-neutralized ionomers exhibit a similar ionomer peak across the entire temperature range studied (25 ^{o}C - 150 ^{o}C). For all ionomers, the peak intensity increases with increasing temperature. The morphological transitions are thermoreversible. Detailed analysis of the positions of the ionomer and amorphous peaks reveals that the formation of the peak cannot be attributed solely to the enhanced contrast between ionic aggregates and PEO matrix, but rather is consistent with the reorganization of isolated ionic pairs into aggregates. Cs-neutralized ionomers showed the most dramatic transitions due to the weakest ionic association strength among the three different cations. The increasing extent of ionic aggregation with increasing temperature is caused by the decreased ability of PEO to solvate ions.

Chapter 6 elucidates the effect of ionic groups on the hydrogen-bonding interactions in phosphonium-containing polyurethane using a variety of techniques. In comparison to the non-charged polyurethane, which has hydrogen-bonding interactions, the secondary bonding in phosphonium-containing polyurethanes is dominated by the ionic interaction. Both ionic and neutral materials exhibit microphase separation of hard domains as shown by the X-ray scattering. However, the origin of microphase in the charged polyurethane mainly arises from ionic interactions instead of hydrogen bonding. HAADF STEM images of the charged polyurethane combined with energy dispersive X-ray spectroscopy confirmed the presence of ionic aggregates that were enriched with Br and P. In addition to the microphase separation peak, X-ray scattering also exhibited two

additional scattering features, corresponding to intramolecular scattering from hard segments (~ 6 nm^{-1}) and amorphous halo at ~ 14 nm^{-1}, respectively. X-ray scattering on stretched films verified the assignments of these scattering peaks and detected strain-induced crystallization.

7.2 Future Work

7.1.1 Size and Shape of Ionic Aggregates in PEO-based Ionomers: The size and shape of ionic aggregates in PEO-based ionomers remains unknown. X-ray scattering shows that ionic aggregates form in PEO-Na or PEO-Cs ionomers at elevated temperature. Although Cs would provide enough contrast in HAADF STEM mode, the low glass transition temperature prevents the direct imaging of this material at high temperatures in STEM. As PEO-Li ionomers exhibited well-defined ionic aggregation peak at room temperature, it is possible to apply direct imaging method to this materials to elucidate the size and shape of ionic aggregates. However, HAADF imaging is based on the Z-contrast and Li will not have enough contrast in HAADF STEM mode. Analytical electron microscopy techniques provide a promising way to resolve this issue. Energy-filtered transmission electron microscopy (EFTEM) has proven to be a powerful analytical method in the past decade. In EFTEM, post column energy filter in combination with TEM can provide the capability of detecting nanometer or even sub-nanometer scale features.[1] However, the attainable spatial resolution is affected by the specimen thickness, energy, and shape of the ionization edge, collection angle, and inherent instrumental resolution.[1] Gomez *et al*. recently demonstrated the imaging of amorphous Li-containing domains in block copolymer using EFTEM, but the size of the

Li-containing domains is on the scale of 10 nm.[2] Imaging the Li-containing ionic aggregate of 1 nm in diameter in PEO-based ionomers will be particularly challenging, as the feature size becomes convoluted by the spatial resolution, which caused broadening of the feature as well as reduced contrast. Using electron energy loss spectroscopy (EELS) in combination with STEM imaging will improve the resolution. The spatial resolution in STEM-EELS is mainly governed by focused beam size and the beam broadening in the specimen, thus mapping mode in STEM-EELS would provide similar resolution as the point/line analysis mode.[3] Several researchers have demonstrated sub-nanometer scale imaging in inorganic materials using STEM-EELS.[3, 4] Using STEM-EELS to determine the size and shape of ionic aggregates in PEO-Li ionomers would help to determine appropriate structural model to facilitate further interpretation of the X-ray scattering data.

7.1.2 Origin of Dielectric Relaxations in Ionomers: The dielectric relaxation spectroscopy reveals rich information about the dynamics of bound dipoles and charge carriers over a wide frequency range. Depending on the frequency or temperature, the complex dielectric loss originates from different processes: (1) rotational diffusion of dipoles, (2) translational diffusion of mobile charge carriers, and (3) separation of charges at interfaces.[5] In Chapter 3, we focused on the processes at relatively high frequency (α and α_2) in SPS ionomers. The origins of lower-frequency processes remain unclear, partially due to the complexity of the morphology and high T_g. Several relaxations could occur at lower frequency, including associating and disassociating of hydrogen-bonded sulfonic acids, ion-hopping process, Maxwell/Wagner/Sillars polarization, and electrode polarization. Analysis will continue in Professor Runt's group to elucidate the origins of

these processes, including analysis of the temperature dependence of relaxation frequency and comparison of the dielectric relaxation with dynamic mechanical analysis results. Temperature dependent FTIR spectroscopy can be employed to study the hydrogen-bonding interactions in SPS acid and partially neutralized ionomers.

The combination of STEM, X-ray scattering and DRS can be applied to other ionomers systems as well. Poly(ethylene-ran-methacrylic acid) (EMAA) based ionomer have been extensively studied to understand its morphology and mechanical properties. It is found that EMAA ionomers exhibit multiple phases, including semicrystalline polyethylene lamella, amorphous polyethylene, and ionic aggregates.[6] When the acid content is high enough, the ionomers become amorphous, which eliminates the complexity associated with crystalline phase. EMAA have much lower T_g (< 50 ^oC)[7] than SPS, thus it is possible to explore a wider temperature range above T_g before reaching thermal degradation temperature. This is especially helpful for the investigation of the higher temperature or lower frequency relaxation processes. Kutsumizu *et al.* reported the dielectric studies of non-crystalline EMAA random ionomers containing 13.3 mol% acids and neutralized with Na and Zn.[8] The ionomers were prepared by melt reaction of the acid polymer with sodium carbonate or zinc oxide. Their analysis of the dielectric constant using Onsager equation showed that most of the COONa groups are located in the ionic clusters.[8] However, the analysis is highly dependent on the assignments of various relaxation processes, and the authors did not provide adequate evidence to support their assignments.[8] Our group recently elucidated the morphology of EMAA ionomers with precisely spaced acids pendant to the polymer backbone using both X-ray scattering and STEM.[9] One of these precise EMAA ionomers exhibits

ordered ionic aggregates with cubic lattice instead of liquid-like packing.[9] It is expected these ionomers would exhibit interesting dielectric properties and ordered structures would greatly facilitate the interpretation of various dielectric relaxation processes.

7.1.3 Effect of Water Content on the Morphology of Ionomers: Many researchers have reported the effect of water content in the structure and dynamics of hydrocarbon-based ionomers using X-ray scattering, ESR, and extended X-ray absorption fine structure (EXAFS).[10-14] It is expected that water will preferentially interact with the ionic groups rather than the hydrocarbon matrix. However, the effect of water content on the morphology is complicated by the presence of isolated ionic groups in the matrix, the possible reorganization of hydrated ionic groups, and the slow water transport through mostly non-polar matrix that could result in incomplete hydration. Yarusso and Cooper found that increasing water content in Zn-SPS shifted the ionomer peak to lower q and sharpened the peak intensity.[13] The interpretation of the scattering data with the modified hard-sphere model showed that the increase in the volume of ionic aggregates is larger than the volume of water added.[13] As a result, they proposed that the ionic groups that were originally isolated in the matrix aggregated upon hydration.[13] However, this is surprising considering that the migration of ions requires motion of polystyrene segments and T_g of rigid polystyrene matrix is well above room temperature. Williams *et al.* observed different water uptake behaviors in carboxy-telechelic ionomers with different distribution of polymer chain length between the ionic groups.[10] The ionomers with narrower chain length distribution between ionic groups showed much slower water uptake compared to ionomers with broader chain length distribution.[10] It was proposed that ionomers with more random chain length distribution between ionic groups contain

more isolated ions in the matrix, which facilitate water uptake.[10] This is also supported by much higher level of electron density fluctuation in these ionomers from X-ray scattering.[10]

In Chapter 3, we have reported the morphologies of SPS acid copolymers and SPS ionomers at room temperature. It is desirable to study the effect of water content on the morphologies of these ionomers, and how the water uptake behaviors change with acid content, neutralization level, and cation type. The change in the scattering patterns and water uptake behaviors would provide qualitative information about the extent of ionic aggregation, i.e. percentage of ionic groups in the aggregates. The results can also be correlated with the dielectric properties. In addition, as the small-angle upturn has been attributed to the long-range inhomogeneities, including unneutralized acids, extra neutralizing agents, and isolated ion pairs distributed in the polymer matrix,[15] the effect of water content on the small-angle upturn would facilitate the interpretation of morphological changes as well.

7.3 References

1. Grogger, W.; Schaffer, B.; Krishnan, K. M.; Hofer, F. *Ultramicroscopy* **2003,** 96, (3-4), 481-489.

2. Gomez, E. D.; Panday, A.; Feng, E. H.; Chen, V.; Stone, G. M.; Minor, A. M.; Kisielowski, C.; Downing, K. H.; Borodin, O.; Smith, G. D.; Balsara, N. P. *Nano Lett.* **2009,** 9, (3), 1212-1216.

3. Watanabe, M.; Williams, D. B.; Tomokiyo, Y. *Micron* **2003,** 34, (3-5), 173-183.

4. Browning, N. D.; Wallis, D. J.; Nellist, P. D.; Pennycook, S. J. *Micron* **1997,** 28, (5), 333-348.

5. Kremer, F.; Schönhals, A.; Eds., *Broadband Dielectric Spectroscopy*. Springer-Verlag: Heidelberg 2003.

6. Wakabayashi, K.; Register, R. A. *Macromolecules* **2006,** 39, (3), 1079-1086.

7. Baughman, T. W.; Chan, C. D.; Winey, K. I.; Wagener, K. B. *Macromolecules* **2007,** 40, (18), 6564-6571.

8. Kutsumizu, S.; Tadano, K.; Matsuda, Y.; Goto, M.; Tachino, H.; Hara, H.; Hirasawa, E.; Tagawa, H.; Muroga, Y.; Yano, S. *Macromolecules* **2000,** 33, (24), 9044-9053.

9. Seitz, M. E.; Chan, C. D.; Opper, K. L.; Baughman, T. W.; Wagener, K. B.; Winey, K. I. *J. Am. Chem. Soc.* **2010,** In Press.

10. Williams, C. E.; Russell, T. P.; Jerome, R.; Horrion, J. *Macromolecules* **1986,** 19, (11), 2877-2884.

11. Welty, A.; Ooi, S.; Grady, B. P. *Macromolecules* **1999,** 32, (9), 2989-2995.

12. Tsujita, Y.; Yasuda, M.; Kinoshita, T.; Takizawa, A.; Yoshimizu, H.; Davies, G. R. *J. Polym. Sci., Part B: Polym. Phys.* **2002,** 40, (9), 831-839.

13. Yarusso, D. J.; Cooper, S. L. *Polymer* **1985,** 26, (3), 371-378.

14. Kutsumizu, S.; Schlick, S. *J. Mol. Struct.* **2005,** 739, (1-3), 191-198.

15. Li, Y. J.; Peiffer, D. G.; Chu, B. *Macromolecules* **1993,** 26, (15), 4006-4012.

Appendix A: Supporting Information for Chapter 2

Electron spin resonance (ESR) spectra of Cu(II)-neutralized poly(styrene-*co*-methacrylic acid) ionomers at 100% neutralization (SMAA-100Cu) with different acid contents are shown in Figure A.1. All spectra consist of rather broad lines and show a site with $A_{//}$=155G, very close to the major site (site 2) in SMAA-50Cu. Due to the limited resolution, it is impossible to determine whether there are different sites present or not. However, the spectra of SMAA-100Cu suggest the formation of more ordered structures at 13.3 mol% compared to SMAA-100Cu with lower acid contents.

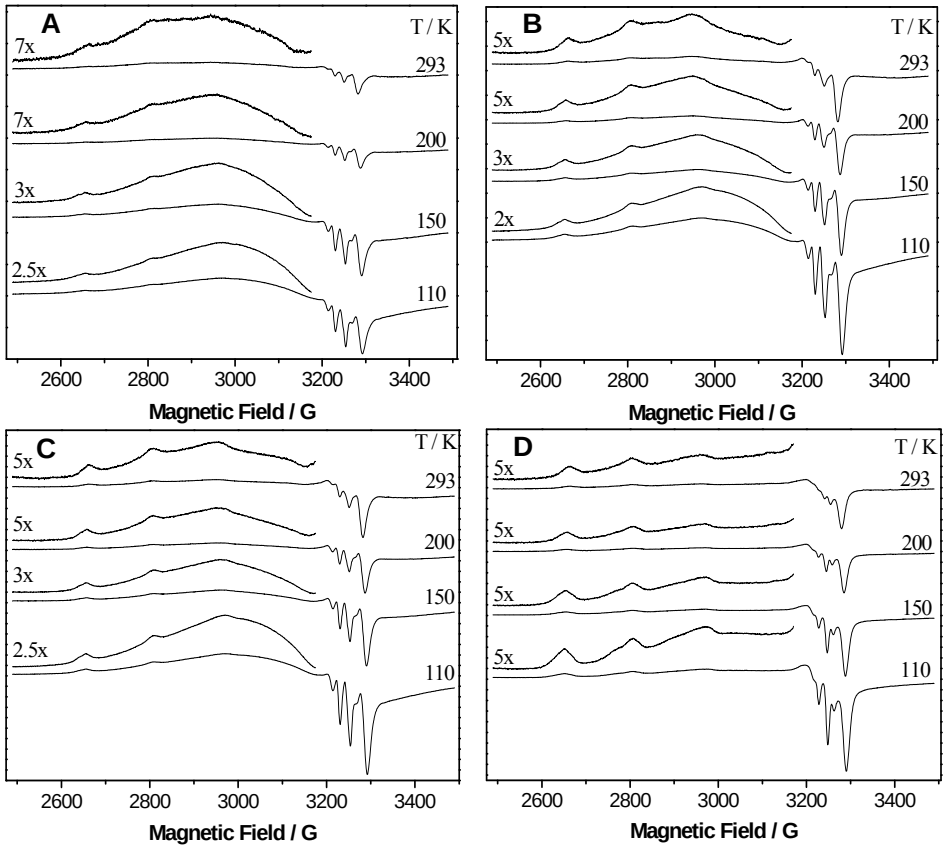

Figure A.1 X-band ESR spectra of SMAA-100Cu as a function of temperature. Vertically expanded portions are shown. The mol % acid is 4.1 (A), 5.8 (B). 8.3 (C), and 13.3 (D).

Appendix B: Supporting Information for Chapter 3

Figure B.1 and Figure B.2 display the X-ray scattering intensity vs. scattering vector q of SPS*x*-*y*Na and SPS*x*-*y*Cs, respectively. The ionomer peak intensity increases with increasing sulfonation level and the peak position shifts slightly to higher angle, indicating smaller inter-aggregate distance.

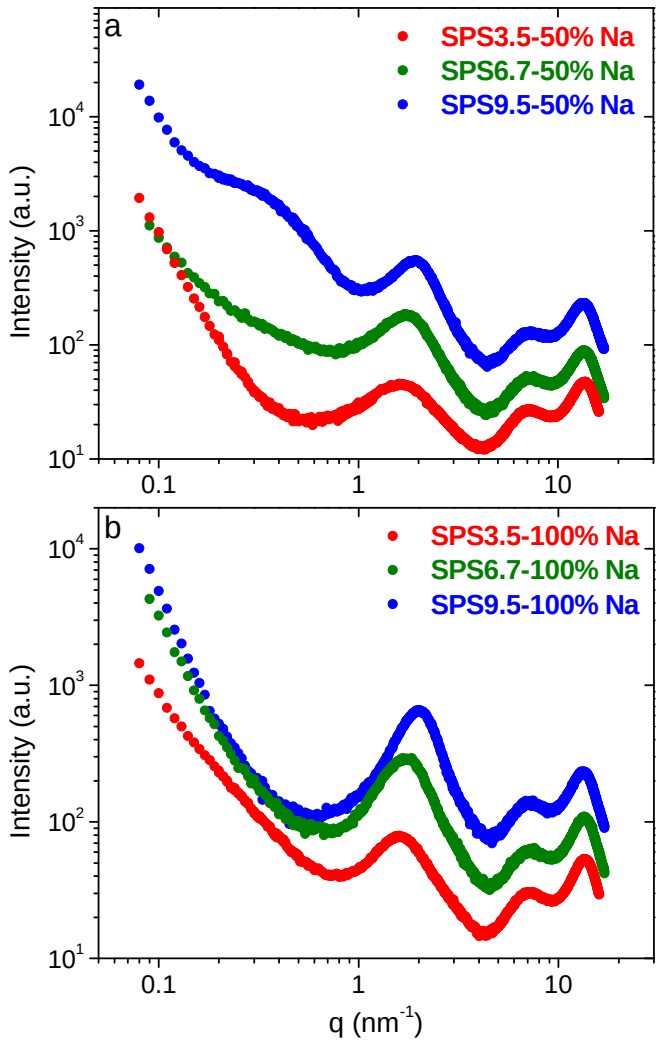

Figure B.1 X-ray scattering intensity vs. scattering vector q of SPS*x*-*y*Na with different sulfonation levels (x = 3.5%, 6.7%, and 9.5%): a) y = 50%; b) y = 100%. The scattering data were vertically shifted for clarity.

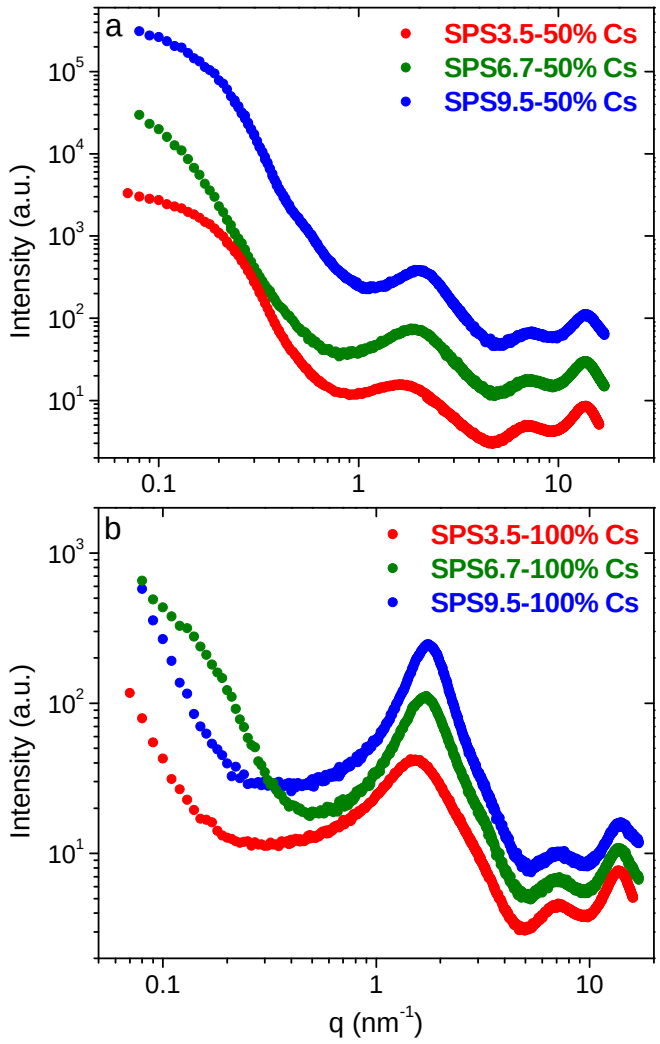

Figure B.2 X-ray scattering intensity vs. scattering vector q of SPS*x*-*y*Cs with different sulfonation levels (x = 3.5%, 6.7%, and 9.5%): a) y = 50%; b) y = 100%. The scattering data were vertically shifted for clarity.

Figure B.3a displays the $2R_1$ and $2R_{CA}$ values as a function of sulfonation level for SPS*x*-*y*M (M = Na and Cs). All ionomers exhibit similar size ($2R_1$) that is independent of cation type, acid content, and neutralization level. The $2R_{CA}$ value decreases slightly with increasing acid content from 3.5% to 9.5%. Figure B.3b shows that N_p increases with increasing sulfonation level.

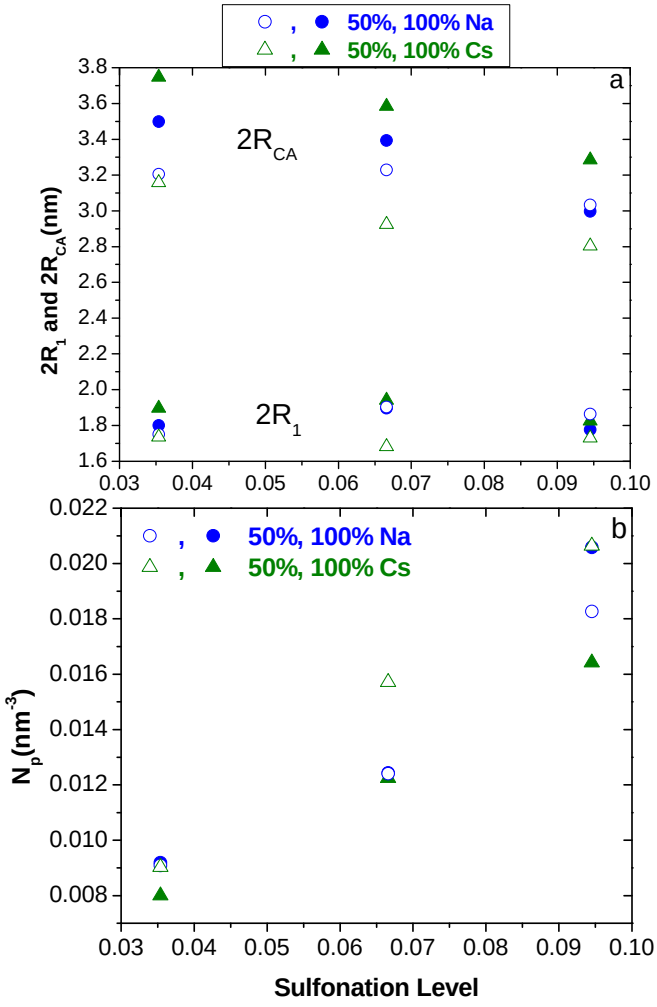

Figure B.3 a) R_1 and R_{CA} determined by X-ray scattering as a function of sulfonation for different cations: ○,● Na; Δ,▲ Cs at 50% (open symbols) and 100% (close symbols) neutralization levels. b) The number density of the ionic aggregate (N_p) as a function of sulfonation.

Appendix C: Supporting Information for Chapter 5

This supplement includes the variable-temperature X-ray scattering of PEO600-yNa (y = 0% and 100%) collected at the Advanced Photon Source at Argonne National Laboratory to a lower angle. In addition, this supplement also presents variable-temperature X-ray scattering from PEO*x*-100%M (x = 400 and 1100, M = Li, Na, and Cs) and X-ray scattering profiles of PEO*x*-100%Li and PEO*x*-100%Na at 150 ^{o}C fitted with Kinning-Thomas model and Debye-Percus-Yevick model.

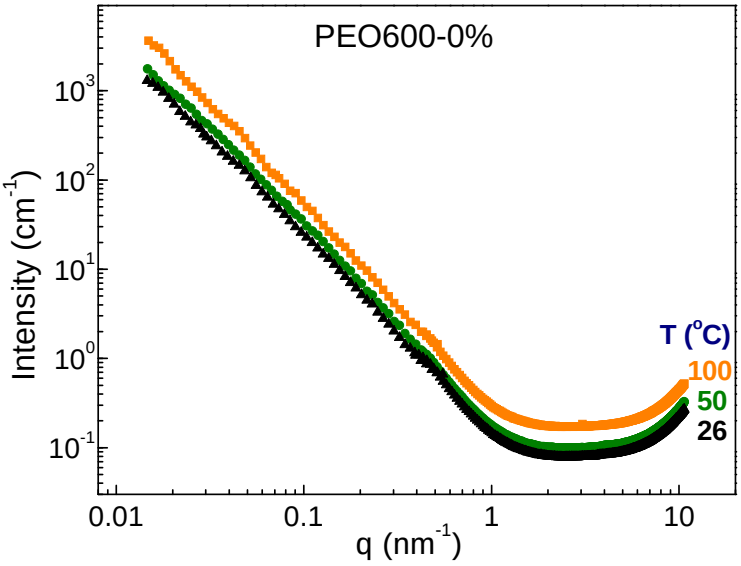

Figure C.1 Ultra-small angle and small angle X-ray scattering data of PEO600-0% as a function of temperature.

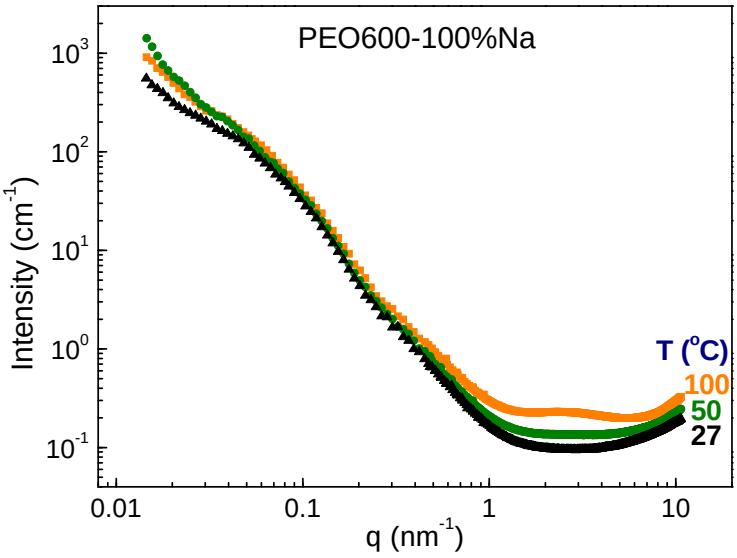

Figure C.2 Ultra-small angle and small angle X-ray scattering data of PEO600-100%Na as a function of temperature. An ionomer peak (q ~ 3 nm^{-1}) appears at 100 °C.

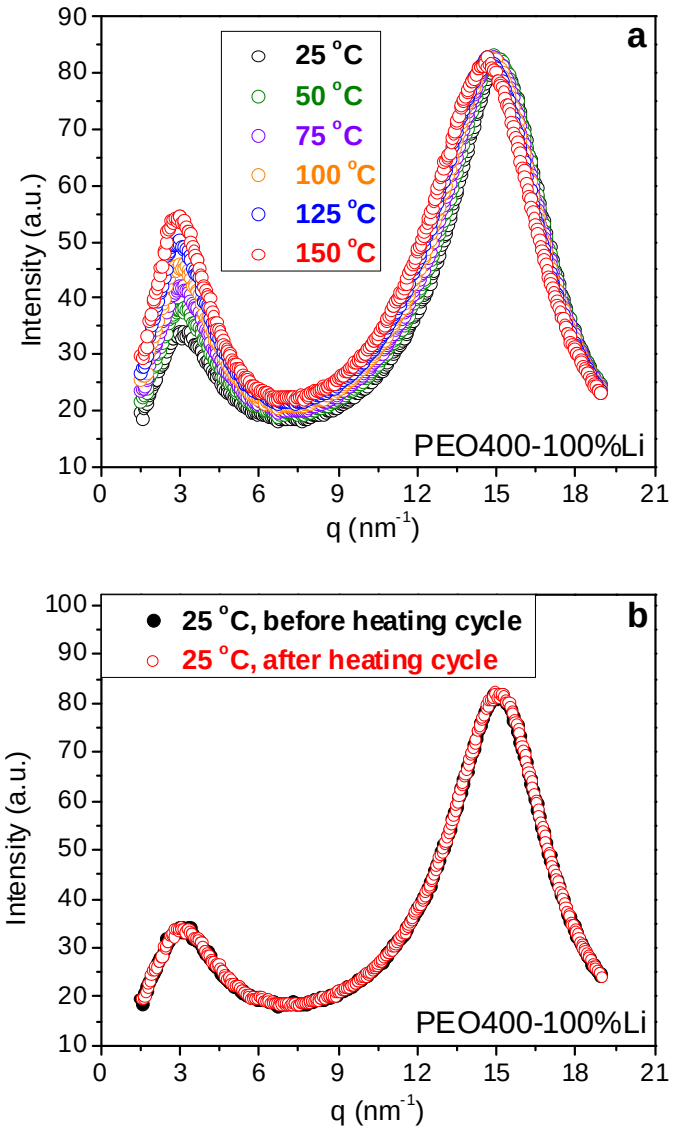

Figure C.3 a) X-ray scattering data of PEO400-100%Li as a function of temperature. The intensity of the ionomer peak increases with temperature. b) The morphology is thermally reversible, as shown by the identical scattering patterns before and after heating.

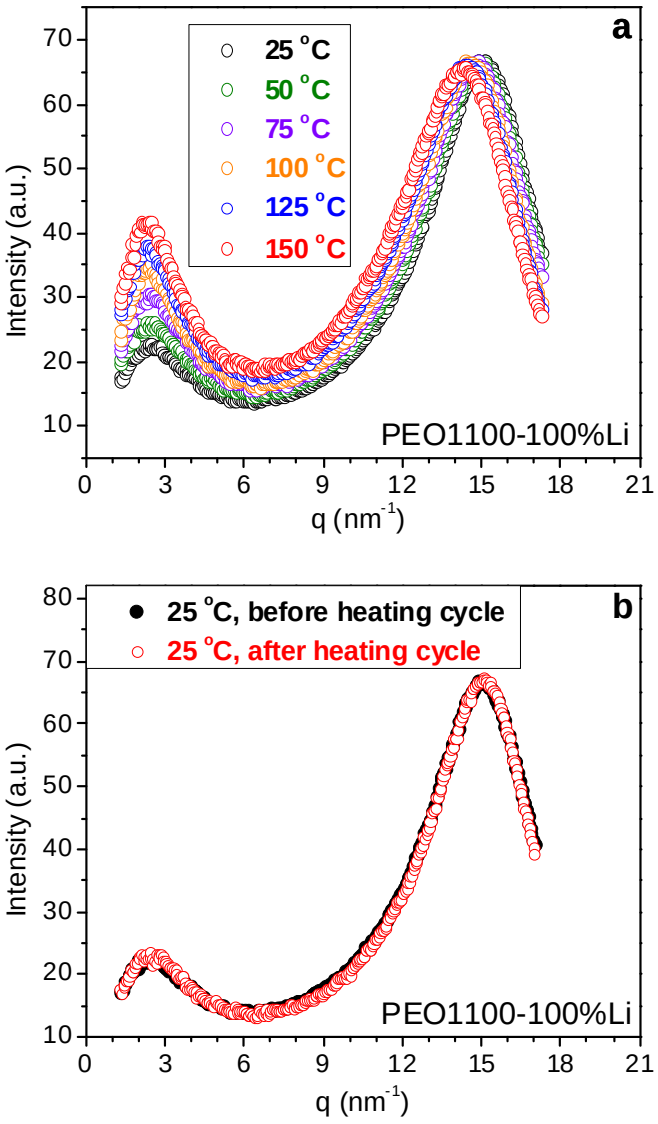

Figure C.4 a) X-ray scattering data of PEO1100-100%Li as a function of temperature. The intensity of the ionomer peak increases with temperature. b) The morphology is thermally reversible, as shown by the identical scattering patterns before and after heating. While PEO1100-100%Li can be semicrystalline at room temperature, depending on the thermal history, this sample is amorphous.

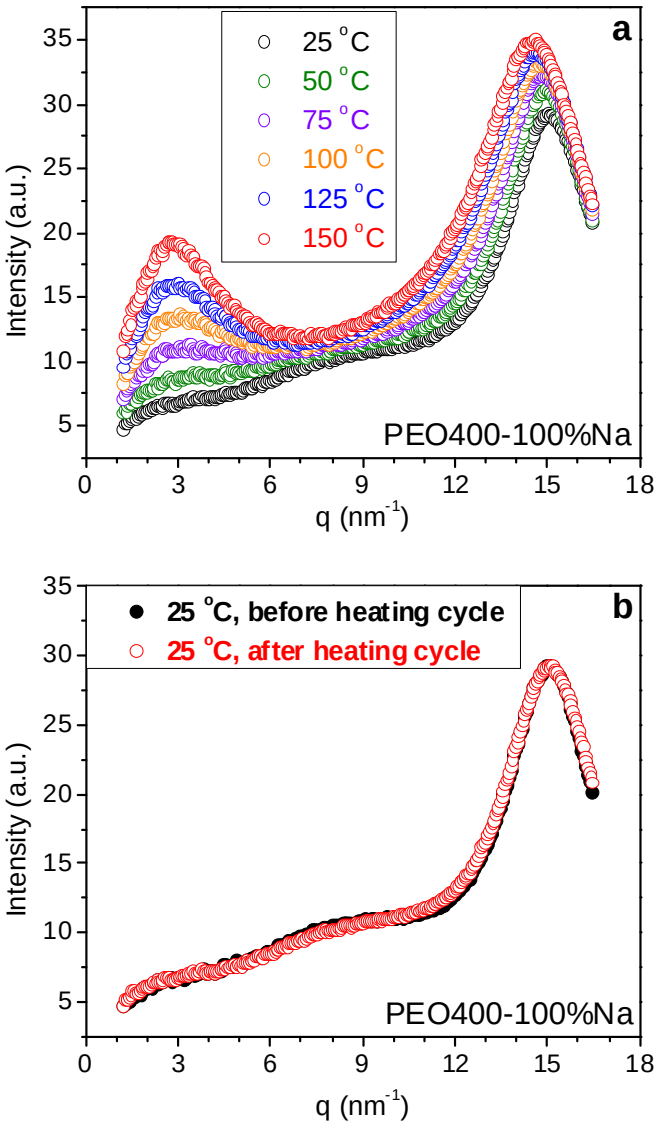

Figure C.5 a) X-ray scattering data of PEO400-100%Na as a function of temperature. An ionomer peak gradually appears as the temperature increases, suggesting reorganization of ionic groups into aggregates. b) The morphology is thermally reversible, as shown by the identical scattering patterns before and after heating.

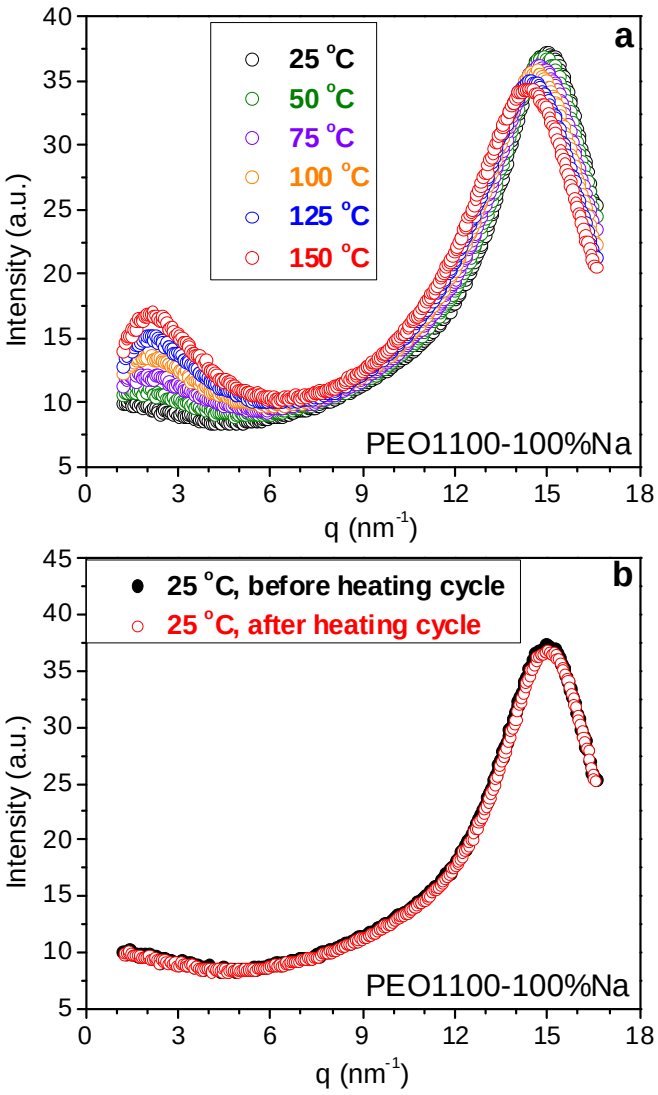

Figure C.6 a) X-ray scattering data of PEO1100-100%Na as a function of temperature. An ionomer peak gradually appears as the temperature increases, suggesting reorganization of ionic groups into ionic aggregates. b) The morphology is thermally reversible, as shown by the identical scattering patterns before and after heating. While PEO1100-100%Na can be semicrystalline at room temperature, depending on the thermal history, this sample is amorphous.

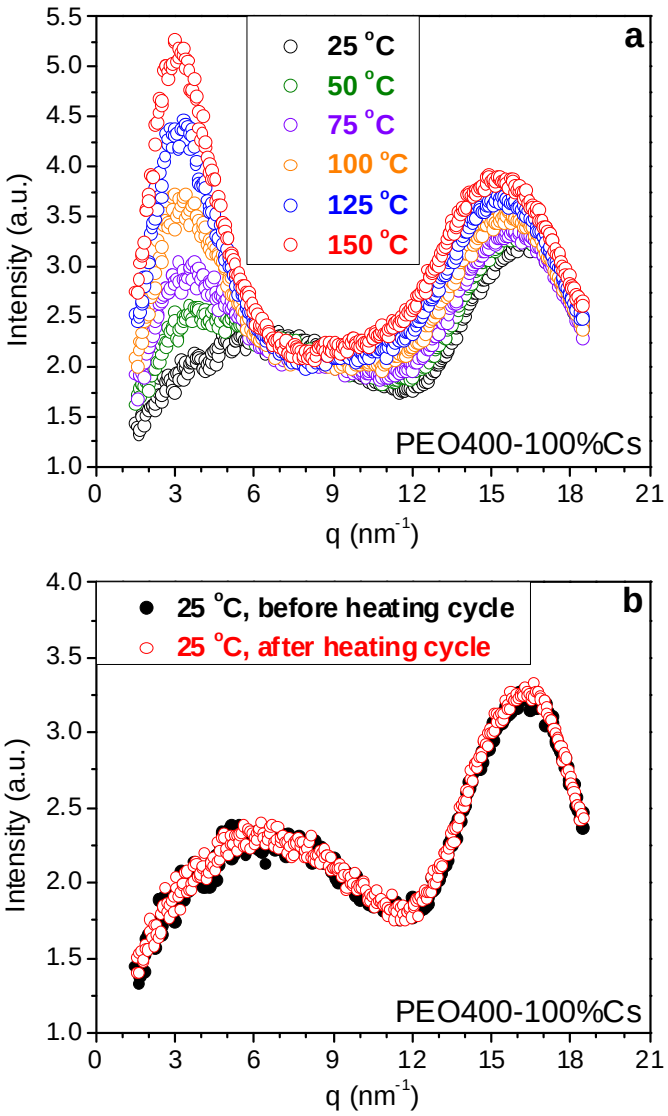

Figure C.7 a) X-ray scattering data of PEO400-100%Cs as a function of temperature. An ionomer peak gradually appears as the temperature increases, suggesting reorganization of ionic groups into ionic aggregates. b) The morphology is thermally reversible, as shown by the identical scattering patterns before and after heating.

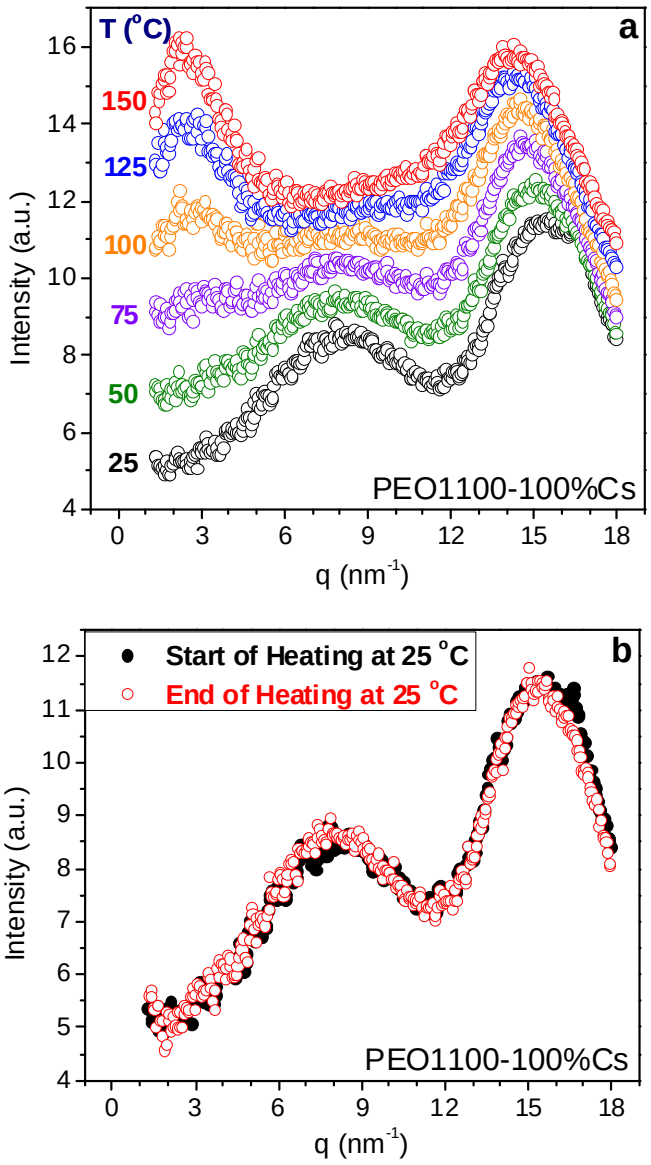

Figure C.8 a) X-ray scattering data of PEO1100-100%Cs as a function of temperature. The scattering data at higher temperatures are vertically shifted for clarity. An ionomer peak gradually appears as the temperature increases, suggesting reorganization of ionic groups into ionic aggregates. b) The morphology is thermally reversible, as shown by the identical scattering patterns before and after heating. PEO1100-100%Cs can be semicrystalline at room temperature, depending on the thermal history; this sample shows slight crystallinity before heating.

Appendix D:

X-ray Scattering of Well-Defined 12, 12-Ammonium Ionenes

A series of water-soluble 12,12-ammonium ionenes were prepared from 1,12-dibromododecane and 1,12-bis(N,N-dimethylamino)dodecane via the Menschutkin reaction, Scheme D.1.[1] A stoichiometric imbalance of monomers controlled the final molecular weights of the polymers. The macromolecular structures were confirmed with ^{1}H NMR spectroscopy, and the absolute weight-average molecular weights were determined using multi-angle laser light scattering (MALLS) with aqueous size exclusion chromatography (SEC). As shown in Table D.1, the obtained experimental M_w values were consistent with the calculated molecular weight values.

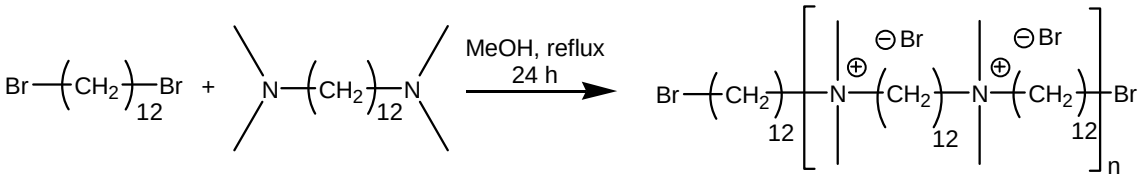

Scheme D.1 Synthesis of bromine-terminated 12,12-ammonium ionenes.

Table D.1 Ionene ditertiary amine monomer: dihalide monomer molar ratios and corresponding molecular weights.

Monomer Molar Ratio	Calculated Molecular Weight (g/mol)[a]	M_w (g/mol)[b]
1.00:1.00	-	20900
1.00:1.03	19800	17800
1.00:1.05	12000	14600
1.00:1.07	8600	12300
1.00:1.10	3200	4300

[a] Calculated molecular weights for offset stoichiometry determined from Carother's equation. [b] Molecular weights are absolute and determined from the MALLS detector.

X-ray scattering was performed on stretched and unstretched 20,900 g/mol 12,12-ionene films. The stretched sample was elongated ~ 200% with heating at 70 °C. Both stretched and unstretched films were isotropic as evident in the two-dimensional scattering patterns (Figure D.1). Both films were also amorphous with a broad amorphous peak at ~ 14 nm^{-1}, and crystalline peaks corresponding to polyethylene were not observed. This result was consistent with DSC and DMA data.[1] In addition, there was a scattering peak at 4.38 nm^{-1}, which corresponded to a real-space distance of 1.43 nm. While the ammonium groups prevented crystallization, these ionic groups assembled into ionic domains. The correlation distance between these domains was well-defined because the separation between ionic groups was exactly 12 methylene groups. If this polyethylene segment was in the all-*trans* crystalline conformation, the ammonium-ammonium separation would be 1.60 nm. The somewhat smaller separation observed here was consistent with the amorphous morphology.

Wagener and co-workers have also synthesized a periodic ionomer, and their reported morphology was similar to this work.[2] The poly(ethylene-*co*-acrylic acid) (EAA) copolymer had 9, 15 or 21 methylene groups between pendant carboxylic acid groups. As in the 12,12-ionene, the correlation lengths between acid groups was comparable or somewhat smaller than the all-*trans* polyethylene conformation. However, in sharp contrast to the 12,12-ionene, the EAA copolymer with the longest polyethylene spacer (21 methylene units) exhibited crystallinity and multiple reflections indicated that packing was more regular. In a similar fashion to the 12,12-ionene, the EAA copolymer with the 15 methylene units between acid groups remained anisotropic upon stretching. In both the EAA copolymers and 12,12-ionenes, the primary structure of the polymers

dictated the nanoscale morphology. The comparison of ammonium ionenes to EAA copolymers may also suggest the relatively more efficient aggregation of metal carboxylates versus large, organic ammonium cations as reported earlier.[3, 4]

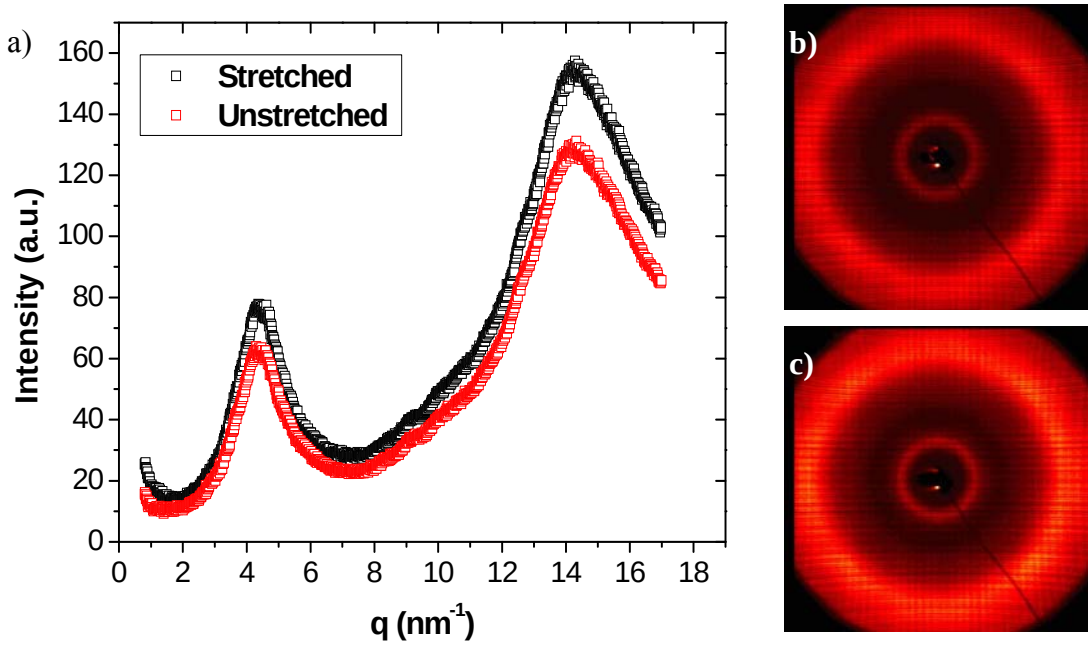

Figure D.1 X-ray scattering profiles of the 1:1 12,12-ionene. a) Scattering intensity vs. scattering vector *q* for stretched and unstretched 12,12-ammonium ionenes films; b) Wide-angle X-ray scattering pattern of stretched ionene film; c) Wide-angle X-ray scattering pattern of unstretched ionene film.

References

1. Williams, S. R.; Borgerding, E. M.; Layman, J. M.; Wang, W.; Winey, K. I.; Long, T. E. *Macromolecules* **2008,** 41, (14), 5216-5222.

2. Baughman, T. W.; Chan, C. D.; Winey, K. I.; Wagener, K. B. *Macromolecules* **2007,** 40, 6564-6571.

3. Capek, I. *Advances in Colloid and Interface Science* **2004,** 112, (1-3), 1-29.

4. Capek, I. *Advances in Colloid and Interface Science* **2005,** 118, 73-112.